# Sub-wavelength Metal-Clad Semiconductor Lasers

by

**Min W. Kim**

A dissertation submitted in partial fulfillment
of the requirements for the degree of
Doctor of Philosophy
(Electrical Engineering)
in the University of Michigan
2011

**Doctoral Committee**:

Assistant Professor Pei-Cheng Ku, Chair
Professor Pallab K Bhattacharya
Associate Professor L Jay Guo
Assistant Professor Vanessa Sih

# Table of Contents

# List of Figures

# CHAPTER 1

# Introduction

## 1.1 History of Semiconductor Lasers

LASER is an acronym for Light Amplification by the Stimulated Emission of Radiation, first theorized by Albert Eistein in 1917 and then-termed "stimulated emission". The first person to experimentally demonstrate it was Charles Townes, who showed stimulated emission at microwave frequencies. Later on, Theodore Maiman showed it in a ruby crystal at optical frequencies in 1960. Semiconductor laser was invented in 1962. [1] Since its first experimental demonstration in 1960, the semiconductor laser technology has improved significantly and been widely commercialized in areas of consumer electronics such as CDs and DVDs [2-4], medicine such as sensing and LASIK [5-7], information technology (IT) [8, 9] and more. In fact, the most significant contribution of semiconductor laser technology could be the fiber-optic communication. The use of a laser is the backbone of internet technology in which a coherent beam of 1550 nm is unanimously used for communication [9].

Fiber-optic communication allows transmitting of information over a long distance by sending pulses of laser light through an optical fiber. Because of its superior functionality including lower attenuation and interference, it has replaced communication via electrical transmission and reshaped the telecommunications industry since its first development in the 1970s. With advancements in the semiconductor laser technology, fiber-optic communication has also undergone several generations. Each generation improves the data bit rate as well as loss. Since the third generation of the technology developed in 2001, InGaAsP laser with 1550 nm is being used.

## 1.2 Reason for Miniaturization of Semiconductor Lasers

As if to further pervasiveness of the use of lasers in everyday life, there has been a growing interest in integrating electronic and photonic components in recent years [10-12]. One such area is in replacing metallic interconnects with optical interconnect whose interest was spurred by increasing problem of heat dissipation in purely electronic components [13-14] among other things. For instance, modern CMOS transistors have eight or more layers of metallic interconnects, all of whom create heat as current travels through them. Moreover, by replacing metallic interconnects with optical ones, one can minimize unnecessary capacitance, thereby improving transistor speed performance [15]. Moreover, optics can alleviate or even solve most of the physical problems that limit electrical interconnections, such as signal and clock distortion, skew and attenuation, impedance matching, cross-talk, power dissipation, wave reflection phenomena, interconnect density limitations, and voltage isolation [14]. Optics opens new doors that

did not exist with electrical interconnections, such as free-space parallel interconnections, wavelength-division multiplexing, and the use of short optical pulses for timing and improved interconnect performance [14].

However, in order for optical interconnect to be plausible, we need a light source that is of the same order of magnitude in size, such that it can be epitaxially grown and fabricated on the same wafer as electronic VLSI. Since the beginning, transistors have been shrinking faithfully, following Moore's law, with the current state-of-the-art CMOS node size of 32nm [16]. However, laser technology has not been following the same trend and still stands near a free-space wavelength in physical dimension. A dense optical interconnect network requires nanoscale components to be compatible with electronic components. Firstly, ultra-small laser will enable low power consumption. Furthermore, thresholdless lasing can be made possible owing to the high efficiency coupling of spontaneous emission into one lasing mode [17].

## 1.3 Previous Work on Nanolaser

To summarize the laser theory, laser is obtained when incoming energy, greater than the band gap of material, is absorbed by a gain medium and undergoes population inversion inside a cavity resonator. Incoming energy is absorbed by a gain medium, and, consequently, electrons are raised into excited states, which recombine with holes and release photons of the same energy. When the number of particles in an excited state is higher than that in a lower energy state, population inversion is obtained, a state wherein stimulated emission is greater than absorption. As this process is obtained in a cavity

resonator composed of reflective surfaces, emitted photons pass through the gain medium multiple times before leaving the resonator due to an aperture or losses. Lasing occurs when the total gain is greater than the total round trip loss including diffraction loss and material loss. In order for this to happen, good confinement of photons inside the cavity resonator is a necessity. Conventionally, index contrast using two different materials or air cladding has been used to create photonic confinement [18-20]. However, using this scheme it is difficult to confine photons in a space smaller than a wavelength.

Much attention has, therefore, been given to maximizing photon confinement in the smallest possible space. This led to the development of novel geometries, including microdisk cavities [21- 24] , photonic crystals [25], and nanowires [26,27,28] , distributed Bragg reflector [29], and micro-toroid resonator [30]. However, as more recently demonstrated, one of the most promising schemes to address the problem of photon confinement to nanoscale dimensions seems to be the use of metal. Light penetrates little into the metal layer and can, therefore, be confined in a much tighter space. State-of-the-art sub-wavelength lasers that employ such method include: bowtie cavity lasers [31,32] , metal-clad nanopillar and Fabry-Perot lasers [33,34], plasmonic nanowire lasers [35], nanopatch laser [36], and spacer-based nanolasers [37]. The following describes some of the state-of-the-art nanolasers.

In all of the cases below, authors rely on metal's ability to tightly confine light because electric field must rapidly go to zero inside it. One difference is that, with the presence of metal, optical modes can take on various shapes: pure surface plasmon, standing-wave hybrid dielectric-plasmonic, and traveling hybrid dielectric-plasmonic. From the below state-of-the-art examples, state-of-the-art hybrid dielectric-plasmonic

lasers include the metal-clad nanopillar and Fabry-Perot lasers, plasmonic nanowire laser, and nanopatch laser. An example of pure surface plasmon nanolasers includes the spacer-based nanolaser. In all of the three cases, use of metal increases absorption loss significantly, with pure surface plasmon cavities suffering the greatest metal loss owing to the large overlap between the lasing mode and the metal. By shifting the peak of the electric field away from metal, the hybrid dielectric-plasmonic modes are able to lessen the burden of metal loss. However, the hybrid mode requires a larger laser cavity. Hence the trade-off needs to be understood in order to optimize the semiconductor laser structures while scaling.

**Metal-clad lasers**

Hill, *et al* in Ref. [33] and [34] demonstrate nanopillar and Fabry-Perot lasers encapsulated in Au film. Using the metal-insulator-semiconductor-insulator-metal system, electric field is confined within ~500nm laterally. In the vertical direction, electric field is confined using index contrast to ~1μm. Most of their experiments were done in cryogenic temperatures or at room temperature with pulsed operation. The authors discuss the impact that the geometry can have on the quality factor and threshold current. Additionally, reducing the insulator layer thickness reduces gain requirement for lasing.

**Plasmonic nanowire laser**

Oulton, *et al* in Ref. [35] takes advantage of surface plasmon, which is capable of tightly localizing light. However, surface plasmon suffers from high ohmic loss at optical frequencies. To address this problem, the authors utilize a hybrid plasmonic waveguide, which is a metal-insulator-semiconductor structure wherein a CdS nanowire sits on top of Ag, separated by a 5nm-thick insulator. The nanowire is ~100nm in diameter, and the optical mode is confined to FHWM of ~40nm. All experiments are conducted in liquid helium-cooled temperatures, T < 10K, using a frequency-doubled Ti-Sapphire mode-locked laser.

**Nanopatch laser**

Yu, et al shows in Ref. [36] lasing in a nanopatch laser which is a cylindrical gain semiconductor gain medium sandwiched between a circular metal nanopatch and a ground metal plane. They, too, rely on metal-dielectric light confinement. Lasing is demonstrated with optical pumping using cryogenic temperature and pulsed pumping.

**Spacer-based nanolaser**

Noginov, et al in Ref. [37] demonstrates lasing in hybrid Au/silica/dye nanoparticles of diameter ~40nm. The nanoparticles were optically pumped with a pulsed laser at room temperature. This structure employs surface plasmon oscillations with a gain medium in close vicinity.

## 1.4 Organization of the Thesis

The objective of this thesis is to investigate a nanolaser whose fabrication site can be precisely controlled and whose in-coupling and out-coupling allow dense integration with electronic components such that it can become an essential building block for integrated circuits. The organization of this thesis is as follows.

In Chapter 2, theory of surface plasmon will be discussed, in which metal loss in a surface plasmon mode will be introduced. In Chapter 3, compensation of metal loss in a surface plasmon mode by placement of a gain medium will be investigated. Hybrid dielectric/plasmonic mode will also be introduced. In Chapter 4, theory and experimental results of a nanolaser employing surface plasmon and named surface plasmon-enabled semiconductor injection laser (SPESIL) will be presented. In Chapter 5, a laser, employing hybrid dielectric and plasmonic modes and named semiconductor nanoring laser, will be presented and explored. In Chapter 6, lasing in a sub-wavelength scale nanoring ring laser will be presented. Additionally, fine-tuning capability of a nanoring ring laser will be explored. In Chapter 7, summary of research will be given as well possible future work.

# CHAPTER 2

# Surface Plasmon Loss

It is generally well-established that the theoretical limit to semiconductor laser miniaturization is imposed due to diffraction limit, which is about half of a wavelength. Using conventional schemes, it is not possible to obtain a laser smaller than the limit. However, it has been proposed that, using surface plasmon or hybrid optical-plasmonic mode, the limit can be overcome. However, surface plasmon suffers from the greatest loss due to the placement of its electric field's peak at the metal-dielectric interface. The following section will describe what surface plasmon is and why it is so subject to metal loss. Additionally, a brief survey on previous works on the compensation of the metal loss is presented. Lastly, advantages and disadvantages of hybrid optical-plasmonic mode over surface plasmon will be studied.

## 2.1 Surface Plasmon

Surface plasmon is electromagnetic waves that propagate along the metal/dielectric interface, whose power flow is along the interface, as derived in Eqn. 2.1.1 through 2.1.3.

$$\vec{H} = \hat{y}H_y \quad \text{(Eqn. 2.1.1)}$$

$$\vec{E} = \hat{x}E_x + \hat{z}E_z \quad \text{(Eqn. 2.1.2)}$$

$$P = \frac{1}{2}\int \vec{E} \times \vec{H}^* \, dx = \hat{z}P_z \quad \text{(Eqn. 2.1.3)}$$

Their electromagnetic fields decay exponentially into the space perpendicular to the metal/dielectric interface, with their maximum located at the interface, as is characteristic for surface waves, as shown in Fig. 2.1.1. The field is described by:

$$E = E_0^{\pm}\exp\left[+i(k_x x \pm k_z z - \omega t)\right] \quad \text{(Eqn. 2.1.4)}$$

with + for z ≥ 0 and − for z ≤ 0 and with an imaginary $k_x$, which yields an exponentially decaying $E_x$. [38]

The spatial extension of SP waves can be determined using the following equations [38]:

$$\text{In the dielectric with } \varepsilon_2 : \hat{x}_2 = \frac{\lambda}{2\pi}\left(\frac{\varepsilon\prime_1+\varepsilon_2}{\varepsilon_2^2}\right)^{1/2} \quad \text{(Eqn. 2.1.5)}$$

$$\text{In the metal with } \varepsilon_1 : \hat{x}_1 = \frac{\lambda}{2\pi}\left(\frac{\varepsilon\prime_1+\varepsilon_2}{\varepsilon\prime_1^2}\right)^{1/2} \quad \text{(Eqn. 2.1.6)}.$$

9

Using the above equations, it can be found that SP extends ~50nm into a semiconductor and ~20nm into the metal. Such nanoscale confinement has attracted many groups to employ SP in the fields of photonic and optoelectronic devices [39-43], metamaterials [44] and biosensing[45, 46] for miniaturization, superior resolution, and speed.

While SP has the advantage of tight photonic confinement as mentioned, the presence of metal at the maximum of electromagnetic field presents a problem of absorption, yielding a very short propagation distance. The length L after which the intensity of SP decreases to $1/e$ is given by:

$$L = (2k''_z)^{-1} \quad \text{(Eqn. 2.1.7)}$$

Thus, free space SP propagation distance is only a few micrometers. However, it has been shown in non-semiconductor systems that such large metal can be at least partially compensated by putting a gain medium in very close proximity to the metal/dielectric interface.
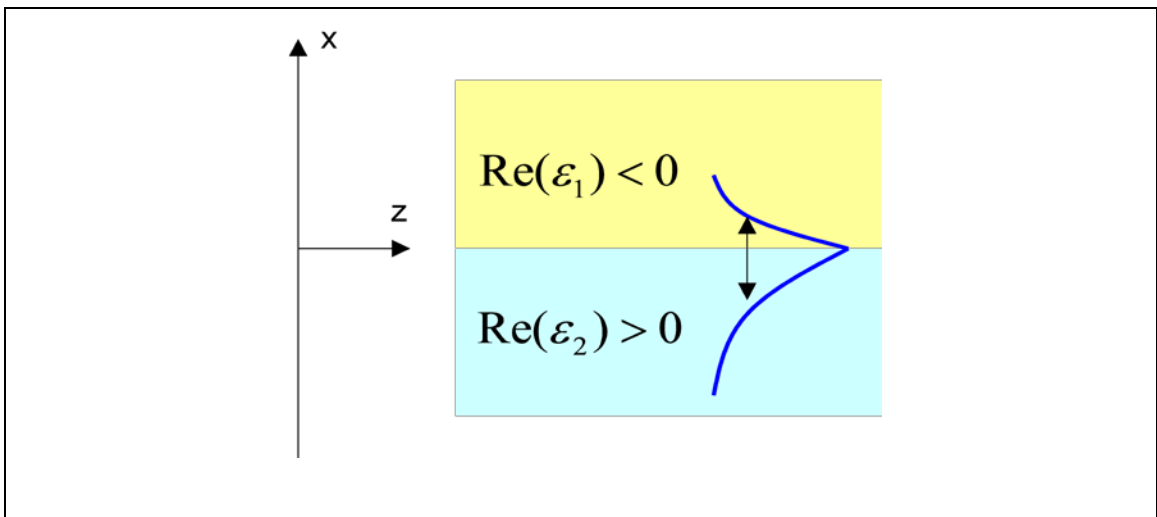


Fig. 2.1.1 Field profile of a surface plasmon wave propagating at a metal/dielectric interface

## 2.2 Previous Work on Loss Compensation by a Non-semiconductor Gain Medium

As described above, because SP waves propagate along a metal surface, absorption loss is detrimental to device operation, with a propagation length of only a few micrometers.  In order to overcome this disadvantage, various groups have shown that a gain medium placed in close proximity can compensate for the metal loss.  It was first proposed theoretically that optical gain in a dielectric medium can elongate the SP propagation length [47].  The first noteworthy experiment took place using a pump-probe configuration on an interface between a silver (Ag) film and optically pumped polymer dye, in which SP loss suppression was reported [48].  The authors of Ref. [48] have reported that their achieved value of gain, 420 cm$^{-1}$, is sufficient to fully compensate the intrinsic SP loss in high-quality silver films.  A similar result has also been reported in an experiment using a gold (Au) strip embedded in Er-doped phosphate glass [50], whose result is shown in Fig. 2.2.1 .  Transmitted SP intensity was measured with varying optical pumping power, and it was shown that the measured signal at the end of the waveguide was enhanced with higher pump power.

Fig. 2.2.1. Experiment showing propagation length increase in optically pumped Er-dope phosphate glass with a gold strip [50]
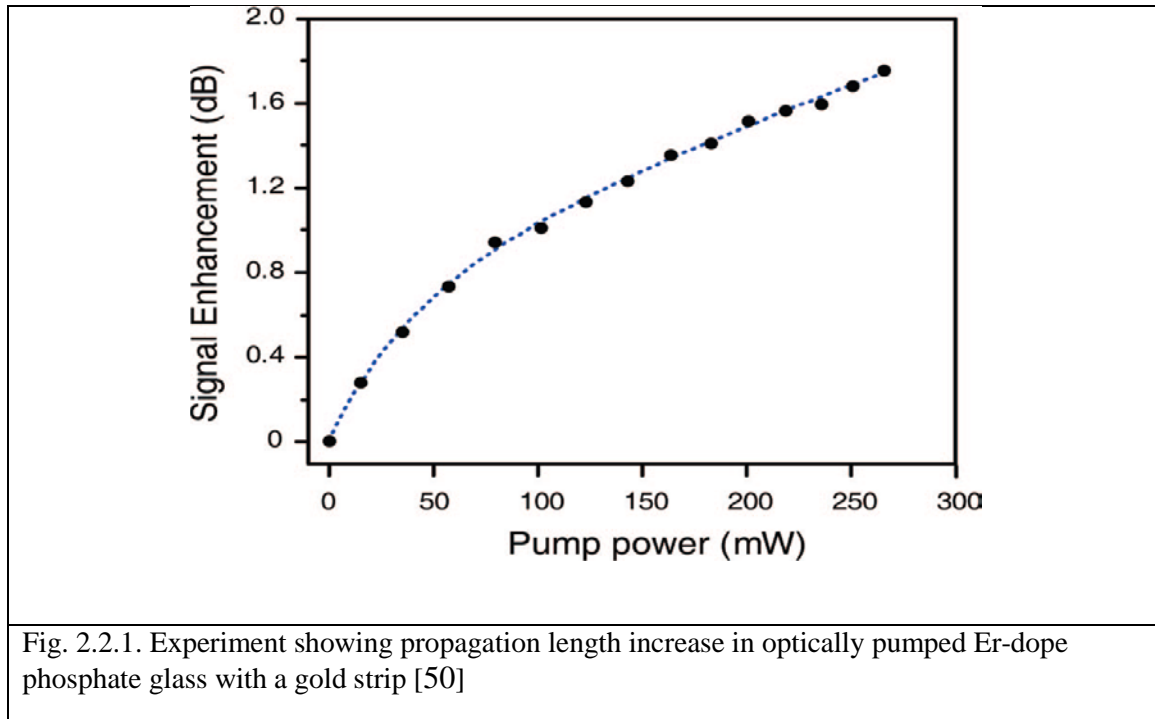
## 2.3 Surface Plasmon versus Hybrid Dielectric-Plasmonic Mode

Surface plasmon has a skin depth of about 50 nm, which allows electric field to be confined in smallest possible dimensions. Therefore, for smallest nanolasers, it is most desirable to use surface plasmon. However, employing surface plasmon requires a special geometry of a resonant cavity wherein the maximum of the field is located at the metal-dielectric interface, which introduces large metal loss. Using hybrid dielectric-plasmonic mode allows one to utilize common resonant cavity geometries and take advantage of superior confinement offered by metal. Hybrid dielectric-plasmonic mode utilizes dielectric materials sandwiched between metal for tighter field confinement with assistance of metal, as shown in Fig. 2.3.1. The figure is an FDTD simulation of

semiconductor sandwiched between two silver films. The semiconductor was 300nm with refractive index of 3.5. The silver films were 200nm thick.



Fig. 2.3.1. FDTD simulation of a hybrid dielectric-plasmonic mode. The structure has 300 nm of semiconductor with *n*=3.5 sandwiched between 2 silver films of 200 nm.
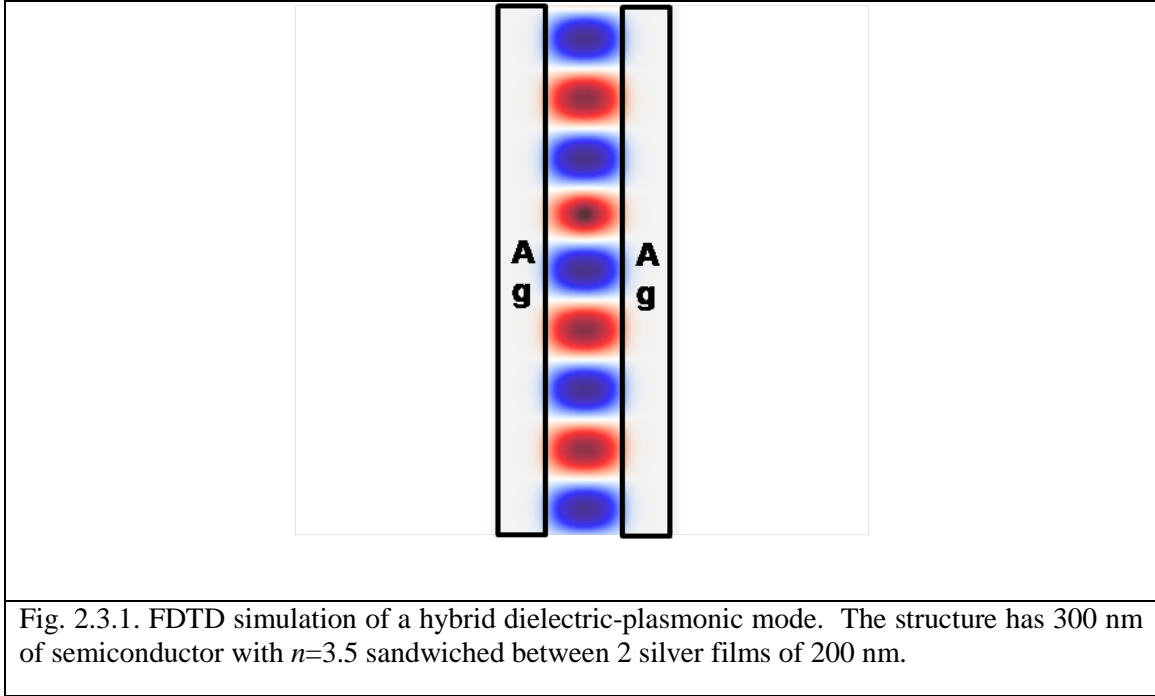
As can be seen from the figure, electric field must rapidly decrease to zero inside a perfect conductor such as metal. However, inside the semiconductor, field is confined similar to other index-contrast confinement. Because one can avoid placing the maximum of the field in close vicinity to metal, metal loss can also be reduced. However, in both cases, it is critical to simultaneously optimize the geometry of the metallic optical cavity and gain region such that the electric field overlap with the active region is maximized in order to maximize the modal gain.

## 2.4 Summary

In this chapter, theory of surface plasmon was discussed. Because surface plasmon decays exponentially both into the dielectric and the metal, it can provide the smallest possible laser dimensions. However, one must deal with the loss that comes with the fact that the peak of the electric field is at the interface between metal and dielectric. One possible solution is to place a gain medium in close proximity. However, no work has previously done to ensure it works for semiconductor materials as well.

Another way to employ metal to take advantage of metal, but to avoid high metal loss is to use a hybrid optical-plasmonic mode. Such mode shifts the peak of the electric field away from the metal to the center of dielectric, so that metal loss is reduced.

# CHAPTER 3

# Surface Plasmon Loss Compensation by a Semiconductor Gain Medium

In order to obtain the smallest possible nanolaser, use of surface plasmon has been explored. As described in the previous chapter, surface plasmon suffers from extrememly high metal loss. However, placement of a gain medium in close proximity has been suggested as a loss compensation scheme. While others were investigating non-semiconductor materials such as organic polymer dye as a gain medium, we investigated plausibility of a semiconductor medium to compensate metal loss. Semiconductor gain media have the advantage of providing a larger material gain and can be more easily integrated with other optoelectronic components. Therefore, it is highly desirable to use a semiconductor gain medium such as multi-quantum wells (MQWs) instead of polymer dye or organic materials as previous works on the topic have done. In order to demonstrate that loss compensation can occur in a semiconductor system, the following experiment was carried out.

## 3.1 Quantum Wells (QWs) as a Gain Medium

In order for easier integration with electronic components, it is highly desired that the material system be composed of semiconductor materials. Furthermore, having a system that can yield a high density of states, and therefore a high material gain, is advantageous. In this section, theory behind quantum wells will be described that shows how the density of states can be higher in quantum wells, compared to a bulk material.

According to Ref. [49], the Schrödinger equation for the electron states in the quantum can be written as follows in a simple approximation:

$$\left[-\frac{\hbar^2}{2m^*}\nabla^2 + V(z)\right]\Psi = E\Psi \qquad \text{(Eqn. 3.1.1)}$$

where $m^*$ is the effective mass of the electron. This problem can be simplified as

$$\Psi(x, y, z) = e^{ik_x x}e^{ik_y y}f(z) \qquad \text{(Eqn. 3.1.2)}$$

where $f(z)$ satisfies

$$\left[-\frac{\hbar^2}{2m^*}\frac{\partial^2}{\partial_z^2} + V(z)\right]f(z) = E_n f(z) \qquad \text{(Eqn. 3.1.3)}$$

Assuming an infinite barrier approximation, $f(z)$ becomes:

$$f(z) = \cos\frac{\pi n z}{W} \text{ if n is even} \qquad \text{(Eqn. 3.1.4), or}$$

$$f(z) = \sin\frac{\pi n z}{W} \text{ if n is odd} \qquad \text{(Eqn. 3.1.5)}$$

where $W$ is the well size, and $E_n$ becomes:

$$E_n = \frac{\pi^2\hbar^2 n^2}{2m^* W^2} \qquad \text{(Eqn. 3.1.6)}$$

16

Each level $E_1$, $E_2$, etc., is actually a subband due to the electron energy in the x-y plane. The resulting subband structure is shown in Fig. 3.1.1 schematically.

The manifestation of this subband structure gives rise to a varied density of states, compared to a bulk system. The density of states in a quantum well is as follows:

In conduction band: $N(E) = \sum_i \frac{m^*}{\pi\hbar^2}\sigma(E - E_i)$ (Eqn. 3.1.7)

where $\sigma$ is the heavyside step function and $E_i$ are the subband energy levels.

In valence band: $N(E) = \sum_i \sum_{j=1}^{2} \frac{m_j^*}{\pi\hbar^2}\sigma(E_{ij} - E)$ (Eqn. 3.1.8)

where $i$ represent the subbands for the heavy hole ($j$=1) and light hole ($j$=2). From this, one can see that a quantum well can give a higher density of states than a bulk material whose density of states is given by:

$$N(E) = \frac{\sqrt{2}m^{*3/2}(E-Ec)^{1/2}}{\pi^2\hbar^3} \quad \text{(Eqn. 3.1.9)}$$
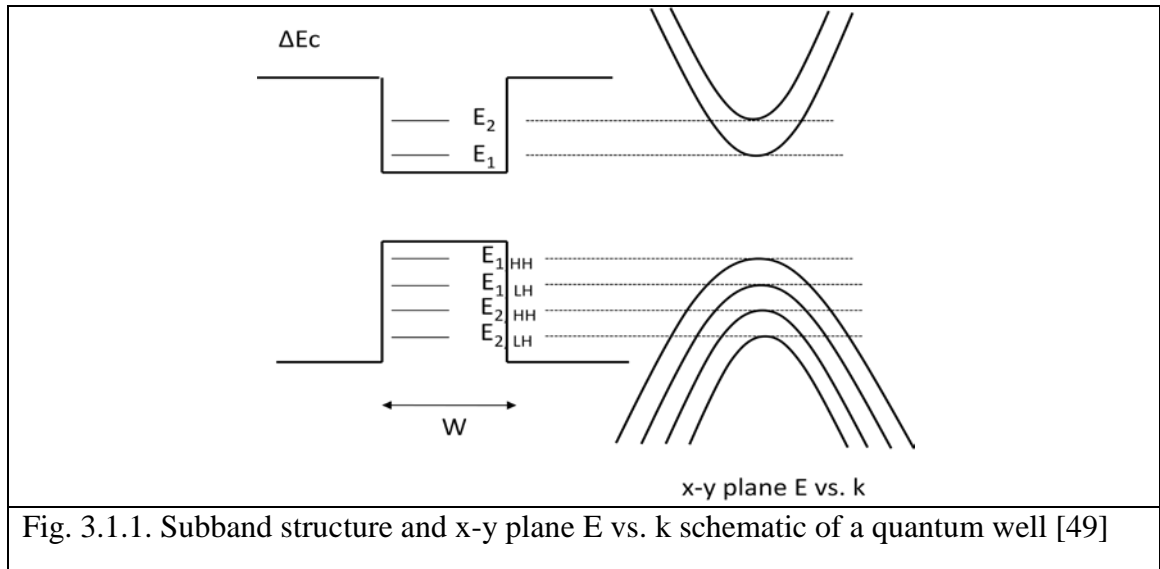


Fig. 3.1.1. Subband structure and x-y plane E vs. k schematic of a quantum well [49]

### 3.1.1 Strain to Control Band Structure

There is another parameter than can be modified in order to maximize the material gain, so as to maximize the loss compensation by a gain medium. In the previous section, it was assumed that all layers in the epitaxial growth of a heterostructure are perfectly matched. However, they have different lattice constants, and therefore, one must take into consideration the effect that the strain has in the band structure. In this section, such effect will be explored.

Fig. 3.1.2 shows how the band edges, especially the valence HH and LH bands, change with strain in a layer grown along the (001) direction. Although the conduction bandedge moves up or down with respect to its unstrained position, there is no splitting since it is a non-degenerate state. However, the valence bandedge is denegerate in the unstrained state. This degeneracy can be lifted by quantum confinement, such as in a quantum well, but splitting produced this way is usually very small, in the order of 10-15 meV. As shown in Fig. 3.1.2, under biaxial compressive strain, the bandgap of the material increases and the splitting as large as 100meV is produced with the HH state above the LH state. Under tensile strain, the bandgap decreases, and splitting happens such that the LH state is above the HH state. Splitting produced by strain can be as large as 100meV, and therefore, can be a very effective means of altering valence band density of states [49].

Fig. 3.1.2. Effect of strain on bandedges [49]
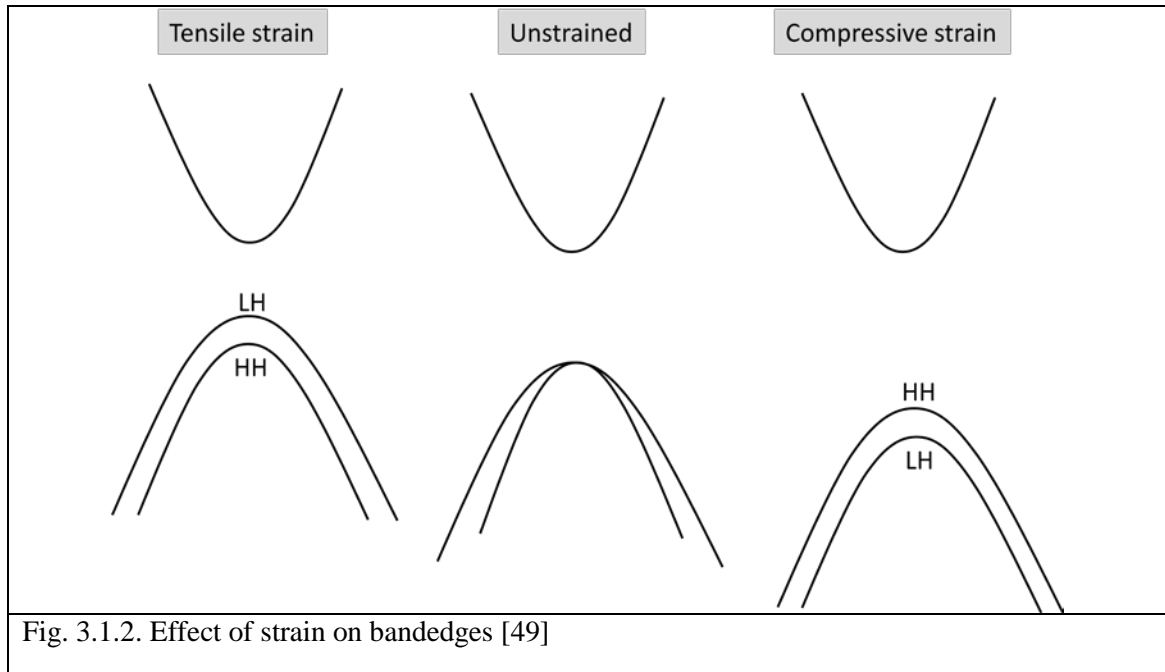
## 3.2 Layer Design for Loss Compensation Experiment

In order to accurately conduct the loss compensation by a semiconductor multi-quantum well (MQW) experiment, Sentaurus device physics simulation was carried out to simulate the band diagram of a MQW epi-wafer with Ag. The epi-wafer, as used in the simulation, is as follows. It had an n-type GaAs substrate and, as an active region, had four MQWs composed of lightly doped GaAs/AlAs (n ~ 1e16 cm$^{-3}$) of 10nm/80nm thickness, respectively. The first AlAs barrier layer was reduced to 7 nm. Unstrained GaAs/AlAs MQWs were chosen for this experiment because: (1) they can provide a strong TM gain component at a slightly shorter wavelength than the ground state transition; (2) this wavelength is more accessible by commercially available lasers as will be required in the pump-probe experiment described in the following. For electrical contact purposes, the epi-wafer was capped with 100 nm of p-GaAs (p ~ 1e16 cm$^{-3}$) with periphery to be removed for Ag deposition for electrical contact and to minimize natural

oxidation of the top AlAs barrier layer. The band diagram of the epi-wafer under 0V

forward bias is as shown in Fig. 3.2.2. In it, the left side (x = -0.2) is Ag and (x=0.1) is

the substrate. It can be seen that the first AlAs barrier sufficiently separates the first

quantum well from the Ag layer, such that carrier quenching by Ag is not a problem.

| | Layer type | Thickness (Tolerance) | Doping (Tolerance) |
|---|---|---|---|
| 11 | P-GaAs | 100nm (+/- 5%) | 1E16 cm-3 ~ 3E16 cm-3 |
| 10 | N-AlAs | 7nm (+/- 1%) | 1E16 cm-3 ~ 3E16 cm-3 |
| 9 | N-GaAs | 10nm (+/- 1%) | 1E16 cm-3 ~ 3E16 cm-3 |
| 8 | N-AlAs | 8nm (+/- 1%) | 1E16 cm-3 ~ 3E16 cm-3 |
| 7 | N-GaAs | 10nm (+/- 1%) | 1E16 cm-3 ~ 3E16 cm-3 |
| 6 | N-AlAs | 8nm (+/- 1%) | 1E16 cm-3 ~ 3E16 cm-3 |
| 5 | N-GaAs | 10nm (+/- 1%) | 1E16 cm-3 ~ 3E16 cm-3 |
| 4 | N-AlAs | 8nm (+/- 1%) | 1E16 cm-3 ~ 3E16 cm-3 |
| 3 | N-GaAs | 10nm (+/- 1%) | 1E16 cm-3 ~ 3E16 cm-3 |
| 2 | N-AlAs | 8nm (+/- 1%) | 1E16 cm-3 ~ 3E16 cm-3 |
| 1 | N-GaAs Buffer | 2um (+/- 10%) | 1E15 cm-3 ~ 1E16 cm-3 |
| 0 | N-GaAs substrate | | |

Fig. 3.2.1. Layer design



(a)

Fig. 3.2.2. Band diagram of the GaAs/AlAs epiwafer with Ag in vertical direction (left: Ag, right: substrate) under 0V forward bias (optical pumping)
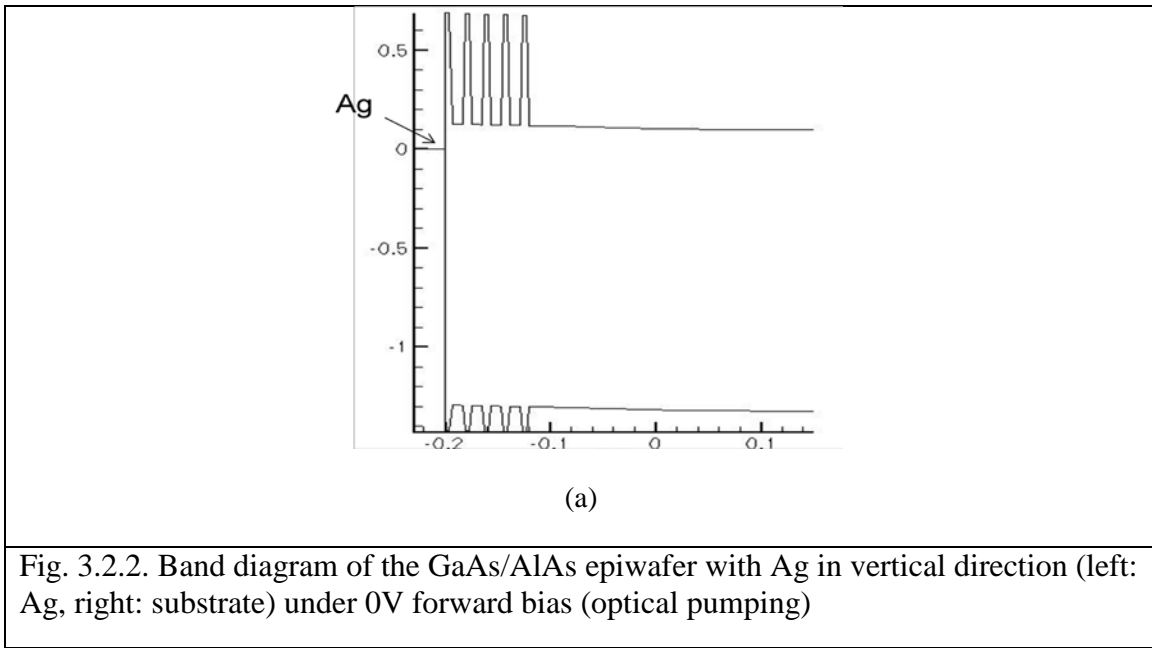
## 3.3 Loss Compensation by a MQW Gain Medium

**Fabrication**

To provide the optical gain, the sample consists of four pairs of unstrained GaAs/AlAs multiple quantum wells (MQWs) epitaxially grown by metal-organic chemical vapor deposition (MOCVD). The quantum well (GaAs) and barrier (AlAs) thicknesses are 10 nm and 8 nm, respectively. The peak wavelength of these MQWs is 840 nm at room temperature as determined by a photoluminescence measurement. Unstrained GaAs/AlAs MQWs were chosen for this experiment because: (1) they can provide a strong TM gain component at a slightly shorter wavelength than the ground state transition; (2) this wavelength is more accessible by commercially available lasers as will be required in the pump-probe experiment described in the following. The top AlAs barrier thickness is reduced to 7 nm to increase the overlap between the SP mode and the gain region. To prevent the top AlAs barrier from oxidation, a thin GaAs cap layer was first grown and then removed immediately before the deposition of a 30 nm thick Ag layer by electron beam evaporator. 1 - 2 nm of germanium wetting layer was inserted between Ag and AlAs to improve the smoothness of the Ag layer. Finally, a 100-nm thick $SiO_2$ layer was deposited to prevent the oxidation of the Ag layer.

Fig. 3.3.1. Left figure: the schematic of the sample used in the gain-assisted SPP propagation experiment. Right figure: the scanning electron micrograph of the waveguide used in the experiment.
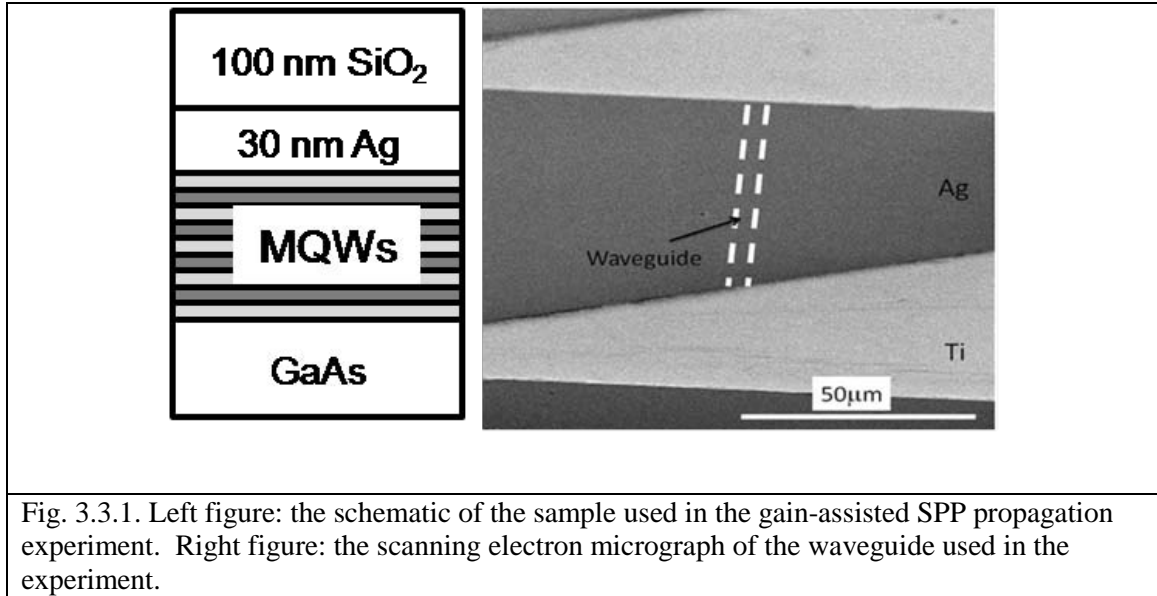
The waveguide was defined by optical lithography as shown in Fig. 3.3.1. Areas outside the waveguide region were covered with Ti to block the optical pump and thus minimize the spontaneous emission from the substrate. The sample was, then, lapped and cleaved. Because the SP propagation length is less than 2 μm at 840 nm wavelength, we are mostly interested in waveguide lengths on the order of 10 μm. Hence, only the entrance facets of the waveguides were cleaved. The exit facets of the waveguides were defined using focused ion beam (FIB). Lateral optical confinement was offered by the presence of optical pumping. That is, in the areas outside the optical excitation, the SP mode, which experiences a large metal loss, would not be able to sustain itself. Therefore each triangle shown in Fig. 3.3.1 was thought to comprise of a series of "waveguides" of different lengths from the leg to the hypotenuse.

**Measurement**

      To characterize the gain-assisted SP propagation, a pump-probe differential transmission configuration was adopted. The pump beam was generated using the second and third harmonic outputs of a mode-locked titanium-sapphire laser (Spectra-Physics Tsunami). The pump beam was first elongated by a cylindrical lens before being focused onto the waveguide using a 27X ultraviolet (UV) objective lens (Newport). The pump beam covered the entire waveguide from a normal incidence. The thickness of the Ag layer was chosen such that it was thick enough to completely confine the SP mode but thin enough for the ultraviolet pump beam to penetrate into the MQWs. The transmittance of an ultraviolet beam through a 30-nm Ag layer is around 25%, as shown in Fig. 3.3.2. The sheet carrier density in each quantum well was estimated to be around $10^{13}$ cm$^{-2}$ for 100 pJ of pump pulse energy.



Fig. 3.3.2 Transmission through 30 nm of Ag film vs. wavelength  (Yi-Hao Chen)
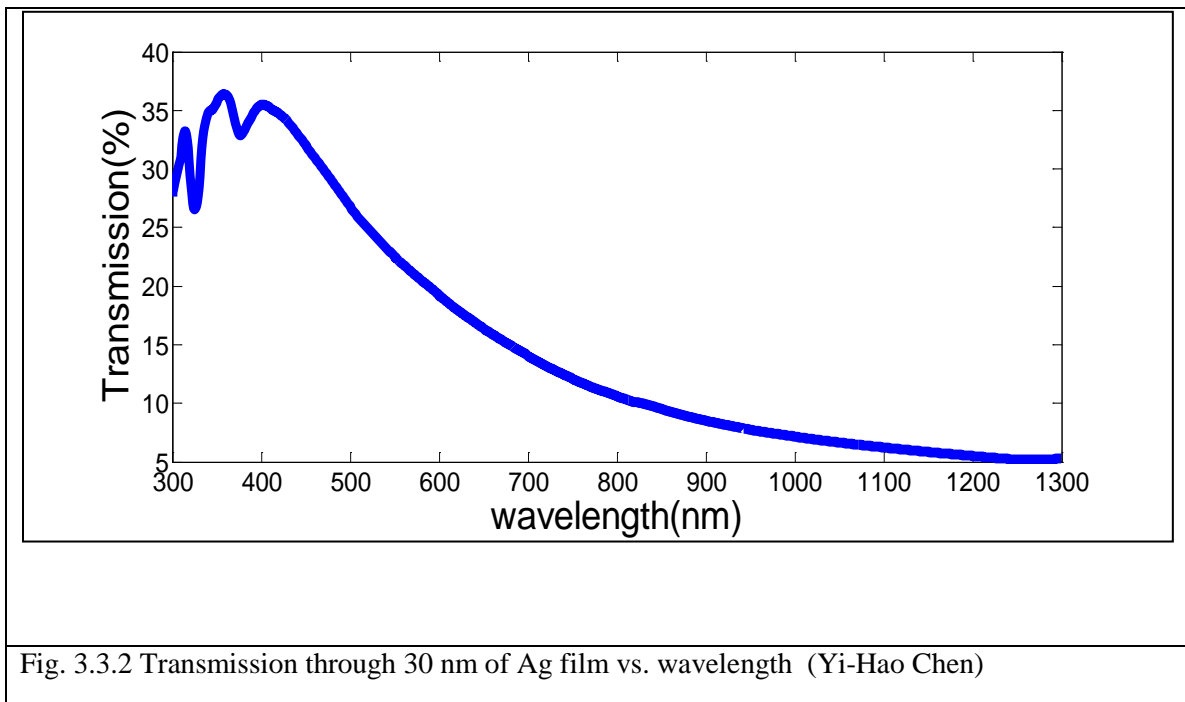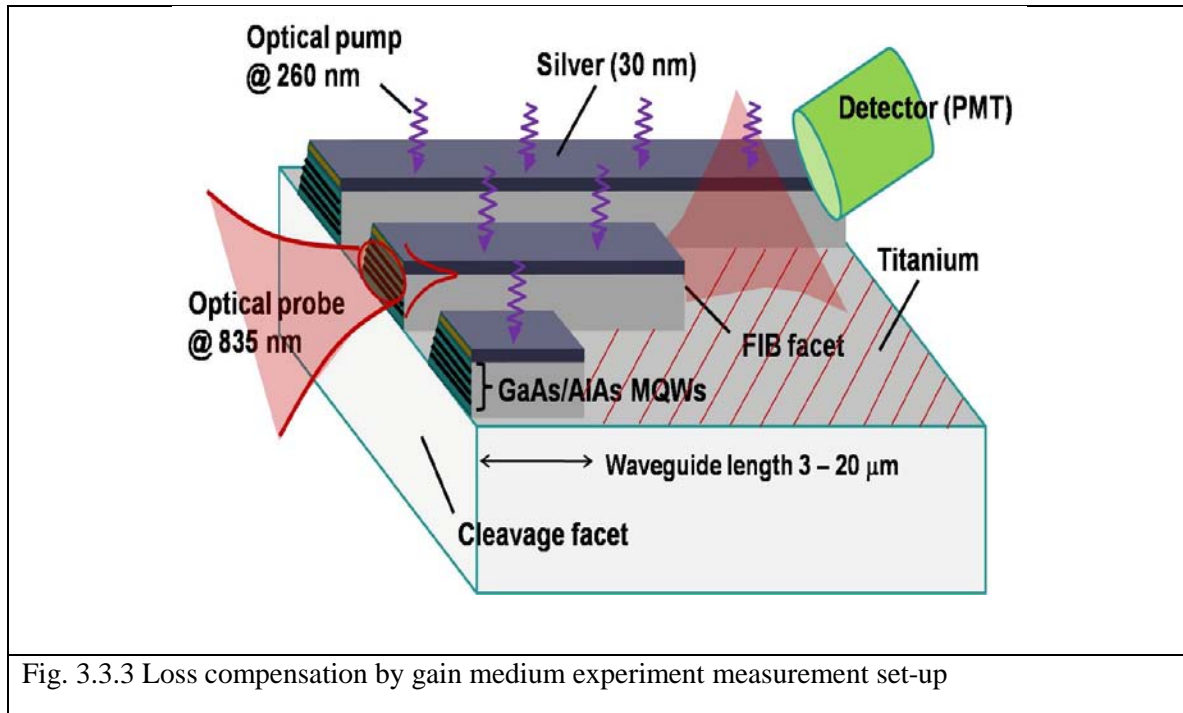
Fig. 3.3.3 Loss compensation by gain medium experiment measurement set-up

To excite the SP mode, we adopted an end-fire coupling scheme suggested in Ref [51]. Two CCD cameras are used to align the probe beam to the pump beam. Because SPs are predominantly TM polarized, we chose an 835-nm continuous-wave (CW) probe laser to excite the SP mode in order to better align the SP mode to the TM component of the optical gain. A half-wave plate and a linear polarizer were used to align the probe laser polarization perpendicular to the Ag layer. The exited SP mode was collected by a long working distance 10X objective lens (Mitutoyo) into a photomultiplier (PMT), which was then interpreted by a lock-in amplifier as follows. Assuming the pump beam went through an optical chopper, the lock-in signal then corresponded to the differential transmission ($\Delta T$) of the probe beam with and without the pump beam. Ideally, this $\Delta T$ signal relates directly to an increase of the SP intensity exiting the waveguide as a result of the gain-assisted SPP propagation. But in the experiment, the detector $\Delta T$ signal also

includes signal from MQWs spontaneous emission and scattered pump signal that enters the PMT; therefore to obtain the part of the signal that corresponded to the gain-assisted SPP propagation, we subtract the ΔT signal without the presence of the probe laser to the ΔT signal with the presence of the probe laser.  This is summarized below:

**Detector (PMT) ΔT with the presence of probe =**
gain assisted SP propagation + QW spontaneous emission + pump scattering

**Detector ΔT without probe =**
QW spontaneous emission + pump scattering

*Gain assisted SP propagation = Detector ΔT with probe – Detector ΔT without probe*

In the measurement, the pump wavelength was fixed at 260 nm and the probe power was 30 mW before entering the objective lens. Before focusing, the pump beam had 105 pJ/pulse of energy, 130 fs of pulse width, and 80 MHz of repetition rate. All measurements were performed at room temperature.  The measurement scheme is shown in Fig. 3.3.3.

Table 3.3.1. Transmission data for one waveguide same

|  | 5µm | 7µm | 9µm | 11µm |
|---|---|---|---|---|
| Transmission with Pump and Probe tother | 2.01 | 1.7 | 1.61 | 1.5 |
| Transmission with Pump only | 0.98 | 0.99 | 1.05 | 1.04 |

Fig. 3.3.4 Gain-assisted SPP propagation versus the waveguide length. Four samples were measured, which showed a common trend but different signal levels. This is due to the difference in excitation efficiency of the SP modes at the entrance facets of the waveguides. The solid line for sample 3 is fitted to Eqn. 2.2.2.1. All measurements were performed at room temperature. Inset: time-resolved photoluminescence (TRPL) measurement of GaAs/AlAs MQWs.

Table 3.3.1 shows transmission data for one of the waveguide samples. As expected, lock-in amplifier ΔT signal (in arbitrary unit) increases with decreasing waveguide length due to increased gain assisted SP propagation. However, ΔT signal when only the pump is present stays more or less constant, as expected. Fig. 3.3.4 shows how gain-assisted SP propagation varies with the waveguide length. For comparison, the SP propagation length without gain assistance was calculated to be 2 μm [38]. Therefore the ΔT signal corresponds to the SP transmission assisted by the MQW gain. In Fig. 3.3.4, all four samples show much increased SP propagation lengths. To further analyze the

26

result, we use the following relationship for the SP propagation to take into account a time-dependent optical gain due to the pulsed excitation:

$$\frac{I_{out}}{I_{in}} = \frac{C}{12ns} \int_0^{12ns} \left\{ exp \left[ -\alpha_{metal}L + \Gamma g_{TM} \left( exp \left( -\frac{t}{t_A} \right) - B \right) L \right] \right\} dt$$

(Eqn. 3.3.1)

where $I_{in}$ and $I_{out}$ are the intensity of the SP mode at the entrance and exit facets, respectively; $\alpha_{metal}$ is the metal absorption coefficient; $\Gamma$ is the optical confinement factor determined by the overlap between the SP mode and the MQWs; $g_{TM}$ is the TM component of the MQW gain; $t_A$ and B are fitted parameters determined by the time-resolved photoluminescence (TRPL) measurement, shown in Fig. 3.3.5, to account for the pulsed nature of the pump laser; we assumed the gain became negative, i.e. loss, after a certain time following the same exponential function using the term $B$; $C$ is a proportionality constant; 12 ns is the interval between two consecutive pump pulses. In Eqn. 3.3.1, $\Gamma$ was calculated to be 0.4 using a transfer matrix method [52]; $\alpha_{metal}$ was calculated to be 2100 cm$^{-1}$ using optical constants reported for an Ag thin film prepared using a similar technique [53]. From Eqn. 3.3.1, the possible range of the maximum modal gain, $\Gamma g_{TM}$ ($t = 0$), was found to range from 575 cm$^{-1}$ to 1660 cm$^{-1}$ as shown by the solid line in Fig. 3.3.4. Comparing the measured modal gain to the metal absorption loss, it is possible to at least partially compensate the metal loss via a proper optical gain.

Fig. 3.3.5. Time-resolved photoluminescence of the epiwafer used
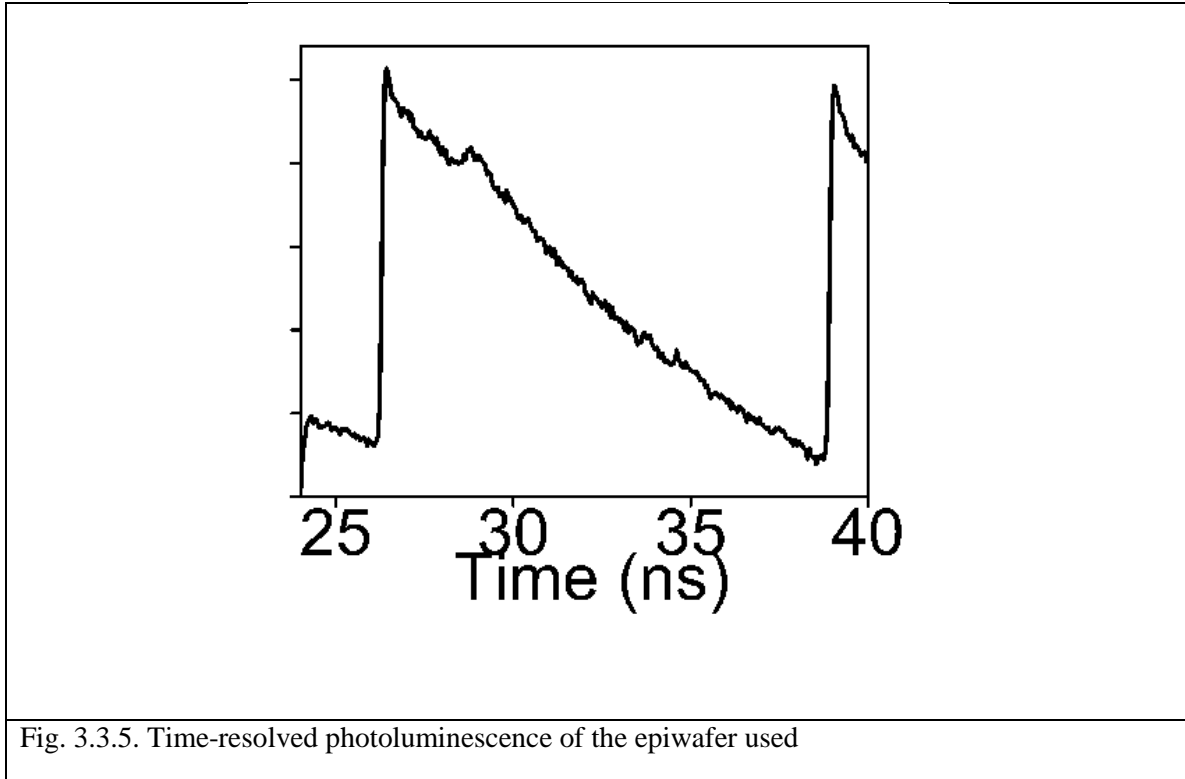
Fig. 3.3.6 shows how gain-assisted SPP propagation varies with the pump energy at a fixed waveguide length of 5 μm. In this measurement, the pump wavelength was fixed at 360 nm. The probe laser power was fixed at 33.5 mW. With increasing pump energy, the gain-assisted SPP transmission increases and follows the logarithmic gain characteristic of the MQWs according to Eqn. 2.2.2.1.

Fig. 3.3.6. Gain-assisted SPP propagation versus pump energy. The waveguide length is 5 μm. The solid line is fitted to a logarithmic equation as shown that describes the optical gain in the MQWs. In the equation: $\varepsilon_s$" is the imaginary part of the semiconductor dielectric function; $P$ is the pump power. The measurement was performed at room temperature.
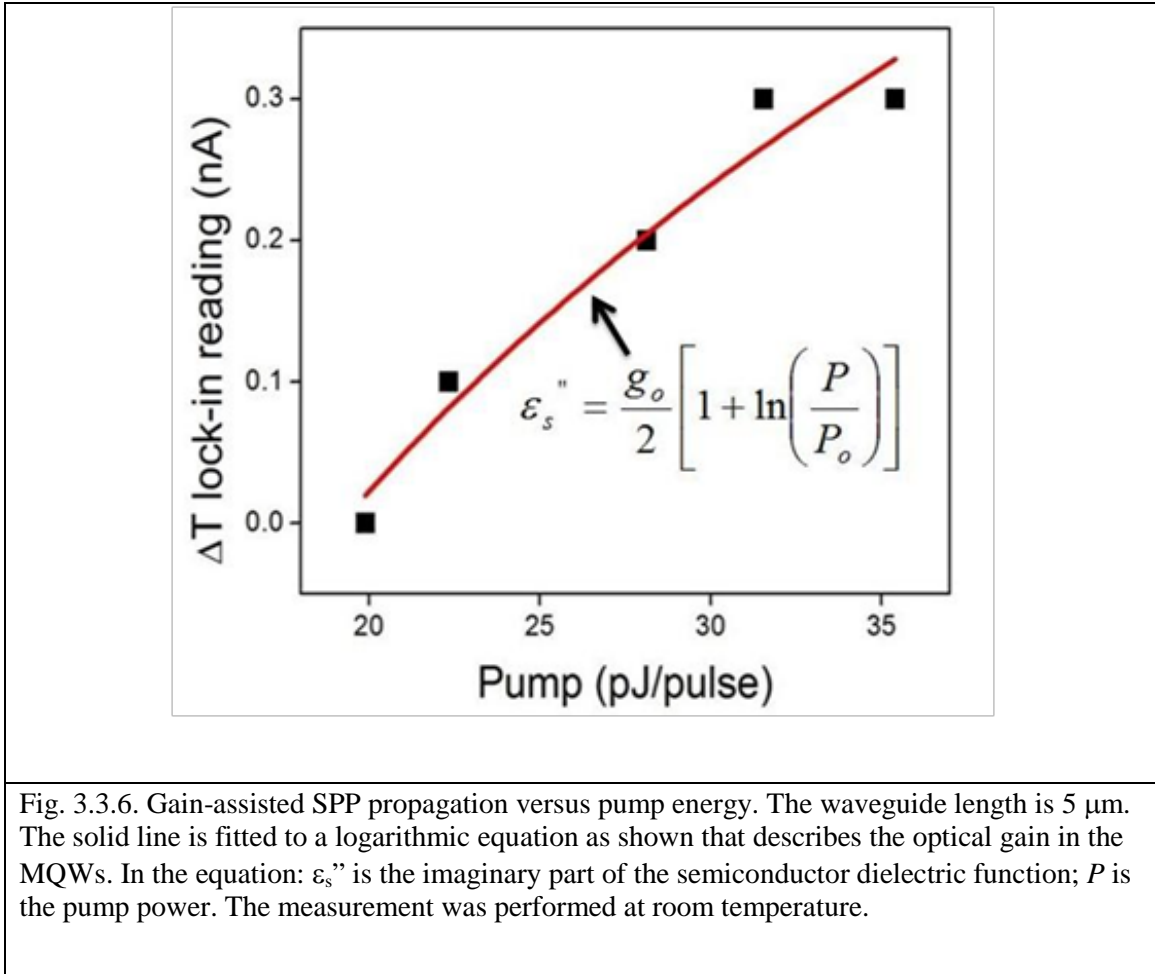
## 3.4 Summary

In this chapter, it was shown that metal loss in a surface plasmon can be at least partially compensated by placing a semiconductor gain medium such as multi-quantum wells (MQWs). Strain can be used to modify the band edges of MQWs. For example, we used unstrained quantum wells in our gain compensation experiment to emphasize the TM gain that surface plasmon mode primarily experiences. Additionally, it is important that a gain medium be placed in close proximity to the metal-semiconductor interface such that the overlap of the electric field and the gain medium is maximal.

We conducted a waveguide experiment, from which we discovered that an optical gain of range from 575 cm$^{-1}$ to 1660 cm$^{-1}$ can be obtained by placing MQWs 7 nm away from the metal-semiconductor interface. Although it was not enough to compensate the loss completely, which was calculated to be 2100 cm$^{-1}$, loss compensation by gain medium is found to be a valid method to overcome the difficulty.

# CHAPTER 4

# Surface Plasmon Enabled Sub-wavelength Injection Laser (SPESIL)

## 4.1 Laser Operation Theory

Combining the theory of exponentially decaying field profile of surface plasmon and loss compensation by a gain medium placed in close proximity to the metal/semiconductor interface, surface plasmon enabled sub-wavelength injection laser (SPESIL) structure that employs a nanoscale whispery gallery mode (WGM) cavity has been investigated, whose schematic is shown in Fig. 4.1.1. The WGM nanocavity of the SPESIL supports a transverse-magnetic (TM) polarized surface plasmon mode at the interface between the metal and the gain medium. Transverse and lateral optical confinement is provided by the SP mode and the WGM mode, respectively. Although the propagation length of the SP mode is very short due to a large metal dissipation loss, it has been shown that a gain medium placed in close proximity can compensate such a loss, as theoretically as shown in Fig. 4.1.2 and experimentally [48, 50, 54-56]. It shows that with an optical gain of 2000/cm, quality factor of the optical cavity can increase by a factor of 10, as shown in Fig. 4.1.2.

Fig. 4.1.1. The schematic of the proposed sub-wavelength SPESIL structure.



Fig. 4.1.2. 3D FDTD result of loss compensation by gain medium in SPESIL (Yi Hao Chen)
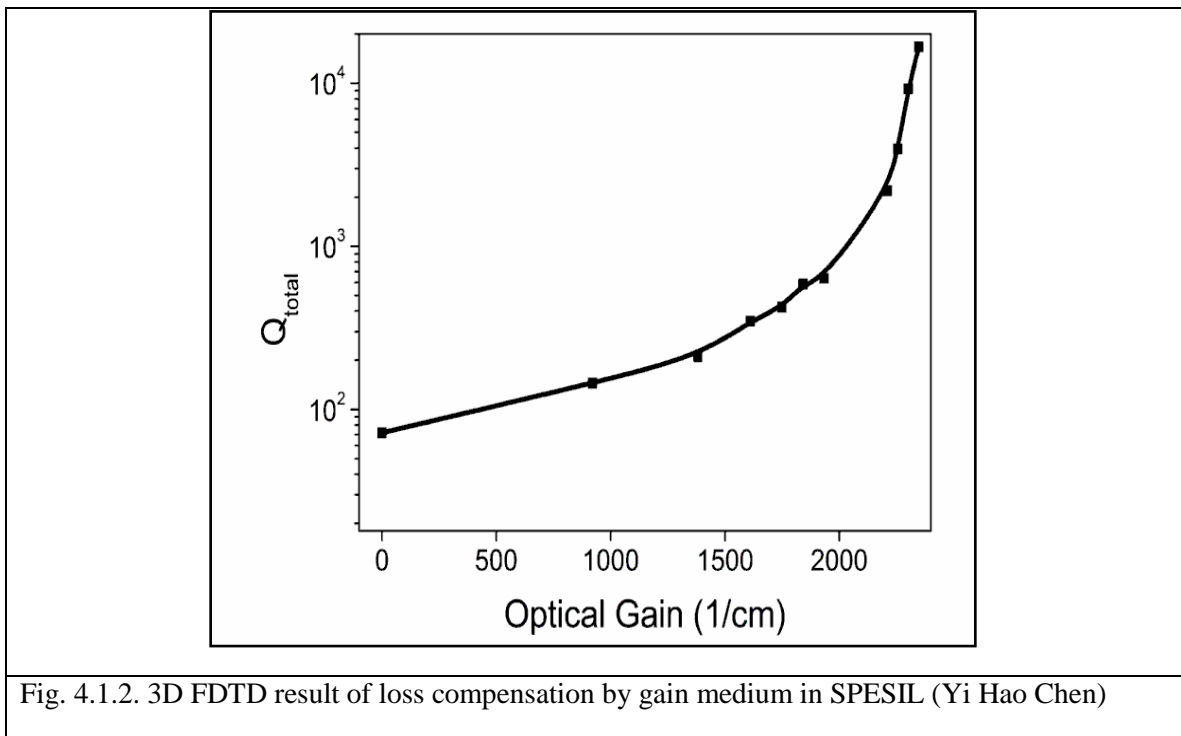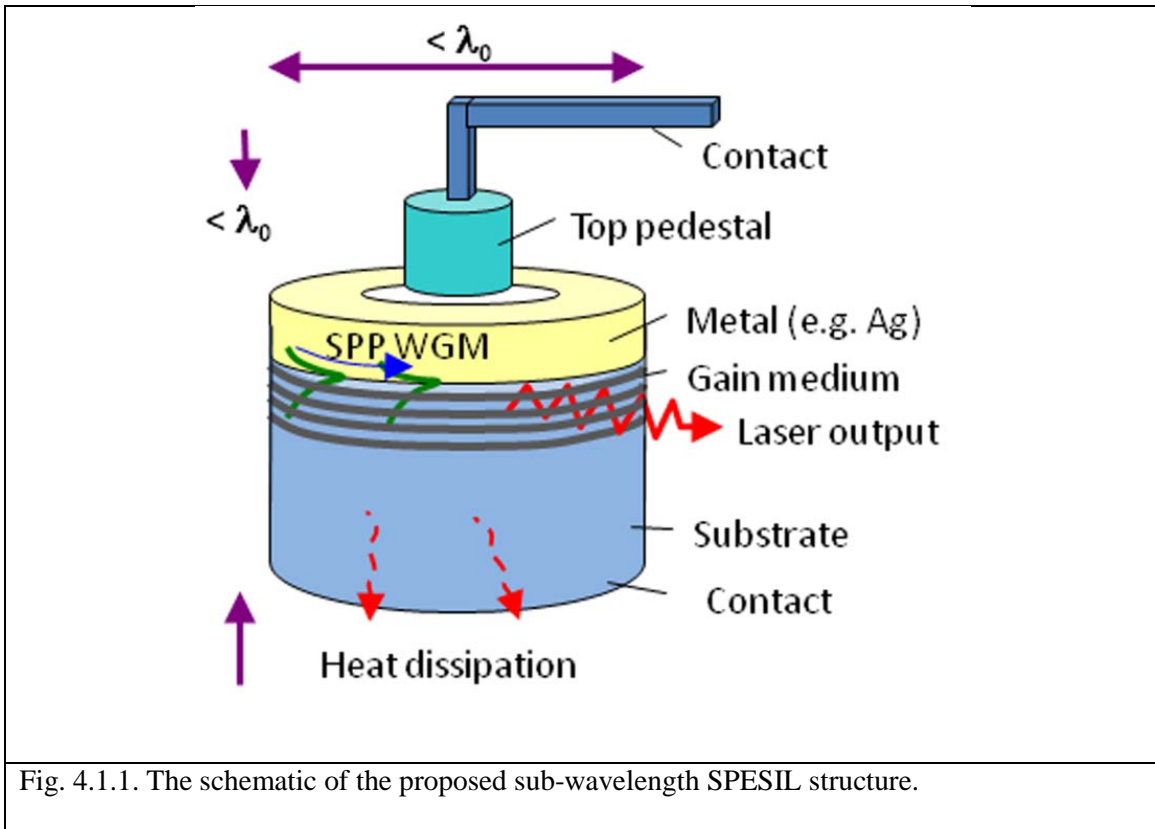
The operation principle of the SPESIL is as follows. First, different SP modes are spontaneously generated, which are, then, amplified by the gain medium. The lasing threshold can be reached once the optical gain compensates all the losses in the cavity, including metal dissipation, optical diffraction, and optical scattering losses. We performed thermal profile calculations in both structures using the finite element method [57] and found that the temperature in the active region of SPESIL was 80 degrees lower than that in a conventional microdisk laser. Better thermal dissipation is critical for laser scaling and room temperature, continuous wave operations. Without the bottom pedestal, the SPESIL structure also has lower electric resistance and optical scattering losses, compared to a conventional microdisk laser. Field confinement in SPESIL has been analyzed by 3D FDTD and is shown in Fig. 4.1.3 (a) and (b). From the figures, one can clearly see that the electric field is confined via WGM laterally and surface plasmon vertically.



(a)          (b)

Fig. 4.1.3 (a) Lateral confinement in SPESIL (b) Vertical confinement in SPESIL (Yi Hao Chen)
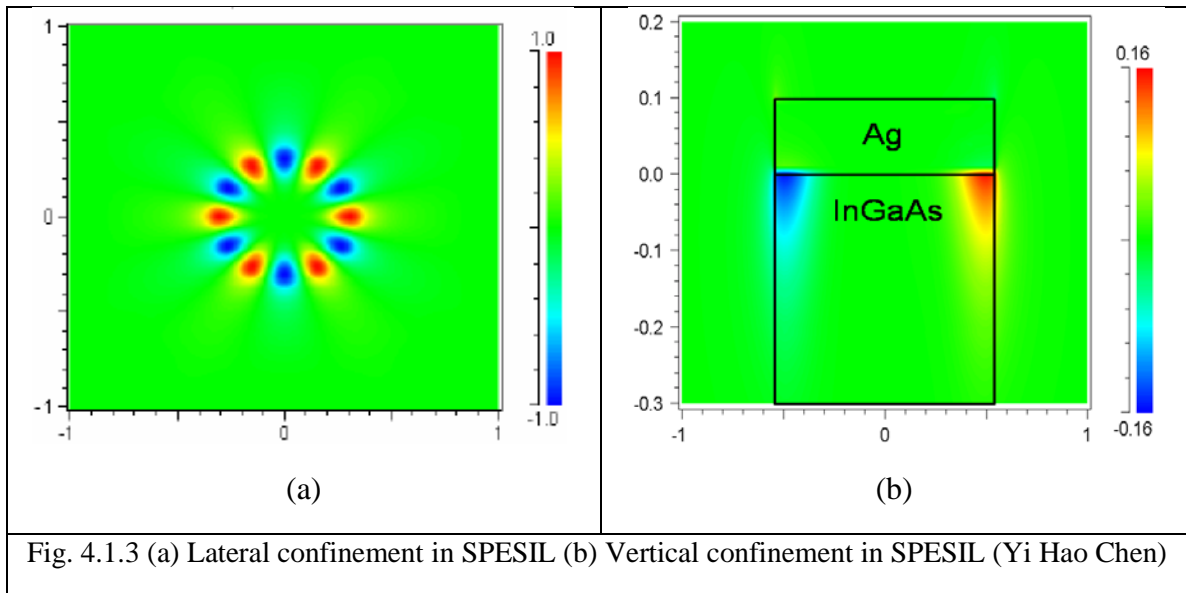
To analyze the SPESIL, we adopted the rate equation approach as follows.

$$\frac{dN}{dt} = \frac{J}{qL_{QW}} - \frac{N}{\tau_N} - vg_{SPP}(N)S \qquad \text{(Eqn. 4.1.1)}$$

$$\frac{dS}{dt} = \Gamma vg_{SPP}(N)S - \frac{S}{\tau_P} + \Gamma\beta R_{sp} \qquad \text{(Eqn. 4.1.2)}$$

Most of the terms in Eqn.4.1.1 and Eqn. 4.1.2 are identical to those in conventional lasers; that is, $N$ and $S$ are electron and photon densities, respectively, $J$ is the injection current, $q$ is the electron charge, $\tau_N$ and $\tau_P$ are the lifetimes of electrons and photons, respectively, $L_{QW}$ is the quantum well thickness, $v$ is defined as $c/n_{eff}$ where $n_{eff}$ is the effective index of the SP mode, $\beta R_{sp}$ is the spontaneous emission, and $\Gamma$ is the optical confinement factor. In Eqn. 4.1.1 and Eqn. 4.1.2, $g_{SPP}$ is the SP gain that includes the metal dissipation loss. We have chosen this approach rather than to include the metal loss as part of the $\tau_P$ term for the reason that the SPP mode profile and hence $\Gamma$ depended on the imaginary part of the metal dielectric constant.

The procedure to determine the modal gain $\Gamma g_{(SPP)}$ is as follows. First, the material gain in the gain medium was calculated for both TM (the dominant component) and transverse-electric (TE) components with a given injection current. The SP mode profile and $\Gamma$ was then calculated using the transfer-matrix method [58]. In this process, the material gain was included in the dielectric constant. The resulting imaginary part of the effective index gave rise to $\Gamma g_{(SPP)}$. Since the metal loss has already been taken into account in the above procedure, it should not be included in the cavity loss again. Hence, cavity loss only includes the diffraction loss, the scattering loss from the periphery of the cavity and top pedestal, and the free carrier absorption. The process described above is shown in Fig. 4.1.4.
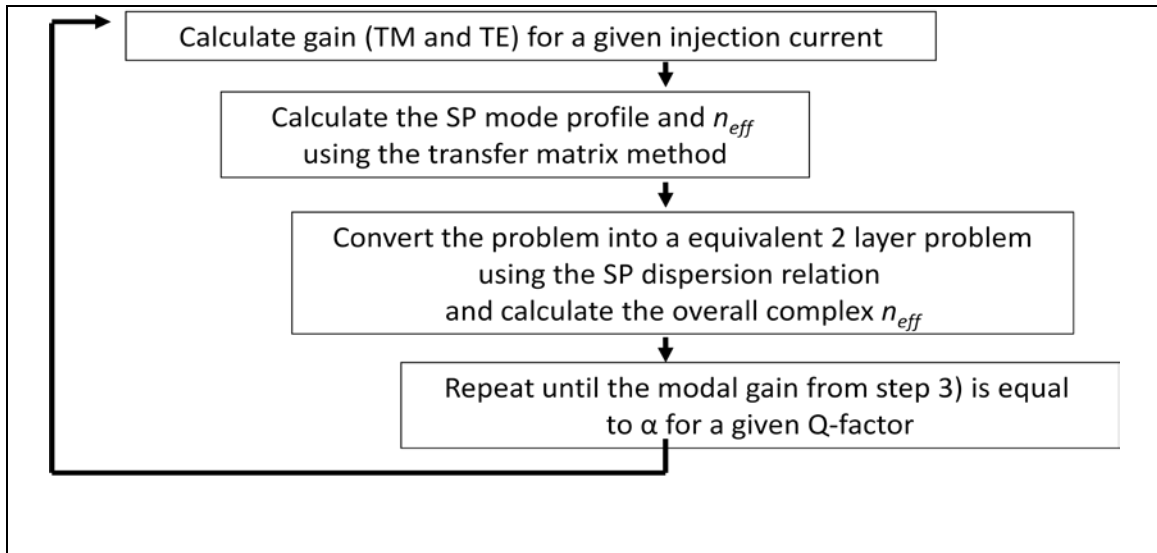
Fig. 4.1.4. Process of simulating threshold current with a given Q factor
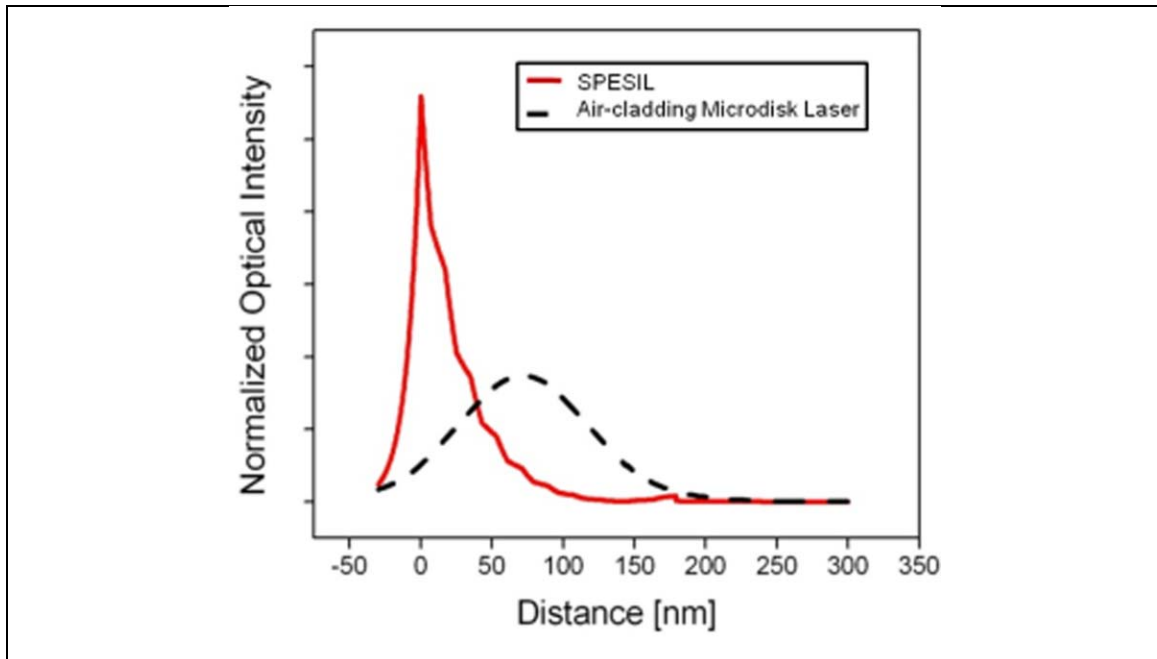


Fig. 4.1.5. The calculated SPP mode profile (solid line) in the SPESIL structure. Also shown is the mode profile in a conventional microdisk laser

As a numerical example, we considered the following structure. It consisted of a silver (Ag) top layer and a GaAs/AlAs (10mm/8nm) multiple quantum well (MQW) gain

region just below it with GaAs as the substrate. Because the SP mode has most of its energy at the vicinity of the metal-dielectric interface, the first AlAs thickness needs to be very small in order to ensure the best overlap between the SP mode and the gain medium. In the following calculations, a 7 nm AlAs barrier layer between the first QW and the Ag layers was used. The calculated SP mode profile is shown in Fig. 4.1.5. The effective index of the above structure is 3.97 as compared to 2.65 for the air-cladding microdisk laser. The higher effective index can allow us to scale down the lateral dimension without sacrificing the cavity Q. This is because, given an actual diameter, optically it is as if the disk is larger with a higher effective index due to the optical wavelength inside the material being smaller. Also, despite the large metal loss, the SPESIL structure can have a large modal gain as it has a much larger $\Gamma$ —around 40% versus a typical $\Gamma$ of ~ 10% for a conventional microdisk laser. Fig. 4.1.6 shows how SPESIL (SP-WGM) scales in comparison to a conventional air-cladding microdisk (TE-WGM and TM-WGM), as calculated by 3D FDTD simulation. For the reasons mentioned above, SP-WGM shows a superior scaling behavior. However, as the diameter ($D/\lambda_o$) gets larger, surface plasmon suffers largely due to metal absorption and, therefore, shows a saturation behavior in $Q_{total}$.
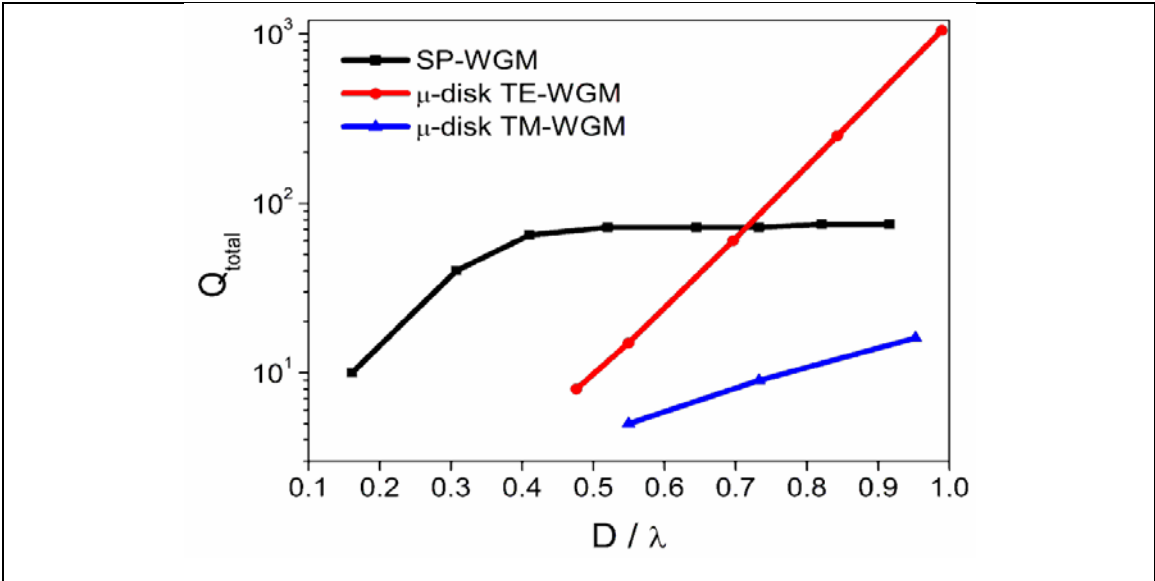
Fig. 4.1.6. Comparison between surface plasmon confined (SP-WGM) and air-cladding confined (TE- and TM-WGM) whispering gallery mode (WGM) cavity resonator's Q vs. diameter (Yi Hao Chen)
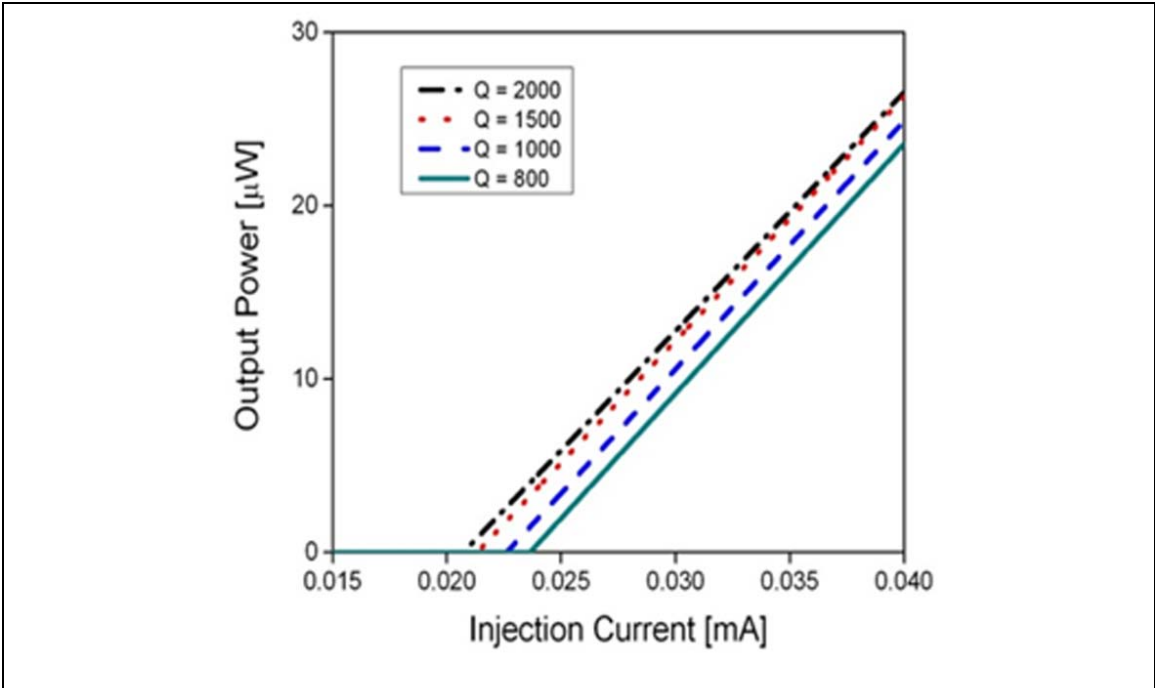


Fig. 4.1.7. Calculated L-I curve for different cavity Q's with five MQWs

Fig. 4.1.7 shows the calculated L-I curves for different cavity Q's. Output power was found using

$$P_{out} = \frac{\hbar\omega}{q} \frac{\alpha_m}{\alpha_m + \alpha_i} \eta_i (I - I_{th})$$  (Eqn. 4.1.3)

In the above expression, $\hbar\omega$ is the photon energy, $\eta_i$ is the internal quantum efficiency, and $\alpha_m$ and $\alpha_i$ are the mirror and intrinsic losses, respectively. We assumed that $\eta_i$ was unity and $\alpha_i$ was equal to a typical value of $\alpha_i$ for GaAs, i.e. 10/cm. $\alpha_m$ was found by using the finite-difference time-domain (FDTD) method. By setting the grid size to be 10 nm to simulate the edge roughness and taking into account the effective index of the SPP mode, we estimated the Q to be around 1100 for a lateral dimension of 0.9 λ where λ was equal to 840 nm. This corresponded to a threshold current of 22 μA. With a higher Q, a lower threshold current can be achieved.

Fig. 4.1.8 shows the calculated threshold current density $J_{th}$ vs. Q for a different number of QWs. At first, as more QWs are added to the structure, there is more overlap between the SP mode and the gain medium that can contribute to the modal gain. However, since the SP mode decays rapidly away from the metal-dielectric interface within the first few QWs, an extra number of QWs will not contribute to the modal gain. In the above structure, the penetration depth of the SP mode on the semiconductor side was calculated to be around 50 nm. This corresponded to the optimal number of QWs to be five.
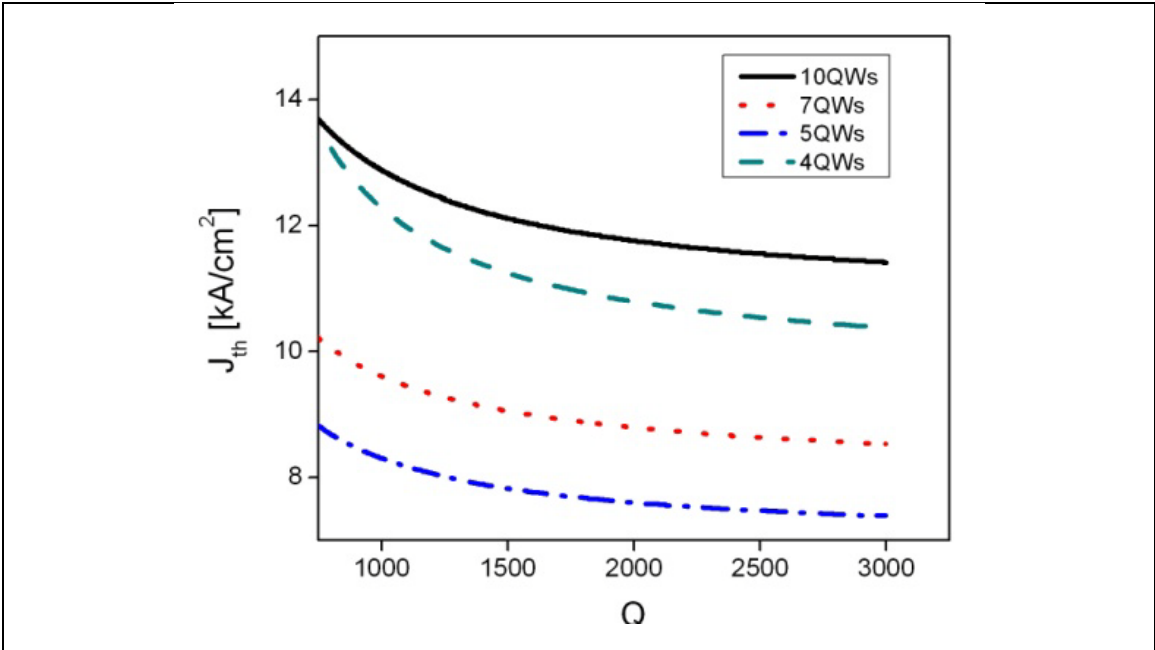
Fig. 4.1.8. Threshold current density $J_{th}$ vs. Q for 4, 5, 7, and 10 MQWs.
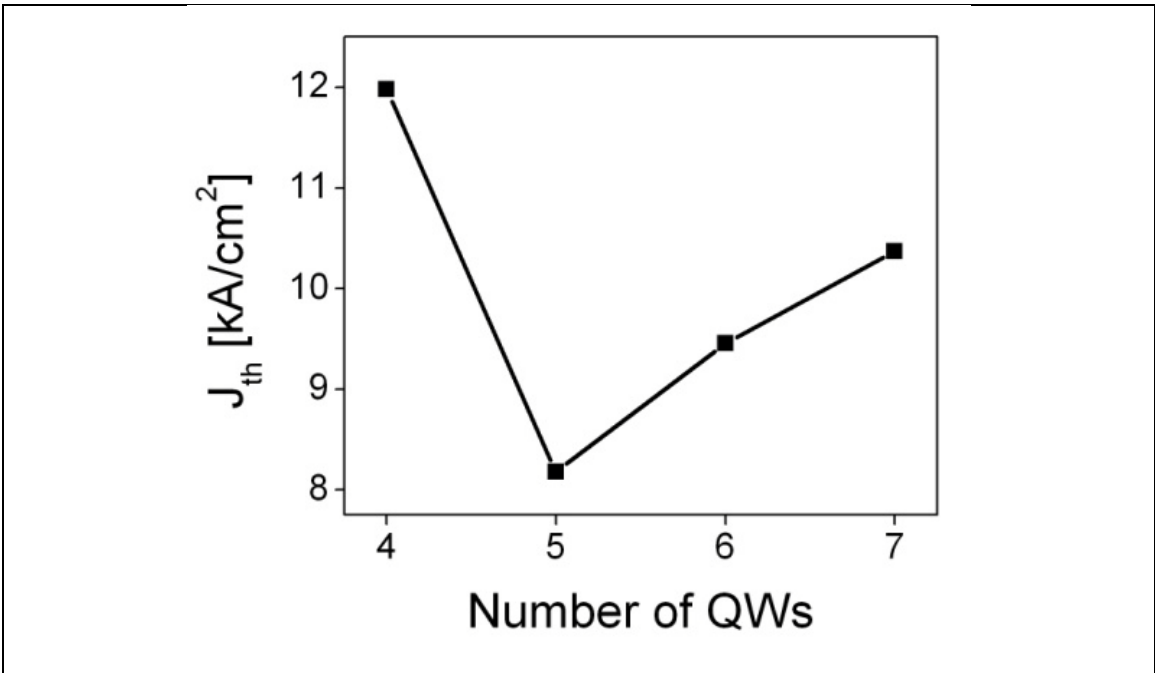


Fig. 4.1.9. $J_{th}$ vs. the number of QWs. A Q of 1100 was used, which was calculated by the FDTD method.

## 4.2 Experimental Demonstration of Linewidth Narrowing

Since no probe laser was required as in the waveguide experiment, a different sample consisting of tensile-strained InGaAs/InAlGaAs MQWs was chosen in this experiment to provide an optimized TM gain component that can most effectively compensate the metal loss. The sample was grown by molecular beam epitaxy (MBE) on a (001) n+InP substrate. The MQWs consist of four pairs of tensile-strained $In_{0.43}Ga_{0.57}As$-$In_{0.53}Al_{0.22}Ga_{0.25}As$ heterostructures, as shown in Fig. 4.2.1 (a). The thicknesses of the quantum well and barrier are 5 and 10 nm, respectively. The top barrier layer is reduced to 8 nm to maximize the overlap between the SP-WGM and the MQWs.



(a)                                                                           (b)

Fig. 4.2.1. (a) Layer design of InP-based QW wafer used in the SPESIL experiment (b) Scanning electron micrograph of a SPESIL device (1400nm in diameter) (Fabrication done by Yi Kuei Wu)
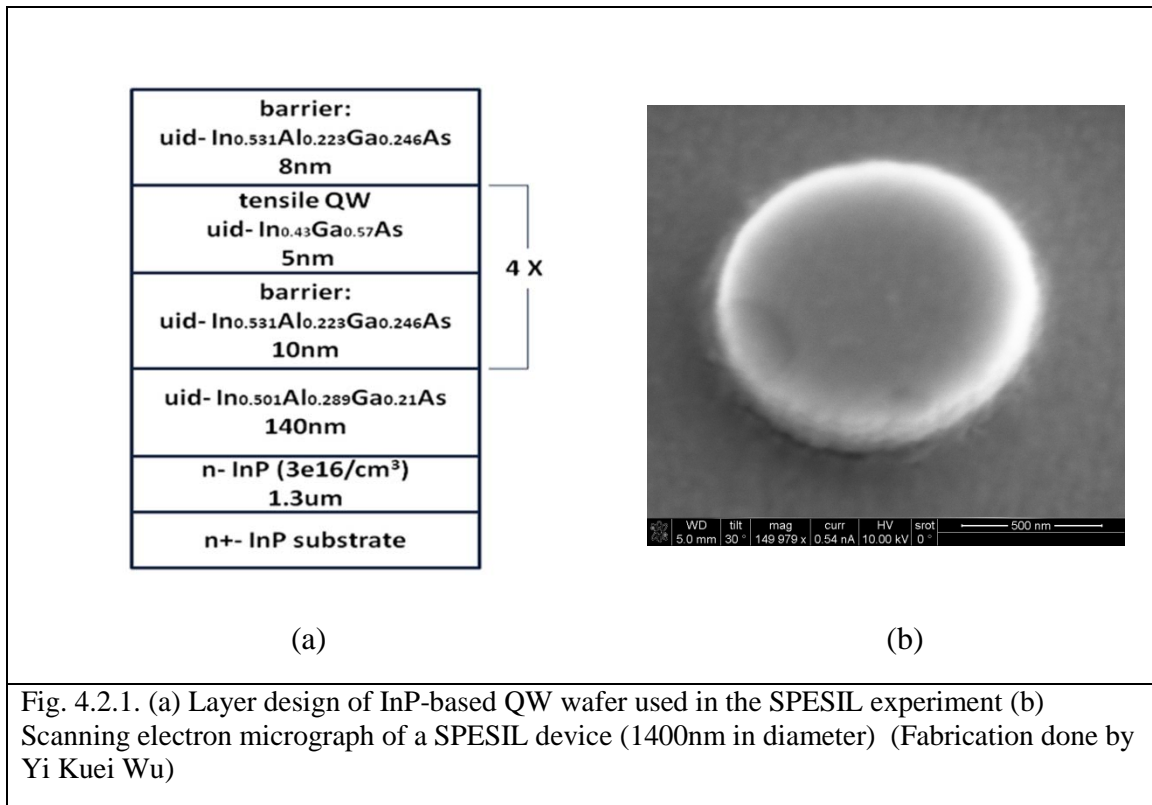
The micro-pillar device structure was formed by electron beam (e-beam) lithography and wet chemical etching of the MQW heterostructure. After spin-coating of PMMA and e-beam lithography, 150 nm of silver and 30 nm of nickel were deposited using e-beam evaporation, followed by lift-off. The nickel layer was used as an etch mask for the subsequent wet etching using $H_2SO_4$:$H_2O_2$:$H_2O$ (1:1:32). The etching rate was controlled to be 3nm/s and the total etching depth is 100 nm. To prevent silver oxidation and to passivate the MQW surface, a thin layer (40nm) of $SiO_2$ was deposited by plasma-enhanced chemical vapor deposition (PECVD) immediately after the wet etching. Wet etching was chosen to ensure a smooth sidewall in order to minimize scattering losses. Fig. 4.2.1 (b) shows the scanning electron micrograph (SEM) of a 1400 nm-diameter SPESIL.



Fig. 4.2.2. Micro-photoluminescence measurement
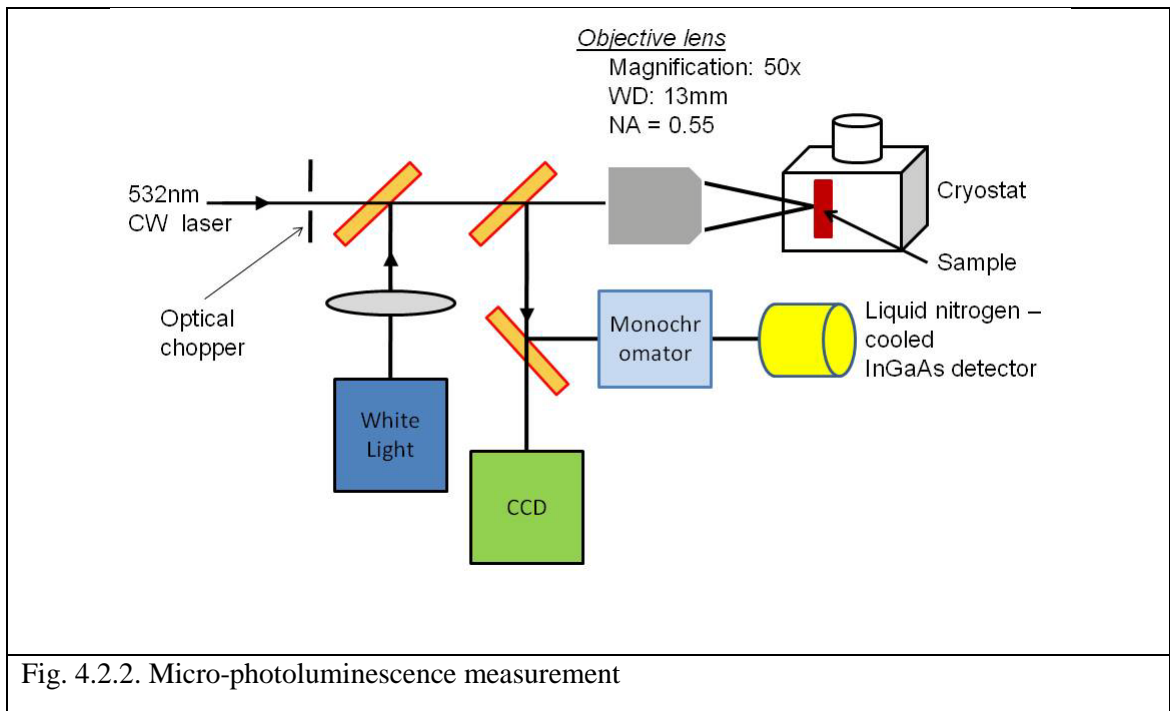
The measurement was performed with the substrate kept at 10K to minimize non-radiative recombination processes. A standard μ-PL was used with a 532 nm wavelength CW pump laser. The polarization of the pump laser is in parallel to the surface of the micro-pillar. The spontaneous emission was collected by an objective lens with a numerical aperture of 0.55, which was subsequently dispersed by a 0.5-m focal-length Princeton-Acton monochrometer and detected by a cooled InGaAs photodetector using a lock-in amplifier. Measurement schematic is shown in Fig. 4.2.2. Because of the proximity (8 nm distance) of the MQWs to the thick metal layer (180 nm total), the only optical mode that can propagate and be confined in the cavity is the SP-WGM mode as confirmed by 3D-FDTD calculations. Previously, it has been shown that part of the spontaneous emission can be coupled to SPs. Hence, by measuring the linewidth of the spontaneous emission versus the pump power, we can expect a linewidth reduction if the cavity-Q is enhanced. The results are shown in Fig. 4.2.3 (b), comparing four different pillar sizes. It can be seen that as the pump power increases, the linewidths of all four pillars increase initially. This increase is attributed to thermal broadening which is consistent with a red-shift of the peak wavelength observed in Fig. 4.2.3 (a). As the pump power is further increased, the linewidths of the two larger pillars continue to increase while the linewidths of the two smaller pillars start to decrease. The linewidth of the smallest pillar (with a $D/\lambda$ ratio of 0.9) starts to decrease first with the pump power. According to Fig. 4.2.3 (a), the two smaller pillars also experience a blue shift in their peak wavelengths, showing signs of microcavity effect.
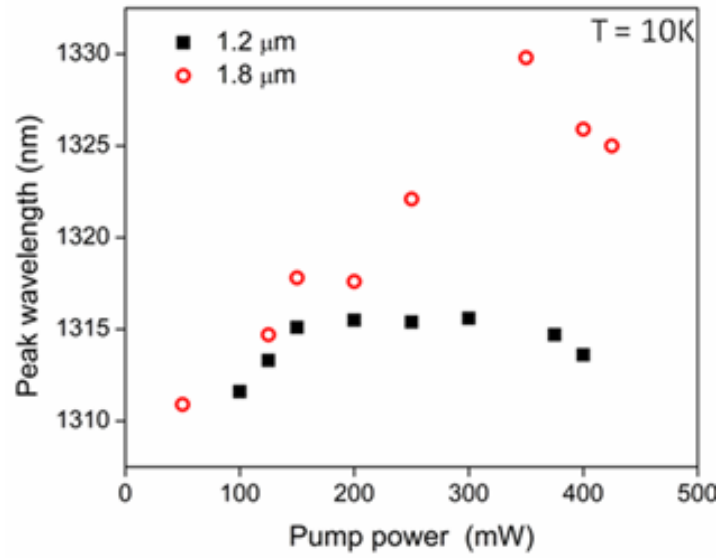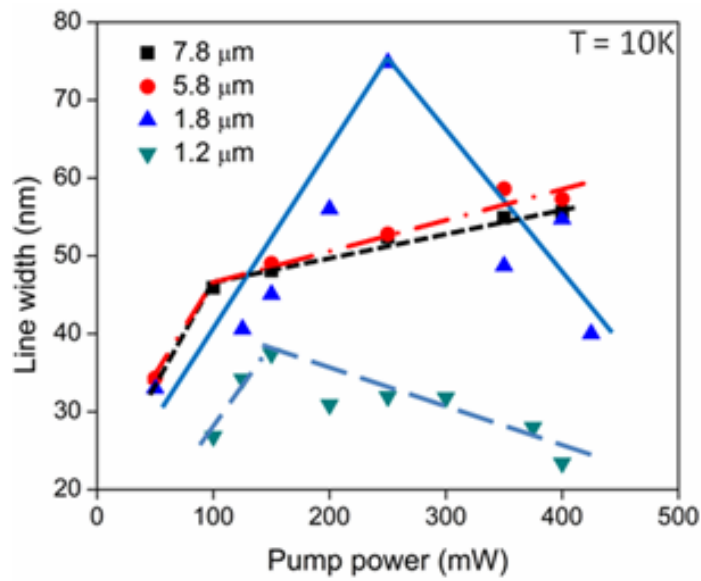
Fig. 4.2.3 (a) PL peak wavelength versus pump power for 1.8 μm and 1.2 μm diameter devices.
(b) PL linewidth versus pump power for 7.8 μm, 5.8 μm, 1.8 μm and 1.2 μm devices. Solid
lines are for visual guidance only

In the experiment, the cavity-Q factor of the SP-WGM can only be observed if it becomes greater than the quality factor corresponding to the spontaneous emission linewidth. The thermal broadening decreases this quality factor and enables the cavity-Q enhancement to be more easily observed. The calculated cavity-Q factors for surface plasmon micro-pillars with $D/\lambda$ ratios > 0.9 are around 60 according to Fig. 4.1.6 . For $D/\lambda > 1$, the cavity-Q factor is limited by the metal absorption loss and remains nearly a constant. Because larger cavities possess larger MQW volumes, the total optical power required to enhance the cavity-Q factor to an observable level increases with the cavity size. The largest cavity-Q factor we have observed was 66 from the $D/\lambda = 0.9$ sample (cavity diameter 1.2 μm). A further increase of the cavity-Q factor has not been observed with increasing pump power due to sample damage.

## 4.3 Summary

In this chapter, a surface plasmon laser, named surface plasmon-enabled semiconductor injection laser (SPESIL), was explored both theoretically and experimentally. The effective index of SPESIL was 3.97 as compared to 2.65 for the air-cladding microdisk laser. The higher effective index can allow us to scale down the lateral dimension without sacrificing the cavity Q. Also, despite the large metal loss, the SPESIL structure can have a large modal gain as it has a much larger $\Gamma$ —around 40% versus a typical $\Gamma$ of ~ 10% for a conventional microdisk laser. Due to the above reasons, SPESIL can be scaled down to sub-wavelength dimensions in all three directions. Using a

rate-equation based laser model, we showed that a sub-wavelength dimension SPESIL exhibits a threshold current of 25 μA at room temperature with five quantum wells in the active region.

Using a μ-PL measurement scheme, the gain-assisted cavity-Q enhancement has been demonstrated in a sub-wavelength surface plasmon micro-pillar cavity. A cavity-Q factor of 66 was observed in a $0.9\lambda$-diameter cavity, which was larger than the passive cavity-Q factor calculated using 3D-FDTD calculations for the same cavity under no optical excitation. However, upon further increasing the pump power, the resonant cavities were overheated and damaged. Therefore, we concluded that the metal loss was too great to overcome even with whispering gallery mode round trip gains.

# CHAPTER 5

# Hybrid Dielectric/Plasmon Metal-clad Nanoring Laser

## 5.1 Hybrid Dielectric/Plasmon Optical Confinement

In the previous chapter, pure surface plasmon has been demonstrated to generate too much metal loss in an optical resonant cavity such as the SPESIL to result in lasing. In Chapter 3, we demonstrated partial compensation of metal loss by a gain medium placed in close proximity to the metal/semiconductor interface; however, total compensation of loss was still proven to be challenging in a surface plasmon resonant cavity.

With the presence of metal, optical modes can take on various shapes: pure surface plasmon mode or and hybrid dielectric-plasmonic mode. State-of-the-art hybrid dielectric-plasmonic lasers include bowtie cavity lasers, metal-clad nanopillar and Fabry-Perot lasers [33,34], and plasmonic nanowire lasers [35]. Examples of pure surface plasmon nanolasers include spacer-based nanolasers [37], and surface plasmon-enabled sub-wavelength injection laser (SPESIL). In all of the above cases, use of metal increases absorption loss significantly, with pure surface plasmon cavities suffering the greatest metal loss owing to the large overlap between the lasing mode and the metal.

However, by shifting the peak of the electric field away from metal, the hybrid dielectric-plasmonic modes are able to lessen the burden of metal loss. Of course, since electric field does not decay exponentially inside dielectric, the hybrid mode requires a larger laser cavity. Hence the trade-off needs to be understood in order to optimize the semiconductor laser structures while scaling.

## 5.2 Metal-clad Semiconductor Nanoring Laser

There are two types of hybrid dielectric-plasmonic optical modes: standing wave and traveling wave. Of the two hybrid dielectric-plasmonic modes, traveling wave optical modes are more attractive for on-chip operation because they require no extra gratings or mirrors. For this reason, most of state-of-the-art integrated optical components currently utilize whispering gallery mode, a type of traveling wave optical mode. A prime example of such cavity is a semiconductor ring resonant cavity. Semiconductor ring lasers (SRLs) possess several advantages that are critical for photonics integration. [59,60] These are in-plane orientation for easy coupling to output waveguides and capability of controlling emission wavelength and laser dimension independently. In addition, the SRLs can exhibit bistability due to de-generate clockwise and counter-clockwise modes. This bistability has been exploited for the on-chip optical memory application [61-63].

As useful and beneficial as SRLs are for on-chip operation, it has been difficult shrinking their device dimensions due to increased diffraction loss, as their bending angle becomes larger. Therefore, a mechanism must be developed which would increase the

optical confinement and reduce the bending loss. One method is to use metal to confine electric field inside the semiconductor more tightly. A ring resonant cavity, named metal-clad semiconductor nanoring laser, which takes advantage of hybrid dielectric/plasmon mode, is given in Fig. 5.2.1.



Fig. 5.2.1. Side view of the sub-wavelength ring laser. The semiconductor ring is covered with metal everywhere.
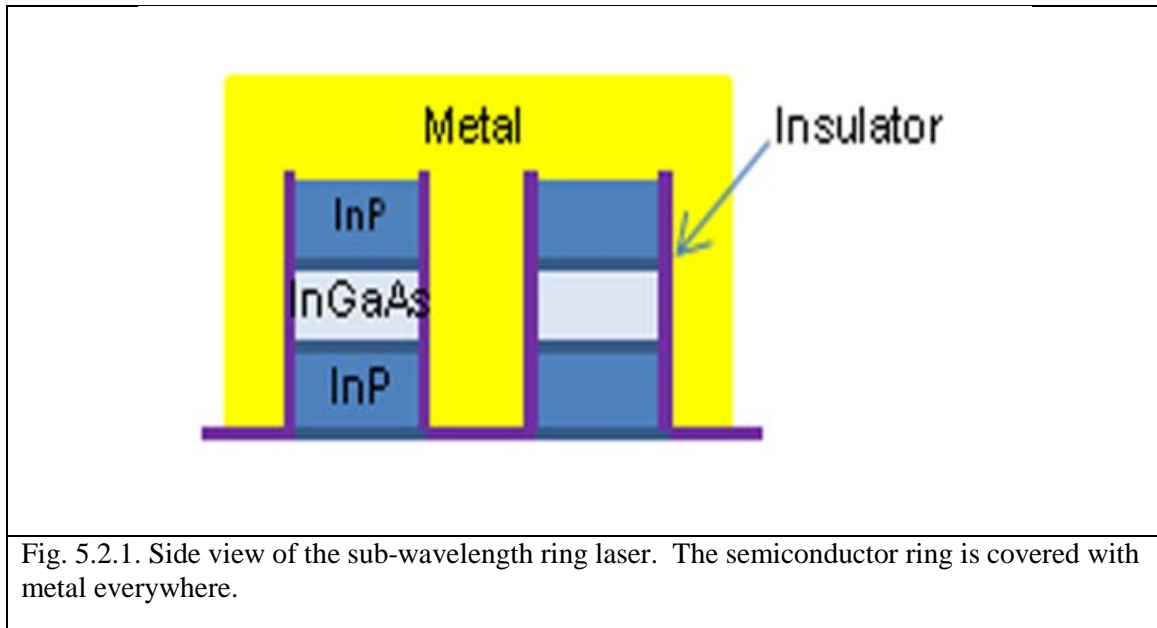
The ring resonator exhibits superior scaling properties and possesses desired features for on-chip integration. The metal-clad semiconductor nanoring laser is also expected to preserve the advantages of their metal-free microring laser counterpart while enabling scaling to the sub-wavelength dimension. In addition, the small laser dimension can considerably increase the free-spectral range, allowing single longitudinal operation to be attained without additional feedback structures. Additionally, as will be shown experimentally, their lasing wavelength can be fine tuned using the ring width with the diameter kept constant.
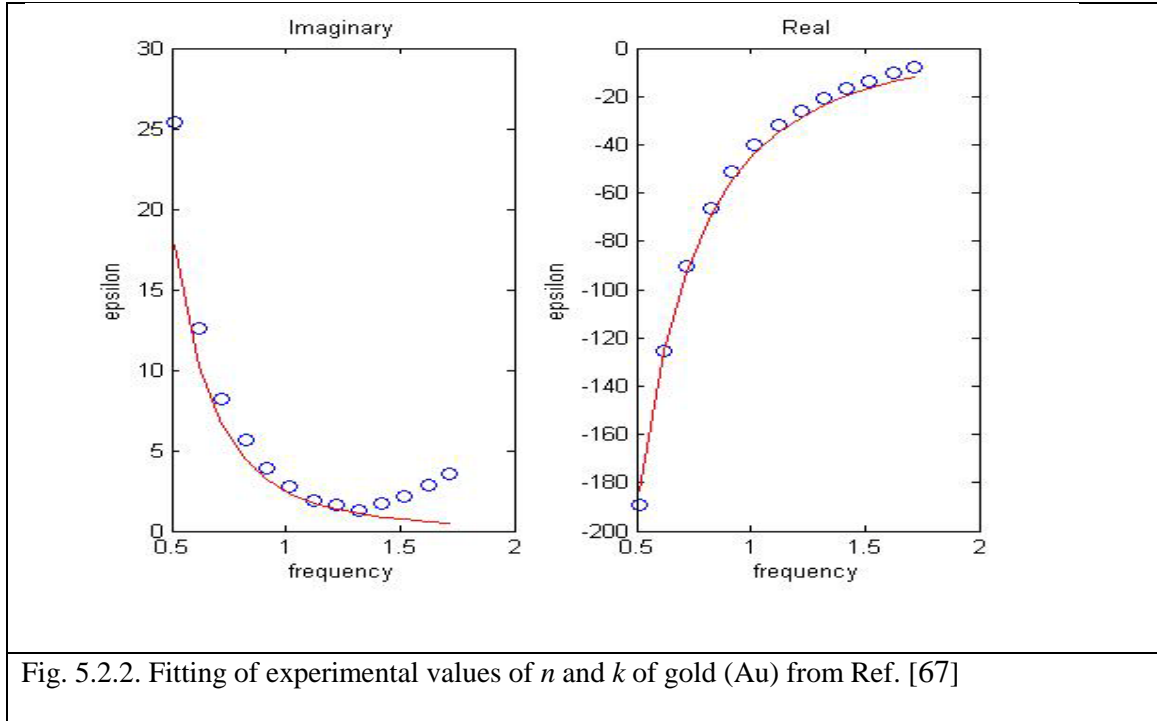
Fig. 5.2.2. Fitting of experimental values of *n* and *k* of gold (Au) from Ref. [67]

The sub-wavelength nanoring laser can be formed by conformally depositing a metal layer over a semiconductor ring structure. The metal enables tight optical confinement and improves heat conduction of the device, resulting in a device that can be scaled to sub-wavelengths in all three directions. Fig. 5.2.3 (a) and (b) show the lateral and transverse optical modes, respectively. The radial mode profile shows the hybrid nature of dielectric and surface plasmonic confinement as manifested by the electric field profile near the metal-semiconductor interface. The transverse mode is from the conventional dielectric confinement with the active region acting as the waveguide core. Simulations were performed using MEEP, which is a finite-difference time-domain (FDTD) simulator [64]. Cavity resonant frequencies were calculated using the filter diagonalization method [65]. To reach the lasing threshold, the optical gain must overcome all the losses including metal absorption, diffraction, and scattering loss. In

our simulations, the scattering loss is simulated by the grid size of the FDTD calculations, 12nm. Because the optical mode propagates parallel to the substrate in this device, the laser output is expected to be primarily from the circumference of the ring via diffraction and scattering losses. Experiment parameters of $n$ and $k$ of Au from Ref. [67] were fitted as shown in Fig. 5.2.2, and used in MEEP.



(a)



(b)
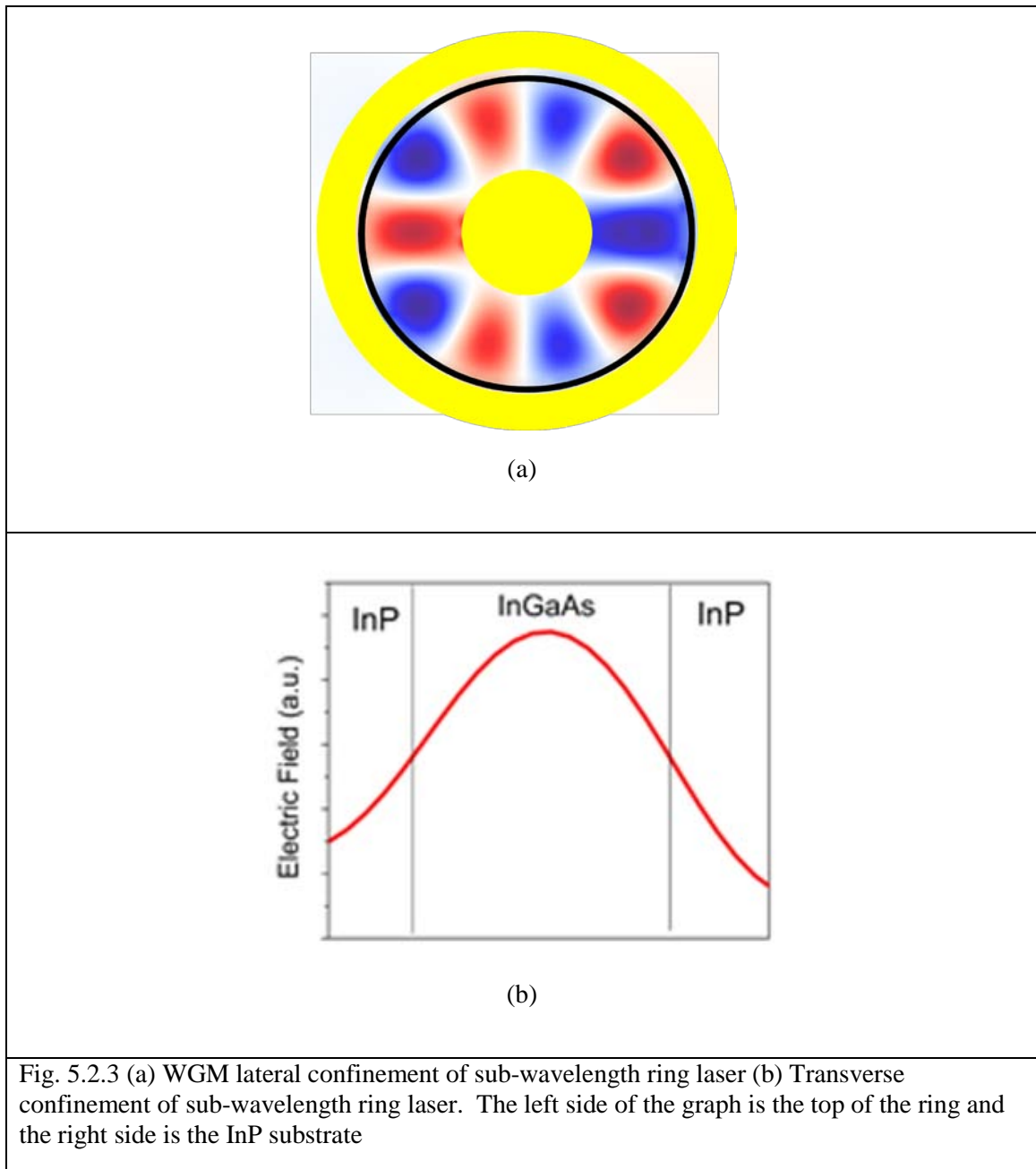
Fig. 5.2.3 (a) WGM lateral confinement of sub-wavelength ring laser (b) Transverse confinement of sub-wavelength ring laser. The left side of the graph is the top of the ring and the right side is the InP substrate

**Scaling**

To show that the metal-clad nanoring laser indeed exhibits a superior scaling property, Fig. 5.2.4 compares the cavity Q factors versus the device dimension, normalized to the free-space wavelength $\lambda_0$, for the three metal-clad nanolaser structures—the nanoring, nanopillar, and SPESIL—and the conventional microdisk laser. In SPESILs, the transverse mode is a pure surface plasmon mode whose propagation loss is limited by the metal loss rather than by the diffraction loss for a device dimension greater than $0.5\lambda_0$. As a result, the cavity Q factor in a SPESIL structure shows a saturation behavior even with an increasing device size for $D/\lambda_0 > 0.5$ where $D$ is the device diameter. Although the diffraction loss is even larger in this regime as shown by the cavity Q factor of the microdisk laser, the combination of dielectric and metal confinement can considerably increase the cavity Q. This is attributed to better dielectric confinement as a result of the metallic interface which suppresses the diffraction loss. Both metal-clad nanopillar and nanoring lasers show benefits of the hybrid dielectric/plasmon mode. But owing to a more flexible design, the nanoring laser shows a superior scaling property compared to the nanopillar laser.

Fig. 5.2.4. Cavity Q factor vs. D/λo for metal-clad nanoring laser (called subwavelength ring on plot), metal-coated pillar laser and SPESIL, as well as conventional air-cladding microdisk laser. Lines are for visual guidance only.
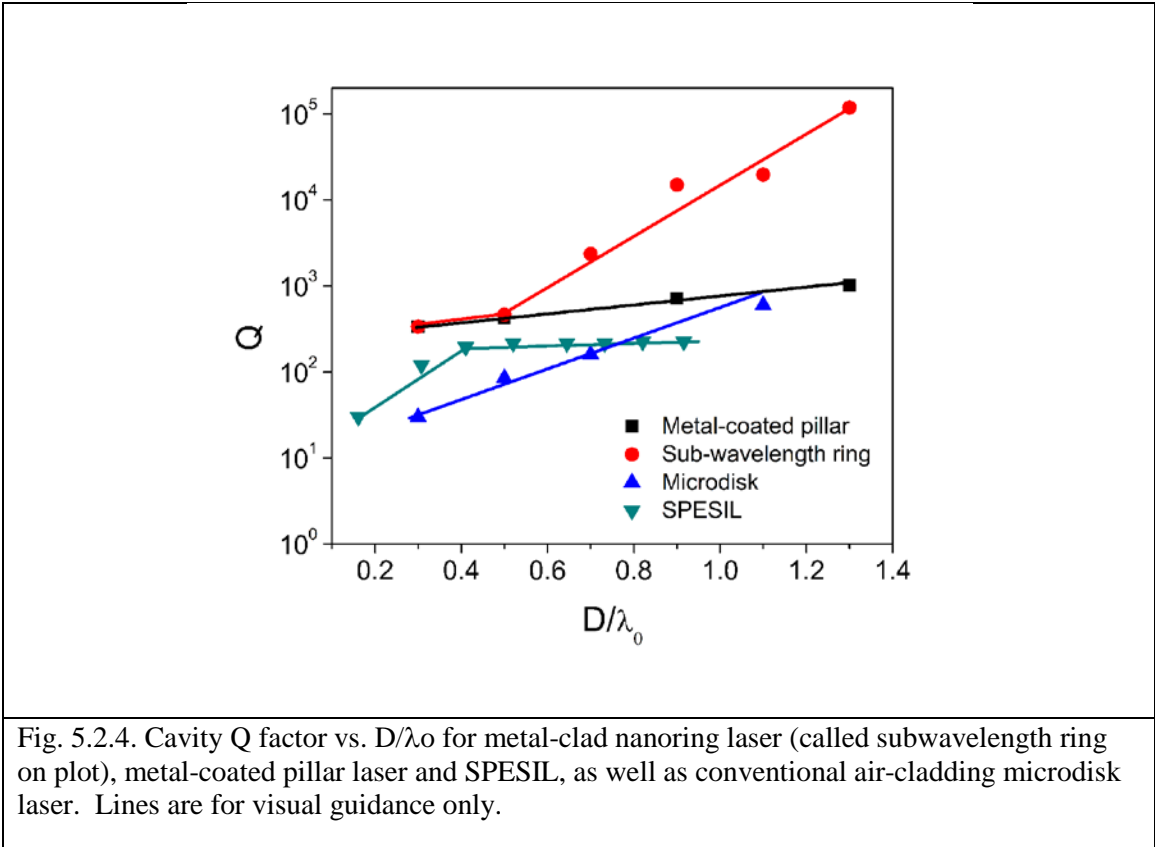
**Independent Control of Resonance Wavelength and Cavity Quality Factor**

The metal-clad nanoring laser has two design parameters—the ring diameter and ring width—which allow independent control of the resonance wavelength and cavity Q factor. Fig. 5.2.5 (a) shows how cavity Q factor changes for various ring widths given a ring diameter for the resonance wavelength of 1μm. It can be seen that the cavity Q can be optimized at a different ring width for a given laser dimension. The simultaneous optimization of the cavity Q factor and control of the resonance wavelength is critical for the practical applications of nanolasers. Without such a capability, it will be extremely difficult to fix the output wavelength of a nanolaser due to the large free spectral range that is typical for a nanolaser. According to Fig. 5.2.5 (a), as the laser dimension becomes larger, the optimal ring width also becomes larger. For example, the optimal ring width for a 700nm diameter laser is 125nm whereas that for a 900nm diameter laser is 200nm. However, as the optimal nanoring laser design below 500nm diameter becomes a nanopillar laser, this trend disappears for smaller devices. Fig. 5.2.5 (b) shows how tolerable a nanoring laser of a given diameter is to non-optimal ring widths. As the ring diameter increases, ring width tolerance for FWHM of cavity Q factor decreases significantly. For ring diameter equal to 700nm, the Q decreases to half of the maximum value within 50nm on either side of the optical ring width. However, as the diameter increases to 1100nm, the tolerance is only 10nm on either side. Therefore, there is a stricter design requirement for a larger diameter sub-wavelength ring laser.
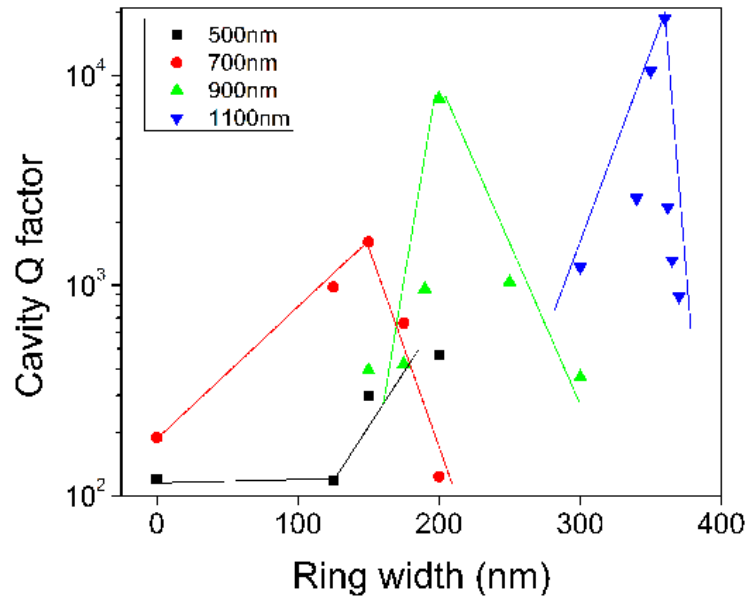
(a)
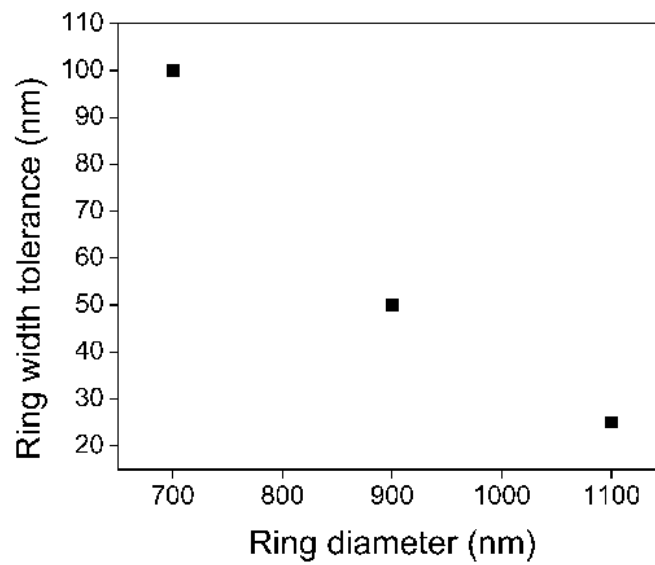


(b)

Fig. 5.2.5 (a) Cavity Q factor vs. ring width for 4 different ring diameters. $\lambda_{res} = 1\mu m$ (b) Ring width tolerance for FWHM of Q factor in nm for a given ring diameter. Lines are for visual guidance only.

**Metal Thickness**

As mentioned above, a metal-clad nanolaser exhibits better photon confinement than a microdisk laser does owing to the metal confinement. It is, therefore, important to optimize the metal layer thickness. As shown in Fig. 5.2.6 (a), when the metal layer is too thin, the optical mode cannot be tightly confined inside the semiconductor region, causing more metal absorption and diffraction losses and resulting in a low cavity Q factor. As the metal layer thickness increases, more and more field is confined inside the semiconductor, therefore increasing the cavity Q. Fig. 5.2.6 (b) shows the electric field profiles with 3 different metal layer thicknesses (50nm, 90nm and 200nm). In Fig. 5.2.6 (b), x = 0 denotes the center of the ring and the semiconductor region is located between x = -200nm and -400nm. Due to the boundary condition and the exponentially decaying electric field profile inside the metal, more electric field lies within the semiconductor for devices with a thicker metal coverage. Furthermore, with a thinner metal thickness such as 50nm, the optical mode is concentrated more toward the inner perimeter of the ring. Because the grid size used in FDTD calculations, 12nm, simulates the surface scattering loss, this causes a higher loss for a ring with a thinner metal thickness.
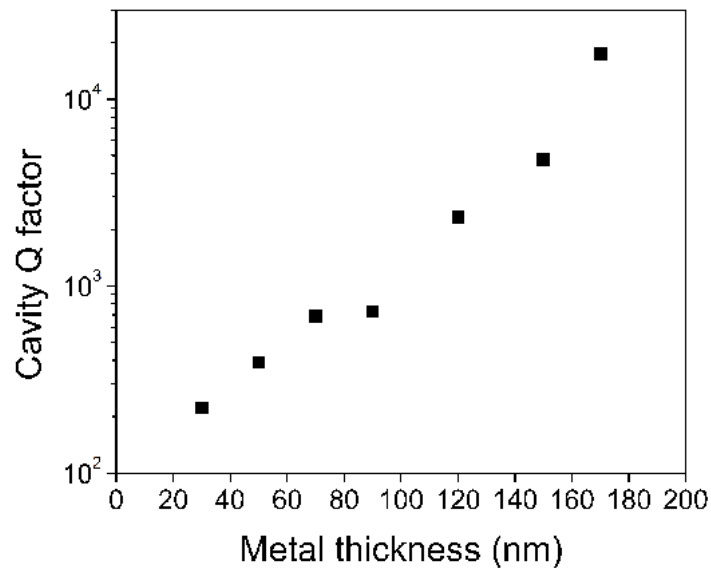
(a)
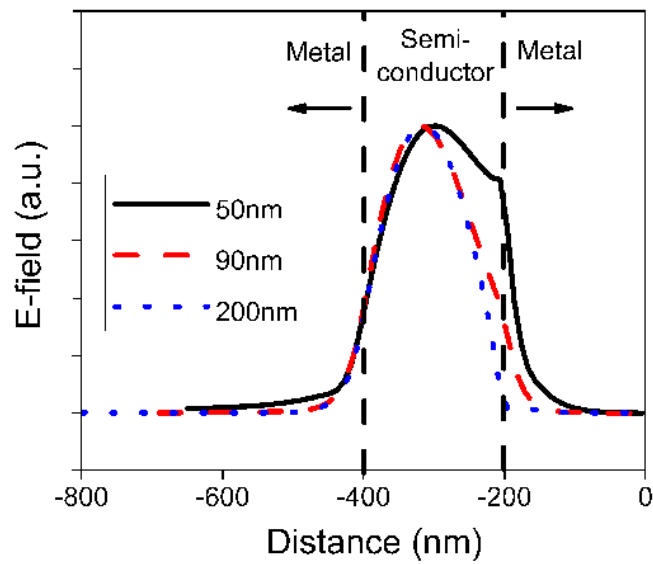


(b)

Fig. 5.2.6. (a): Cavity Q factor vs. metal thickness for semiconductor (excluding metal thickness) ring diameter = 800nm and ring width = 200nm. Resonance = 1μm. (b): E-field profile with varying metal thickness.

**Output Coupling**

Conventional semiconductor lasers use bulky optics for output coupling into an optical waveguide. An ideal nanolaser must have a nanoscale output coupling scheme so that it can be easily integrated with other nanoscale optoelectronic components. In order to achieve this, an opening in the metal layer at the outer edge of the nanoring cavity can be introduced and an optical waveguide can be inserted from such an opening. To keep the opening as small as possible, the beginning segment of the output waveguide can also be metal-clad to improve confinement. The same output coupling scheme can be used in the nanopillar laser structure too. Inevitably, the output coupling of a nanolaser is going to decrease the cavity Q factor. Fig. 5.2.7 (a) and (b) show the cavity Q factors of both the nanoring and nanopillar lasers versus the width of the output waveguide. It can be seen that the nanoring laser exhibits a higher cavity Q factor than the nanopillar laser does with output waveguides attached to them for all sizes. In addition, a smaller nanoring laser has a better tolerance to the perturbation created by the presence of a waveguide. This is attributed to the results shown in Fig. 5.2.5 that a larger nanoring laser has a more stringent design requirement.
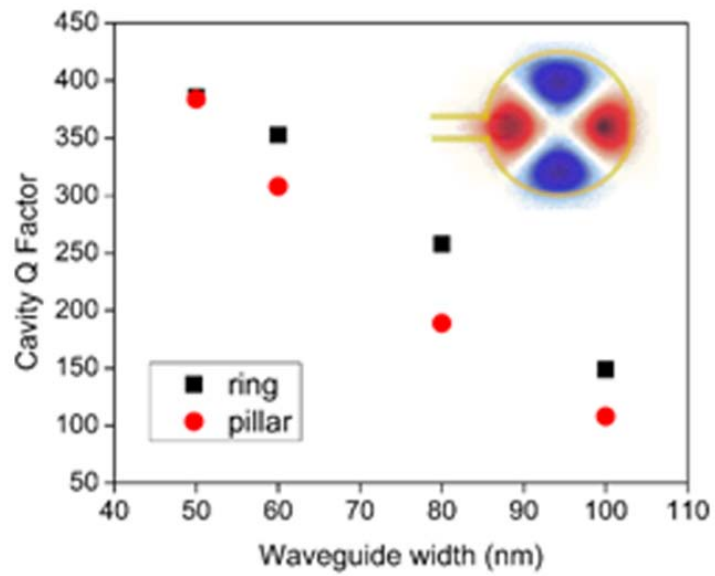
(a)
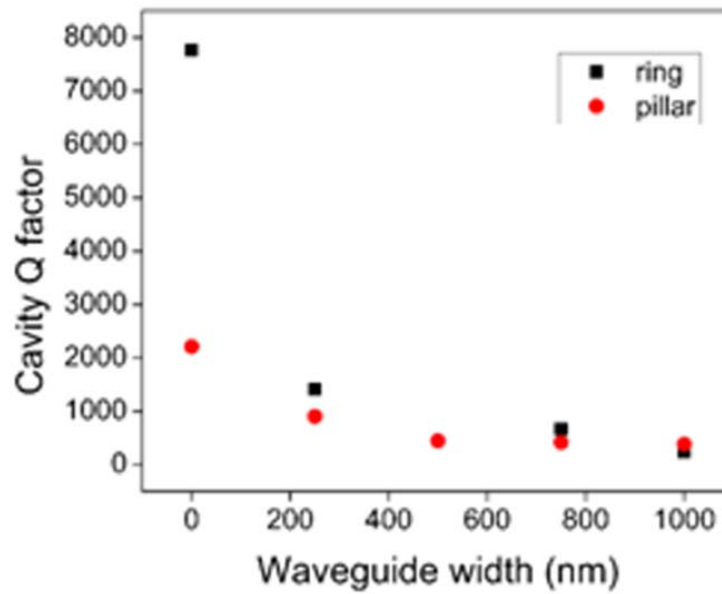


(b)

Fig. 5.2.7 (a): Cavity Q factor vs. waveguide width for $D/\lambda_o = 0.6$ and ring width = 150nm.
(b): Cavity Q factor vs. waveguide width for $D/\lambda_o = 0.9$ and ring width = 200nm

## 5.3 Experimental Results on Micro-sized Metal-clad Ring Laser

Semiconductor microring resonators have been widely used as the fundamental building block for photonic integrated circuits. [68-70]  Semiconductor lasers employing microring cavities exhibit unique advantages that include traveling-wave cavities without a need for additional feedback structures such as mirrors, convenient out-coupling to in-plane waveguides, and independent control of the emission wavelength from the device size.  Furthermore, nanoscale ring lasers can enable single longitudinal mode operation and tighter integration between electronic and photonic components.  To date, however, physical dimensions of state-of-the-art microring lasers remain at diameters greater than 7.5 $\mu$m [71].  In this section, we experimentally demonstrate that the integration of the metal and the ring resonator can lead to the coherent oscillation in a 4-$\mu$m diameter ring resonator that was otherwise difficult to attain previously.

Metal surrounding the semiconductor enhances the optical confinement since the electric field rapidly goes to zero inside the metal.  The lateral and transverse optical modes are purely dielectric and hybrid dielectric-plasmonic in nature, respectively.  The hybrid nature of the transverse optical mode provides an enhanced optical confinement, although at the loss of increased metal dissipation.  This section focuses on the experimental demonstration that showed an increased cavity quality (Q) factor as a result of enhanced optical confinement due to the metal cladding, which outweighed added metal loss.  Therefore, the metal cavity can provide a feasible pathway for continued scaling of a microring laser.

Lasing in a metal-clad microring resonator has been experimentally demonstrated as follows. InGaAsP/InP epiwafer was grown by metal-organic chemical vapor deposition (MOCVD), as shown in Fig. 5.3.1(a). All layers are lattice-matched to InP and the index contrast provide the necessary vertical confinement. Room temperature photoluminescence peak wavelength is 1.5μm. The two InP layers serve as waveguide cladding layers for transverse optical confinement. The top $n^+$-InGaAs and bottom $p^+$-InGaAsP were also included for future electrical injection. The device was patterned by e-beam lithography and reactive ion etching. Raith 150 electron-beam lithography system was used to define the rings using bi-layer PMMA structure to enhance the subsequent lift-off process. MicroChem 495K A6 PMMA develops away faster than MicroChem 950K A2 PMMA, thereby providing a negative angle for lift-off. 50nm of titanium (Ti) was deposited using electron beam evaporation and lifted off in acetone. Using Ti as the mask, InGaAsP/InP epiwafer was dry etched in $CH_4/H_2/Ar$ (4sccm/28sccm/14sccm) environment, in PlasmaTherm 790. The pressure and power were maintained at 30mTorr and 200W, respectively. During the InP etching, polymer is deposited as a byproduct and is removed using an $O_2$ ashing cycle (70sccm, 200mTorr, 100W, 3 minutes). A scanning electron micrograph showing the device after the aforementioned etching step is in Fig. 5.3.1 (b). Afterward, a thin layer (20nm) of gold (Au) was deposited using electron beam evaporation as a seed layer for the subsequent electrodeposition step. In all, 320nm of Au was deposited. Fig. 5.3.1(c) shows the shows the 3D finite-difference-time-domain (FDTD) simulation result of the metal-clad ring laser whose dimensions match the one shown in Fig. 5.3.1 (b). It is clearly shown that the device operates in the whispering gallery mode. The mode volume of the device was

calculated to be 0.7 μm$^3$, which corresponds to 0.32 λ$^3$ where λ is the lasing wavelength in free-space.



(a)



(b)

Fig. 5.3.1 (a): InGaAsP/InP epiwafer used to fabricate the metal-covered ring laser (b): SEM image showing a 4μm diameter ring laser after etching, before metal coverage. (c): field profile inside the device simulated via 3D-FDTD.
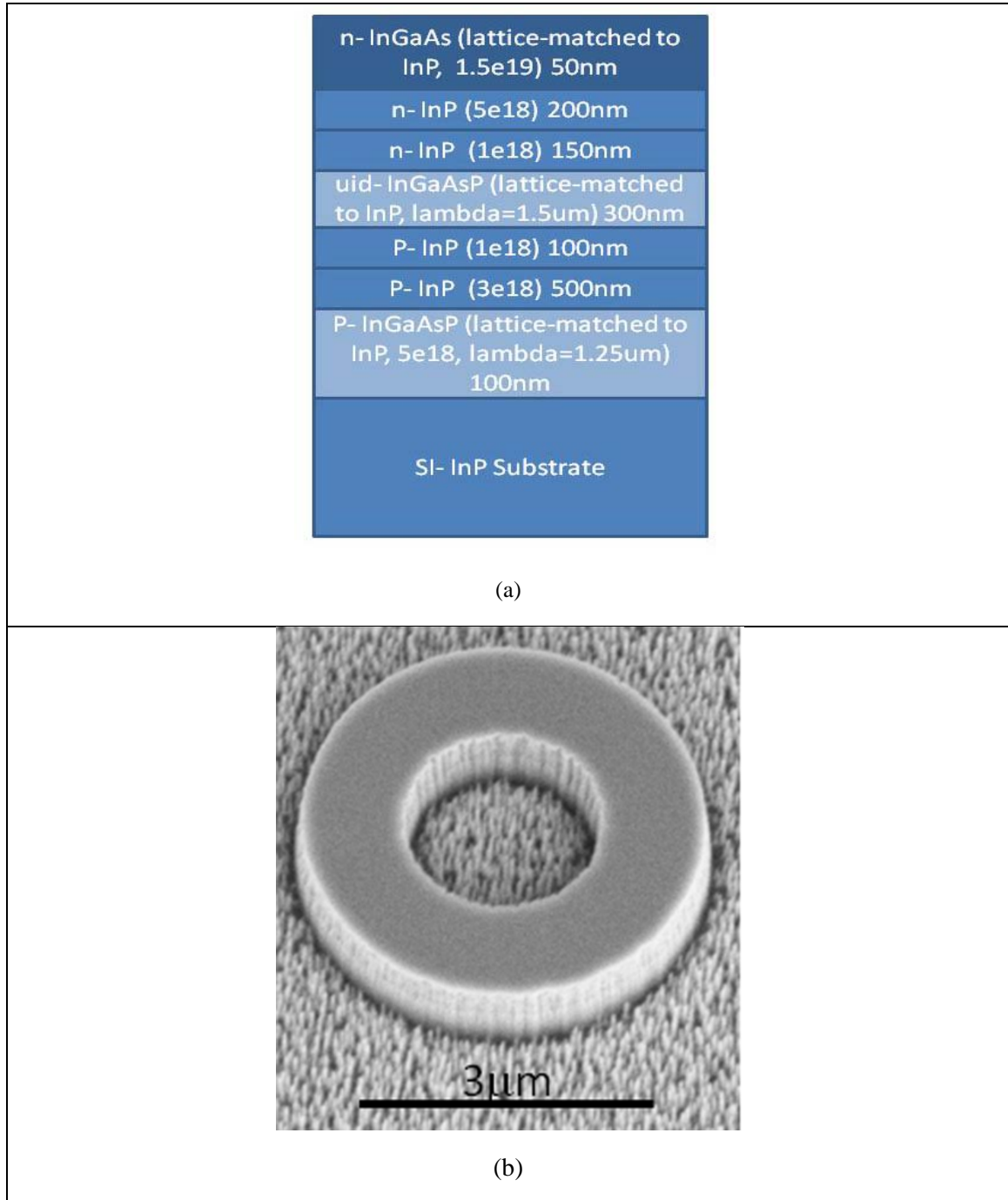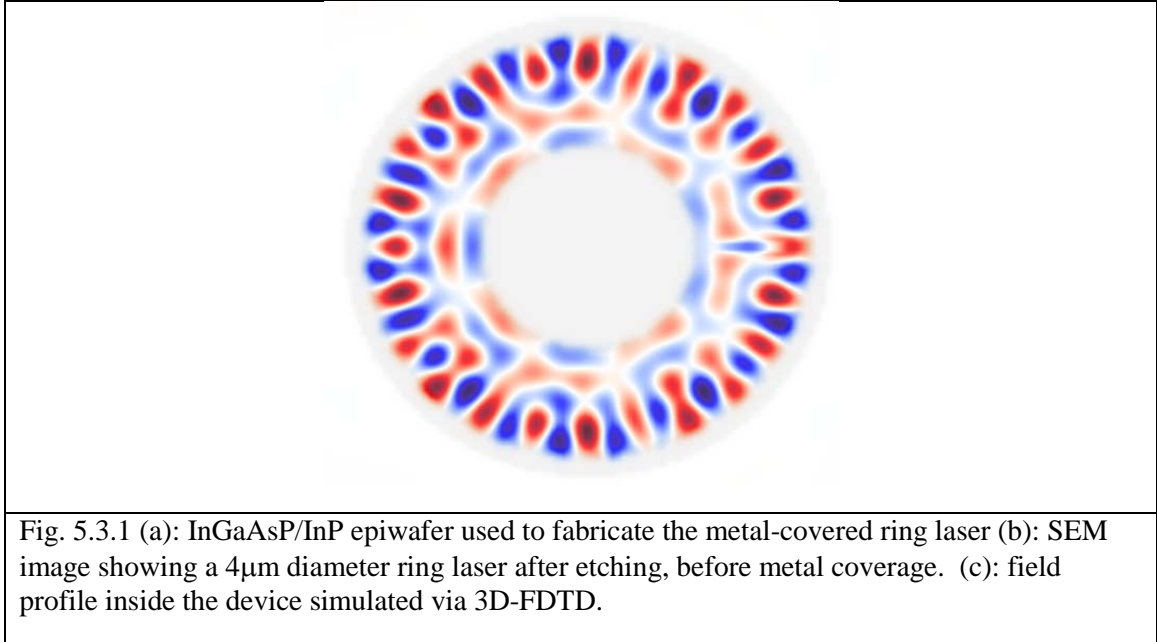
Intensity-dependent micro-photoluminescence (μ-PL) was measured at 77 K for both metal-covered and pure dielectric ring resonator cavities of the same diameter (4 μm) and ring width (1 μm). They were optically pumped through the InP substrate using a 1064-nm wavelength continuous-wave pump laser. In order to align the pump laser with the devices, the gold outside of the device region was etched away using optical lithography for the metal-covered ring resonators. In addition, for pumping through the substrate, the InP substrates was polished. A 20X long-working-distance objective lens was used for focusing the pump laser onto the laser devices. The same objective lens was used to collect the photoluminescence from the optical ring resonator cavities. The front side of the sample was illuminated using a white light lamp. The white light was collimated and focused onto the sample using a 10X long-working-distance objective lens. Alignment of the optical cavity with the pump laser was ascertained from the front side. The μ-PL system is schematically shown in Fig. 5.3.2.

Fig. 5.3.2. Microphotoluminescence measurement system used for optically-pumped lasing in metal-clad micro/nanoring cavities.
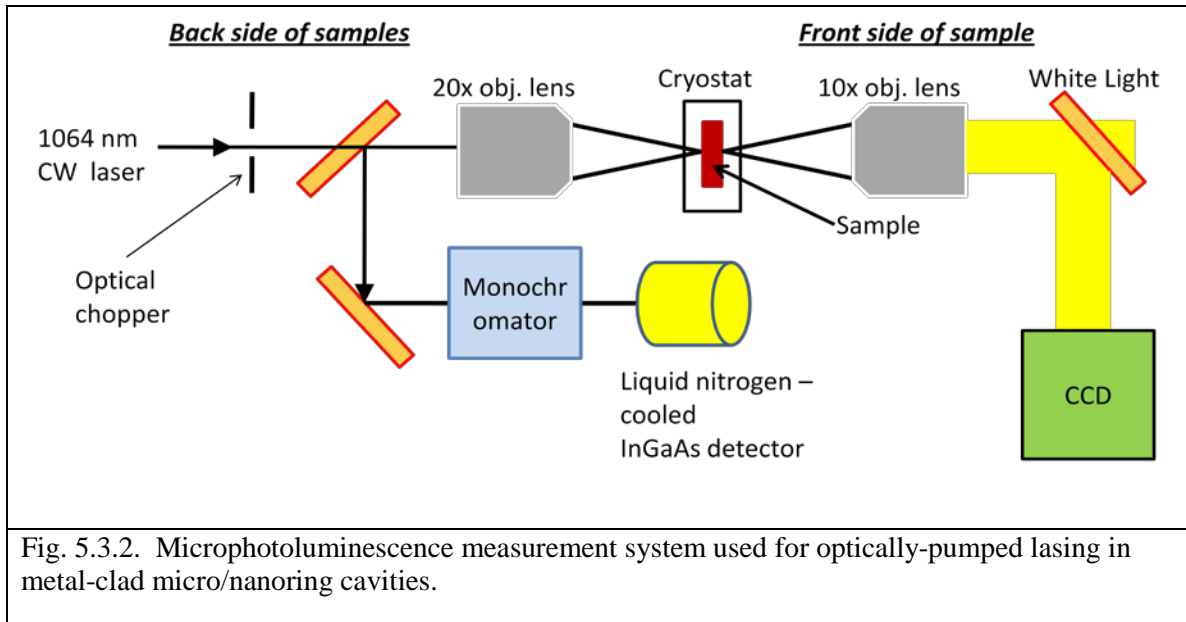
Fig. 5.3.3 (a) shows the intensity-dependent μ-PL of the metal-clad microring resonator. The transition from spontaneous emission to a single-peak stimulated emission can be clearly seen at 21.5 mW pump power which corresponds to a 1.2-mW of power absorbed by the active region assuming a 6-μm diameter of laser focusing spot. The actual absorption should be even lower due to substrate roughness and reflection from cryostat window. On the contrary, Fig. 5.3.3 (b) shows the intensity-dependent μ-PL of the 4-μm diameter pure dielectric ring resonator. Although there is a shoulder developing near the region in which there was a single lasing peak for the device with Au coverage; however, it never fully develops into a stimulated emission peak. Compared to the 11 mW graph, which only shows the spontaneous emission from the epiwafer, the larger pump power graphs exhibit another broad peak between 1360 nm and 1380 nm. We attribute this difference to the fact that higher confinement factor for the device with Au coverage decreases the leakage of field as it travels around the ring, which increases both the cavity-Q factor and modal gain.

63

Fig. 5.3.3. Intensity-dependent microphotoluminescence of a 4-µm microring resonator, (a) covered with Au and (b) not covered with Au, measured at T = 77K. The power shown in the legend is the output power from the pump laser. Only a small fraction (< 1%) of the power indicated in the legend is absorbed by the device.
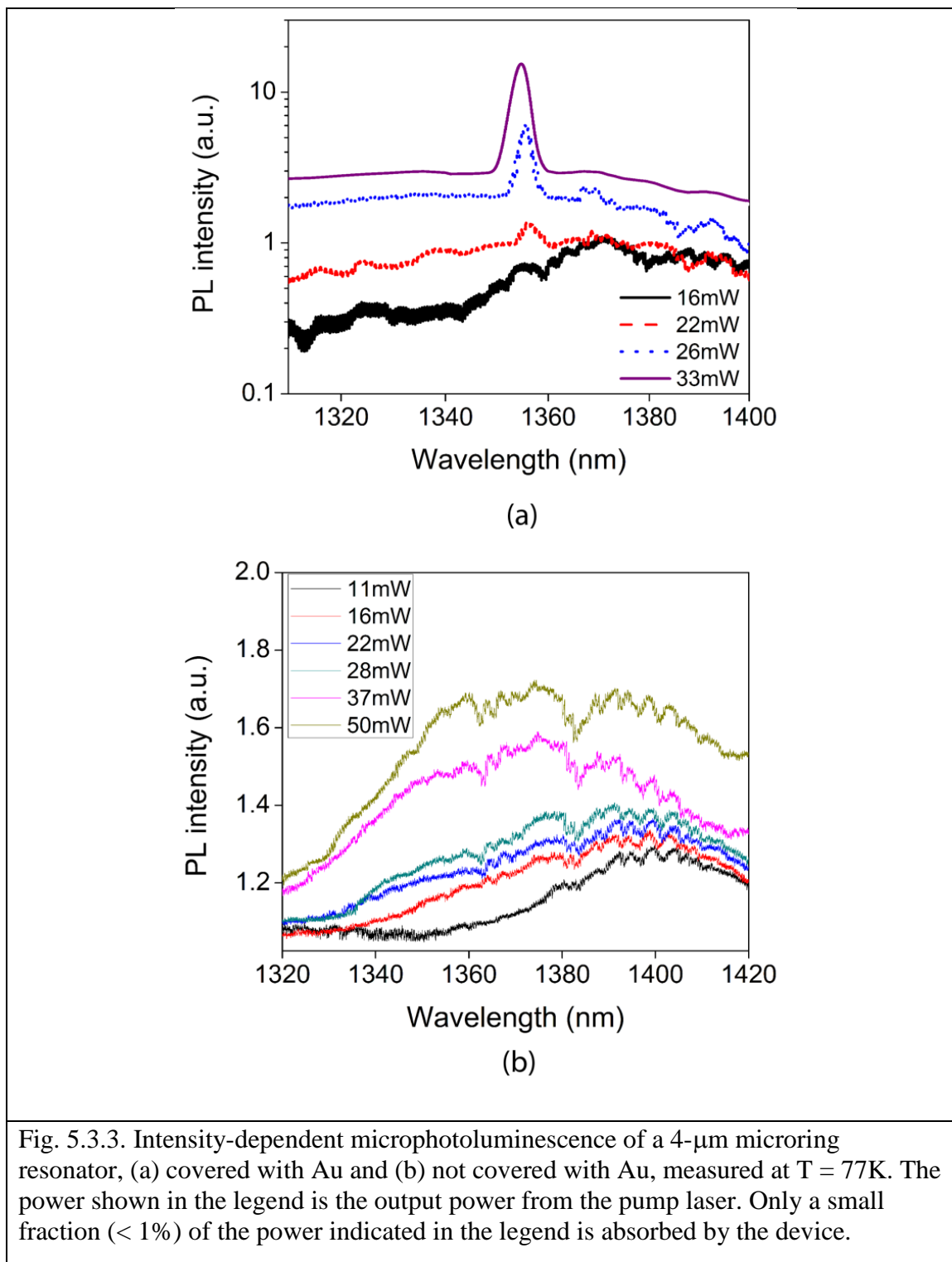
Fig. 5.3.4 (a) shows the L-L curve of the peak μ-PL intensity. The ring resonator that is covered with Au (in black) shows the transition from spontaneous emission to stimulated emission at the threshold. On the other hand, the device that is not covered with Au (in red) shows no such transition. Fig. 5.3.4 (b) shows the FWHM linewidth and the peak wavelength of the stimulated emission for the metal-clad microring laser. The linewidth collapses at the laser threshold from 8 nm down to 1.77 nm. Additionally, the emission peak wavelength, at first, increases due to sample heating as the pump intensity becomes larger. However, when it reaches lasing, the peak starts to blue shift due to frequency pulling effect [72].
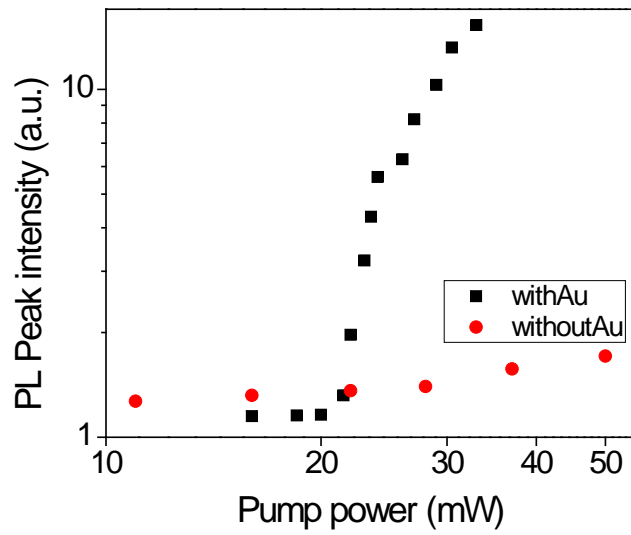
(a)
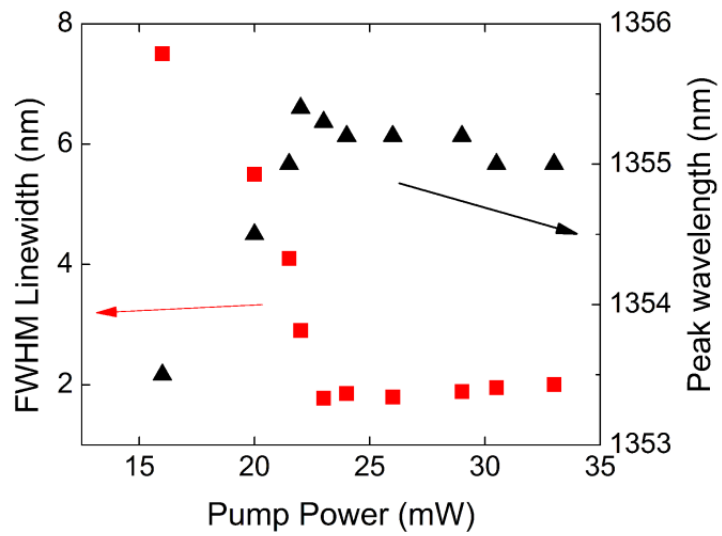


(b)

Fig. 5.3.4 (a) Comparison of peak intensity vs. pump power for 4-μm ring laser devices covered with Au and not covered with Au. (b): FWHM and peak wavelength of the lasing peak of a 4-μm microring laser device covered with Au at various pump powers.

Fig. 5.3.5. Fitting of Peak PL intensity vs. pump power using the laser rate equations with the Purcell factor taken into account.
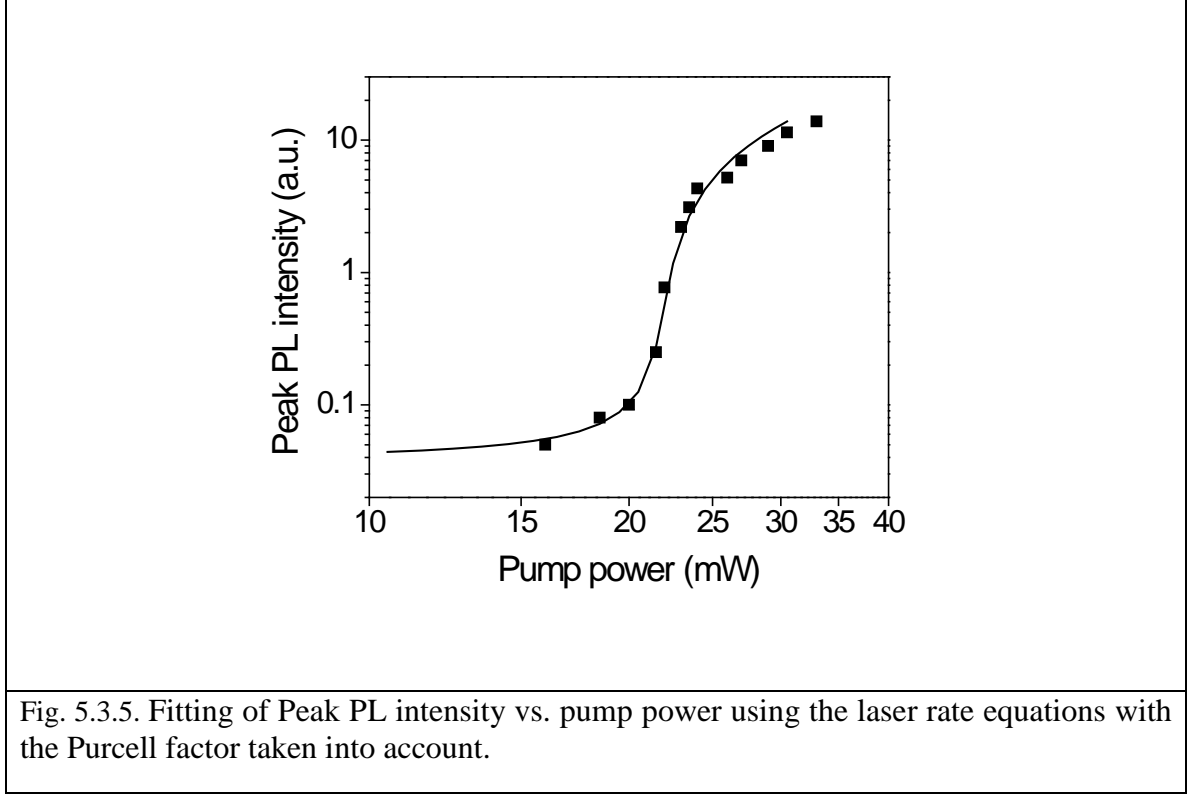
We also fitted the spontaneous emission factor β of the metal-clad microring laser using the following rate equations [36]:

$$\frac{dN}{dt} = P - gS - \frac{1-\beta}{\tau_{sp}}N - \frac{F\beta}{\tau_{sp}}N - \frac{v_s S_a}{V_a}N$$

$$\frac{dS}{dt} = \Gamma gS - \frac{S}{\tau_{ph}} + \frac{\Gamma F\beta}{\tau_{sp}}N$$

where $N,$ $S$ are carrier and photon densities, $P$ is the pumping rate, $g$ is the optical gain, $\tau_{sp}$ is the spontaneous emission lifetime ($\tau_{sp} = 1.5$ ns), $F$ is the Purcell factor, $S_a$ and $V_a$ are exposed surface area and volume of gain region ($S_a = 2\pi r_{out}h + 2\pi r_{in}h$, $V_a = \pi r_{out}^2 h - \pi r_{in}^2 h$), respectively, $v_s$ is surface recombination velocity ($v_s = 2 \times 10^4$ cm/s), $\Gamma$ is

confinement factor ($\Gamma = 0.65$), and $\tau_{ph}$ is the photon lifetime ($\tau_{ph} = Q/2\pi f$, where $f$ is the resonant frequency). $g$ was assumed to follow a linear model with $g = cG(N-N_o)/n_g = 1.09\text{x}10^{-5}(\text{N}-4\text{x}10^{17})$ s$^{-1}$, where $N_o$, $c$, $n_g$ and $G$ are the transparent carrier density, light velocity in vacuum, the group refractive index of the cavity and the linear differential gain coefficient, respectively. The Purcell factor was calculated to be 1.32 with a Q factor of 160, determined experimentally from far below the lasing threshold, and the calculated mode volume. The theoretical Q factor value from a 3D- FDTD simulation yielded 331. Although it is expected that Q factor should be even higher at lower temperatures due to decreased phonon scattering, the actual lower Q factor could be attributed to rough and angled sidewalls. For simulation purposes, $n$ and $k$ values of Au from Ref. [**Error! Reference source not found.**] were used. The $\beta$ factor was found to be $5\text{x}10^{-4}$. Fig. 5.3.5 shows the result of the fitting with the above parameters. Although it is expected that the $\beta$ factor of a resonant cavity device of this dimension should be much larger, it is small due to the presence of metal and the lack of an insulator layer to separate the semiconductor from metal. That is to say that much of spontaneous emission is lost via metal absorption. As the dimensions become even smaller and an insulator is added, the $\beta$ factor is expected to improve and is so demonstrated in the following chapters.

## 5.4 Summary

In this chapter, we explored the possibility of using metal cladding on semiconductor ring lasers (SRLs) in order to further shrink the ring diameters that have been difficult to achieve due to increased diffraction loss. Theoretically we saw that the

addition of metal cladding forms a hybrid dielectric-plasmonic mode which helps confine electric field inside the semiconductor more tightly. This brings about better scaling capabilities. Furthermore, we saw that the metal-clad nanoring lasers have two design parameters which enables independent control of cavity quality factor and resonance wavelength. Lastly, out-coupling capabilities of metal-clad nanoring lasers were investigated in comparison to metal-clad nanopillar lasers and have been found to be superior.

Then, we demonstrated the advantage of metal-cladding in an experiment that directly compared metal-clad and no-metal 4-μm-diameter ring resonators. The metal-clad ring resonator showed a transition from spontaneous to stimulated emission at a threshold pump power that corresponded to 1.2 mW absorbed by the active region, However, there was no such transition for a ring resonator without metal coverage even at much higher pump powers, thereby making shrinking SLR diameters with an aid of metal cladding promising. The $\beta$ factor of the device was found to be $5 \times 10^{-4}$. Although it is expected that the $\beta$ factor of a resonant cavity device of this dimension should be larger, the presence of metal and the lack of an insulator layer to separate the semiconductor from metal causes much of spontaneous emission to be lost via metal absorption. $\beta$ factor is expected to improve with decreasing dimension and addition of insulator and is so demonstrated in the following chapters.

# CHAPTER 6

# Lasing in an Optically-Pumped Sub-wavelength Metal-clad Nanoring Laser

In the previous chapter, we demonstrated that metal cladding is a valid method to continue scaling ring lasers dimensions. In this chapter, we explore methods to fabricate and measure lasing from a ring laser of sub-wavelength diameter.

## 6.1 Fabrication of Sub-wavelength Scale Ring Lasers

As the ring diameter decreased, some of the fabrication steps had to be modified. The following section describes the necessary changes.

### Lift off

In the fabrication of micrometer-scale rings, the bi-layer PMMA lift off process as described in the previous chapter worked well with a negative slope provided by the different molecular weight of the two PMMA layers. However, as the dimension becomes smaller, lifting off the center hole of a ring became increasingly problematic, as

shown in Fig. 6.1.1. The slope of the PMMA on the inner side of the ring became less sloped and, therefore, prevented proper lift-off. This problem was addressed by using a negative e-beam resist (HSQ), Dow-Corning XR-1541. HSQ was spin-coated at 3000 rpm for 50 seconds and baked at $180^{\circ}C$ for 2 minutes on a hot plate. Area dose of 700 $\mu C/cm^2$ with 20 kV acceleration voltage and 10 $\mu m$ aperture was used in Raith 150. The pattern was developed in AZ 400K:DI $H_2O$ (1:4) for 40 seconds.
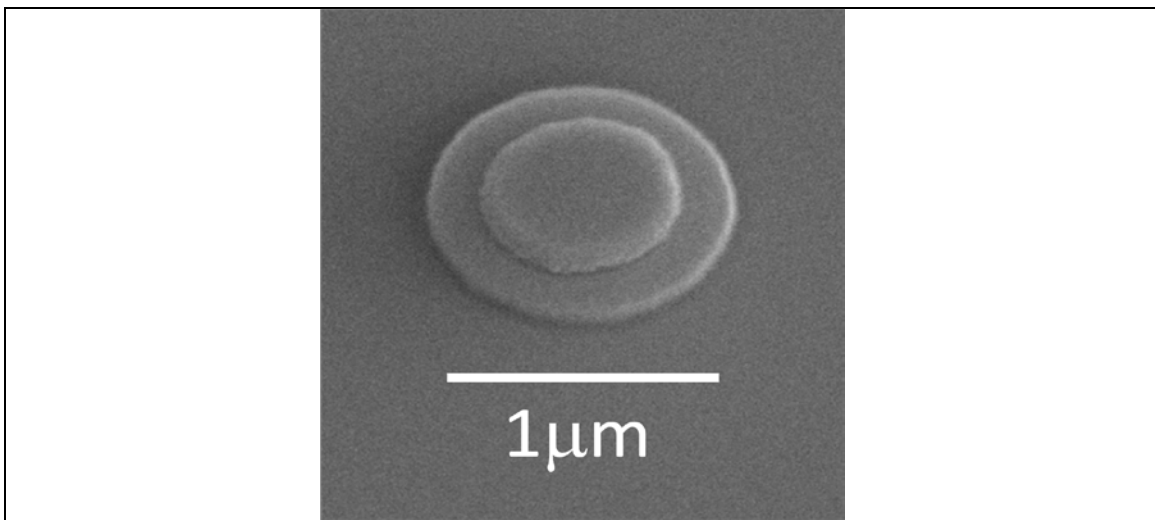


Fig. 6.1.1. SEM showing a lift-off problem in a sub-wavelength scale ring device

**Mask Erosion**

After replacing the bi-layer PMMA process with the XR-1541 HSQ process, there occurred severe mask erosion during the subsequent InGaAsP/InP etch step involving a $CH_4/H_2/Ar$ environment, as shown in Fig. 6.1.2. To alleviate the problem, 200 nm of silicon nitride and 50 nm of chromium (Cr) were deposited before the negative resist electron beam lithography process. HSQ was used as the etch mask for Cr, and Cr was used as the etch mask for silicon nitride. In turn, silicon nitride/Cr were used as the etch mask for InGaAsP/InP. Silicon nitride was used as a sacrificial layer in order to remove

71

Cr after the InGaAsP/InP etch.  Using a hard mask gave a much straighter etch profile, as shown in Fig. 6.1.3.  In the figure, it can be seen that polymer is formed during InGaAsP/InP etch on the device.  It is well known that polymer is formed on surfaces as a by-product of RIE in methane-based plasmas [66].



Fig. 6.1.2.  SEM images showing a mask problem.  The image on the right was obtained after cutting a cross section using focused ion beam (FIB)



Fig. 6.1.3. SEM after switching to a hard mask, silicon nitride/Cr

**Insulation of metal**

As the device dimension gets smaller, metal absorption loss becomes increasingly severe. Fig. 6.1.4 shows how Au coverage affects photoluminescence. Two identical devices were measured under the same condition. The only difference was that the device indicated by the red line was covered with Au, deposited by electron-beam evaporation and electrodeposition, whereas the device indicated by the black line was not covered with Au. Both devices were fabricated in the way manner described above. The substrates of both devices were polished. They were pumped through the substrate using a 1064nm laser. The pump laser was focused using a long working distance 20X objective lens. The samples were kept at 77K. As the devices get smaller, electric field is located closer to the metal, which quenches spontaneous emission. Therefore, an insulator must be deposited between the InGaAsP/InP wafer and Au.



Fig. 6.1.4. Photoluminescence of a 2μm-diameter ring with (red) and without (black) Au.
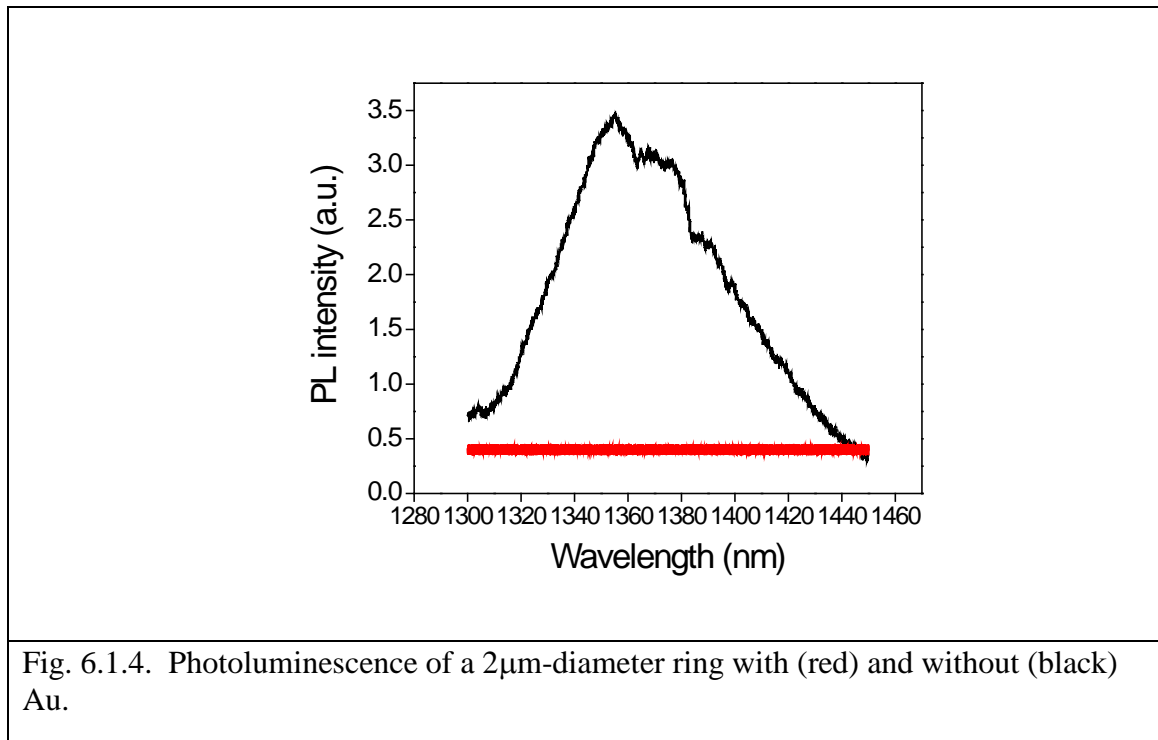
## 6.2 Lasing in a Sub-wavelength Metal-clad Nanoring Laser

The sample preparation is described in the following. The InGaAsP/InP epiwafer was grown by the metal-organic chemical vapor deposition (MOCVD) technique. All layers are lattice-matched to InP, and the index contrast provides the necessary vertical confinement. To define the ring, 200 nm of silicon nitride and 50 nm of Cr were deposited as a hard mask via e-beam evaporation and electron beam lithography with a negative resist (Hydrogen Silsesquioxane, HSQ) was used for patterning. HSQ was spin-coated at 3000 rpm for 50 seconds and baked at $180^{o}$C for 2 minutes on a hot plate. Area dose of 700 μC/cm$^2$ with 20 kV acceleration voltage and 10 μm aperture was used in Raith 150. The patt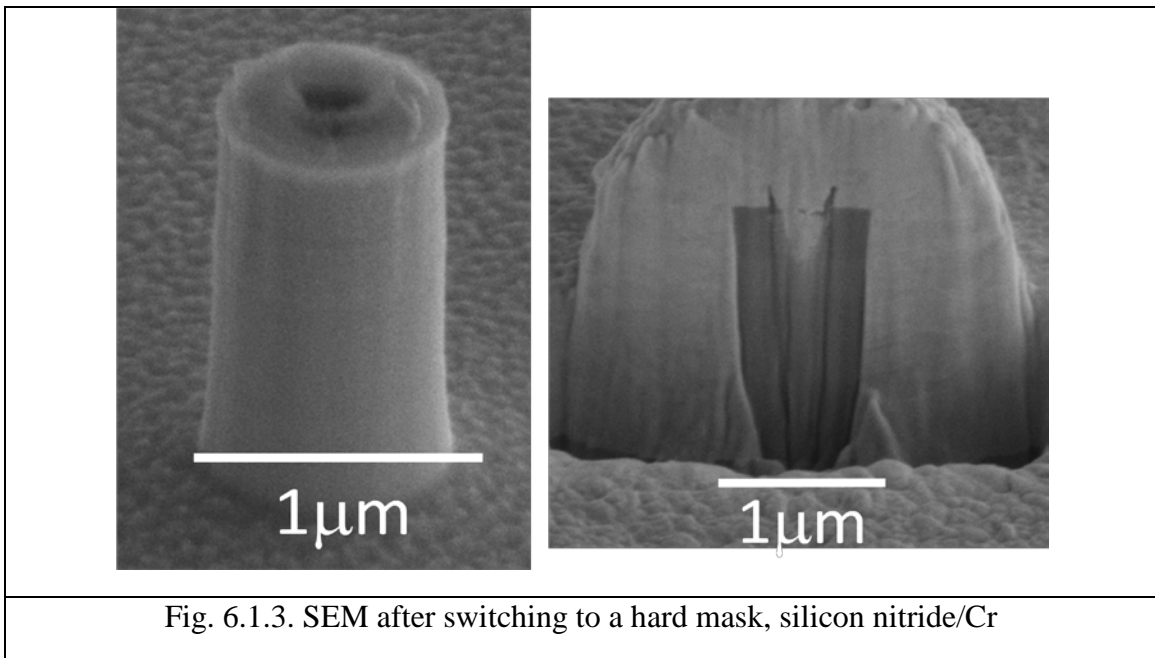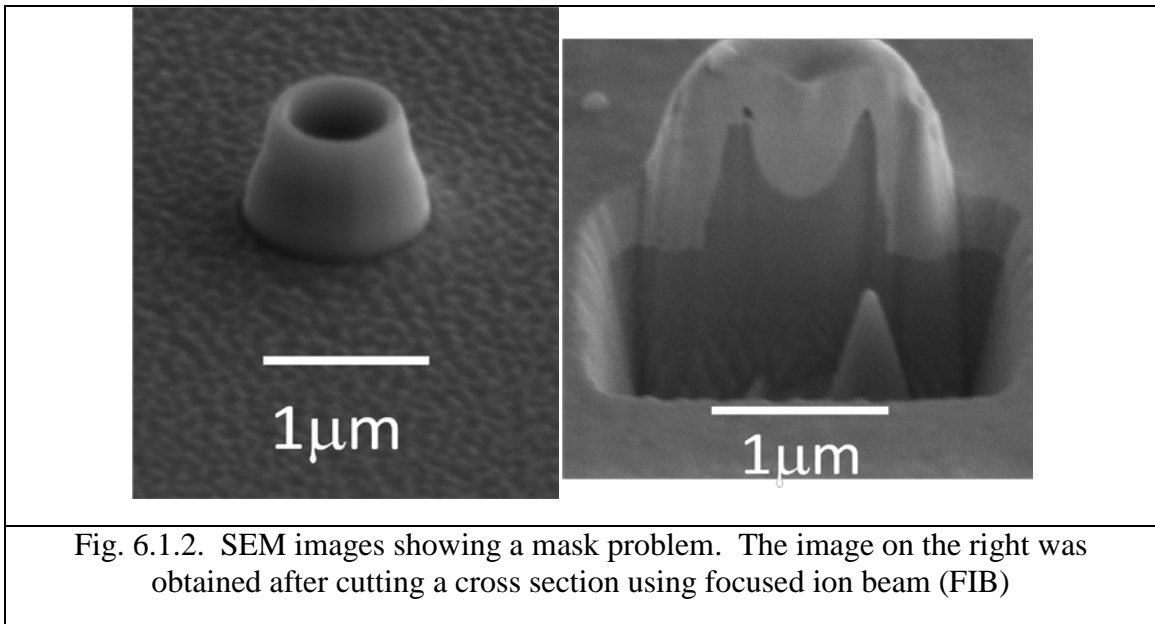ern was developed in AZ 400K:DI H$_2$O (1:4) for 40 seconds. Subsequently, the InGaAsP/InP epiwafer was dry etched in a CH$_4$/H$_2$/Ar environment (4 sccm/28 sccm/14 sccm) environment using PlasmaTherm 790. The pressure and power were maintained at 30 mTorr and 200 W, respectively. During the InP etching, polymer was deposited as a byproduct and was removed using an O$_2$ ashing cycle (70 sccm, 200 mTorr, 100 W, 3 minutes). Once the semiconductor rings were formed, 10 nm of Al$_2$O$_3$ was deposited via ALD as an insulator to separate the semiconductor from subsequent metal coverage. For conformal metal coverage, a combination of sputtering and electrodeposition was used. A thin layer (20 nm) of gold (Au) was first sputtered as a conductive layer. Then, electrodeposition was followed for 300 nm. 1.2-μm-diameter sub-wavelength nanoring microcavity has been fabricated as shown in Fig. 6.2.1. The cross sectional view was obtained via focused ion beam (FIB). Due to the etching chemistry and limitation on small feature size, etch depth of the center hole is only about

1/3 that of outer diameter. According to a 3D-FDTD simulation, Q factor of a 800-nm-diameter ring with 200 nm ring width changes from 7750 to 7130 with such change in the center hole etch depth. This means that nanoring lasers do not have to have the center hole etched through the active region and filled with metal. Just as electric field in a ridge waveguide is laterally confined via refractive index contrast due to a semiconductor ridge on top, a similar ridge of the ring shape on the top of the nanoring provides the necessary index contrast for lateral confinement in the nanoring laser without sacrificing the quality factor. Fig. 6.2.2 shows that, as in the case of a full depth center hole filled with metal, the cavity in the ridge nanoring laser is formed by total internal reflection, known as whispering gallery mode (WGM).



Fig. 6.2.1. SEM image of a 1.2-μm nanoring laser, with metal coverage. Cross sectional view was obtained via FIB.

Fig. 6.2.2. 3D-FDTD simulation of a metal-clad nanoring laser with an incomplete center hole etch depth. The center hole is etched down to, but exclusive of, the active region.
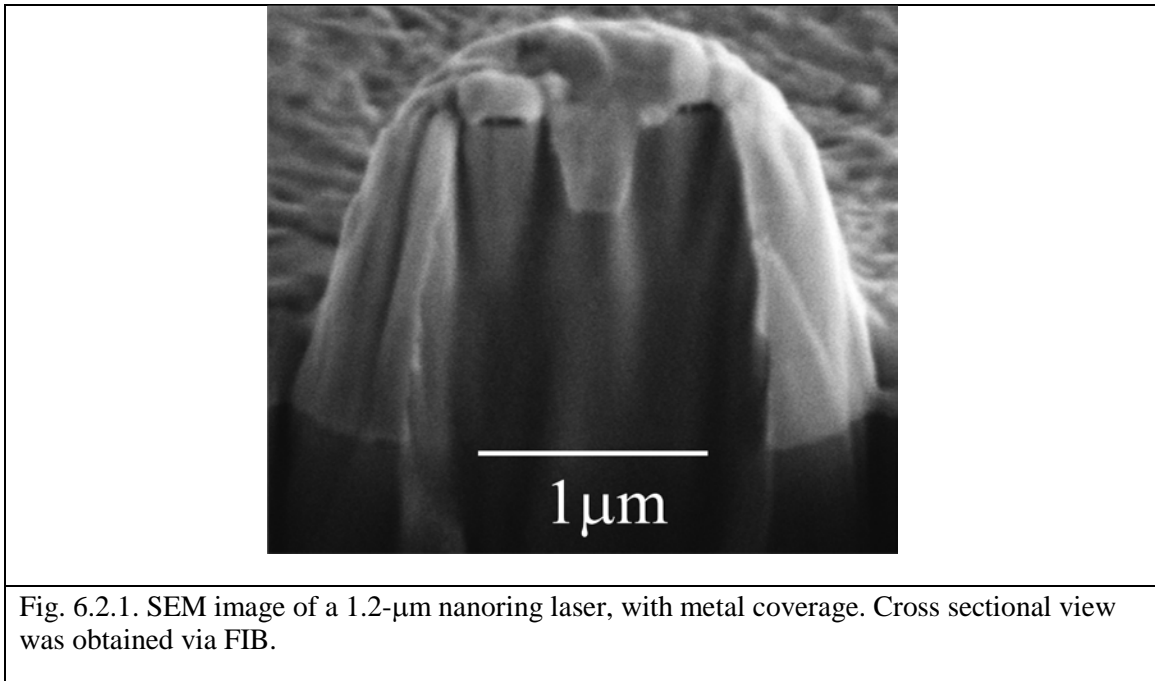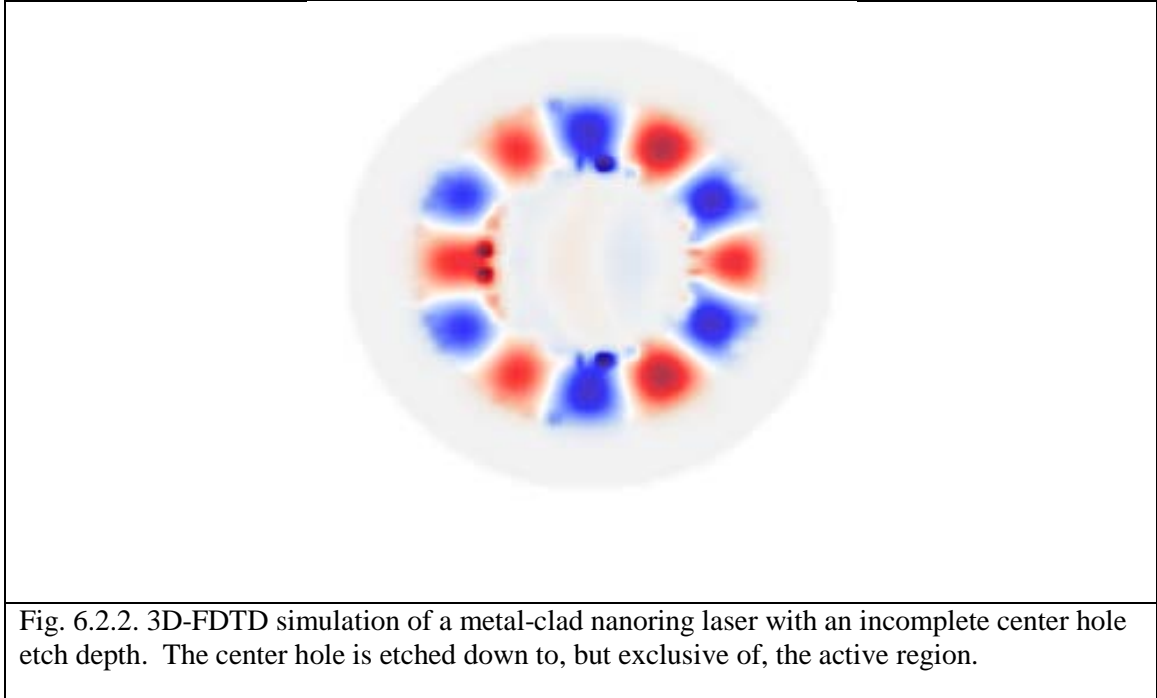
Micro-photoluminescence measurement was carried out to demonstrate lasing in the 1.2-μm metal-clad nanoring cavity. The same measurement scheme as used for the 4-μm metal-clad nanoring resonator cavity was used. As a reminder, a schematic is given in Fig. 5.3.2. The cryostat was cooled down and kept at 10 K using liquid helium. Liquid helium temperatures were used in order to minimize non-radiative recombination. Results of the measurement are shown in Fig. 6.2.3. Transition from spontaneous emission to stimulated emission as well as progression of a lasing peak is clearly seen in the figure. Along with the stimulated emission, spontaneous emission also becomes broader. Also, the peak of spontaneous emission seems to blue shift possibly due to band filling. The PL data are analyzed further, and the pump power vs. peak PL intensity is plotted in Fig. 6.2.4. Transition from spontaneous to stimulated emission is at the pump power of 10 mW (actual power absorbed = 50 μW). Compared to a 4 μm microring laser, which had the transition at the pump power of 21.5 mW (actual power absorbed = 1.2

mW), the smaller metal-clad nanoring cavity has a much smaller threshold to lasing. This is expected as the smaller mode volume of the 1.2 μm nanoring cavity is expected to lower the threshold pump power. The mode volume of the metal-clad nanoring resonator cavity of 1.2 μm diameter is 0.004 $\mu m^3$. The L-L curve in Fig. 6.2.4 was fitted with the laser rate equations as was done for the 4-μm-diameter microring resonator. The 1.2-μm nanoring laser has a spontaneous emission coupling factor, $\beta$, of 0.01 while the 4-μm-diameter microring laser had $\beta$ of $5 \times 10^{-4}$. The higher $\beta$ factor also contributes to decreased threshold pump power, as observed in Fig. 6.2.4. Additionally, the 1.2 μm diameter nanoring cavity shows a saturation behavior as the pump power exceeds 40 mW possibly due to sample heating. The focused laser spot was about 10 μm in diameter and any laser power that hit outside the resonator area contributed to sample heating.



Fig. 6.2.3. Pump power-dependent PL intensity versus wavelength for a 1.2-μm diameter metal-clad nanoring resonator cavity
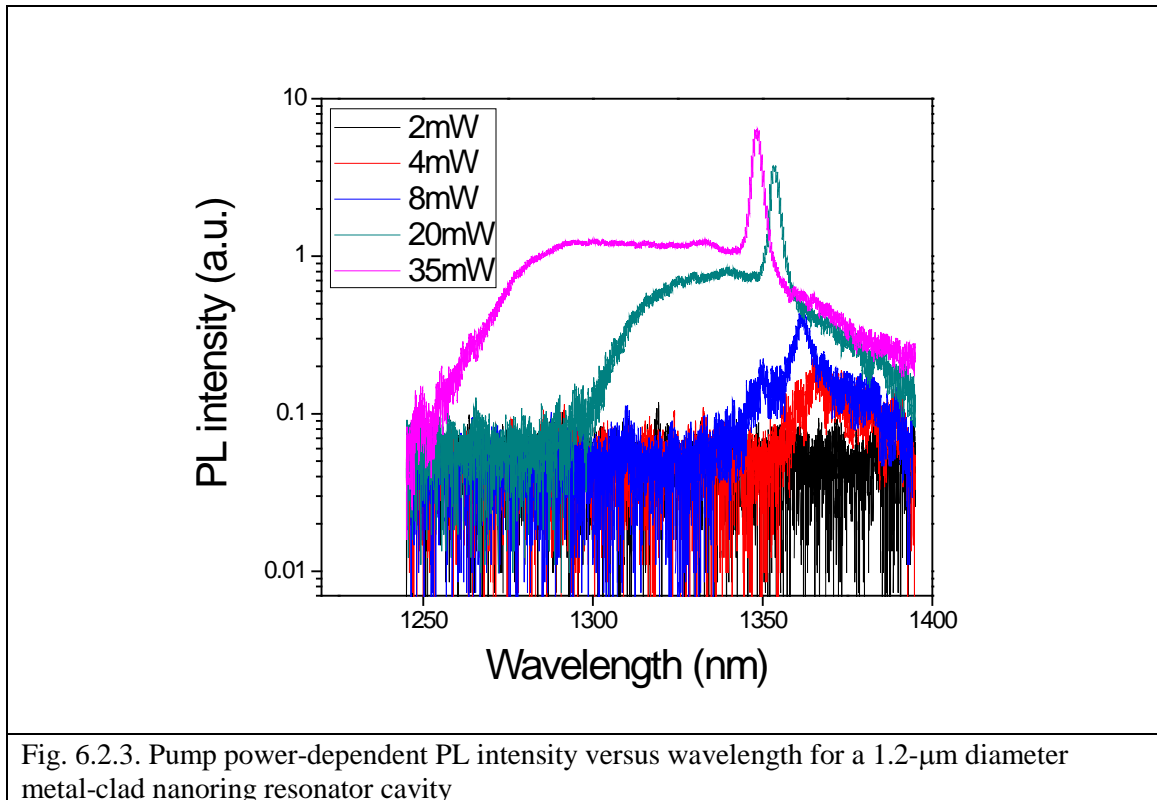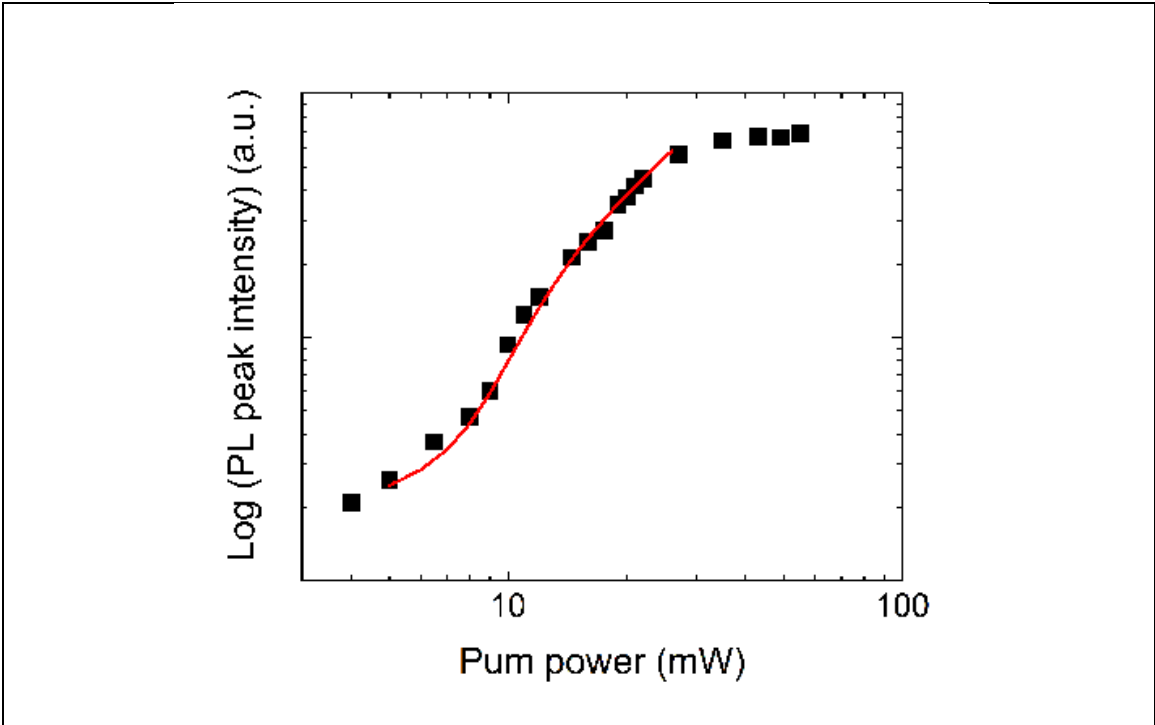
Fig. 6.2.4. Pump power vs. Peak PL intensity of 1.2-μm diameter metal-clad nanoring. Fitting was done using laser rate equations.
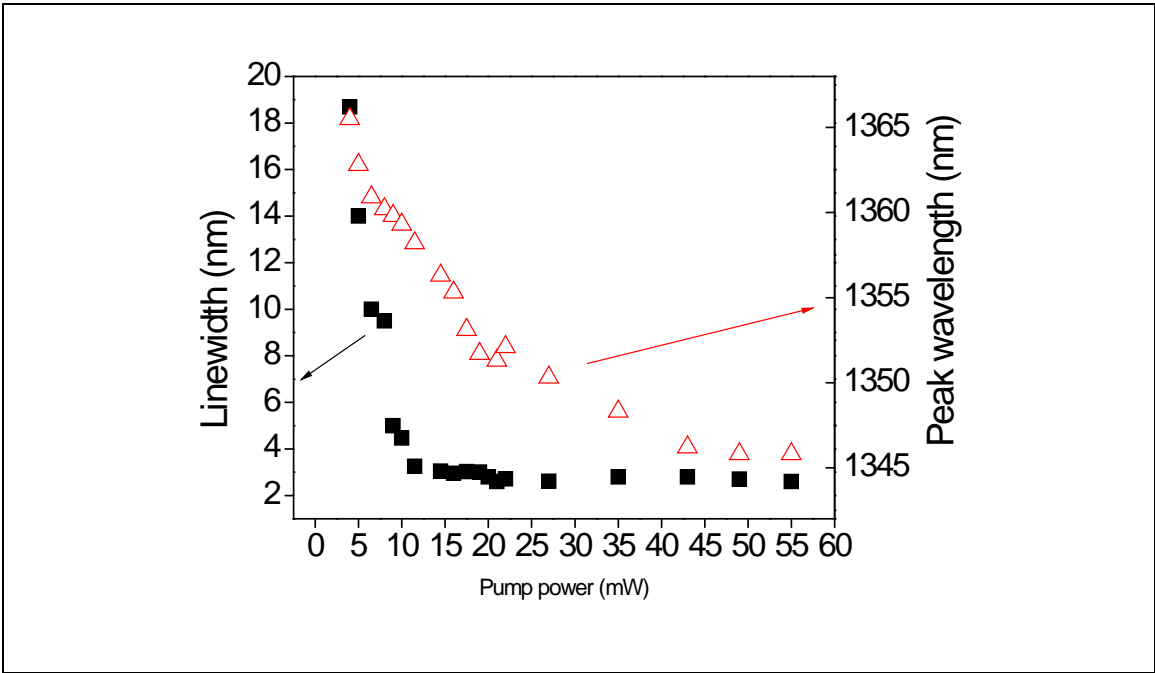


Fig. 6.2.5. Linewidth and peak wavelength vs. pump power of 1.2-μm diameter metal-clad nanoring

Fig. 6.2.5 shows linewidth and peak wavelength vs. pump power of the 1.2-μm diameter metal-clad nanoring resonator cavity. The PL data from Fig. 6.2.3 were fitted with a Lorenzian function to discover the progression of linewidth and peak wavelength with increasing pump power. Linewidth was 19nm far below the threshold, and rapidly collapsed to 2.3 nm at the pump power of 10 mW, corresponding to the threshold as discovered earlier in Fig. 6.2.4. On the other hand, the peak wavelength continuously decreased with increasing pump power. The lasing wavelength continuously decreased with the increasing pump power, possibly due to band filling, although the lasing wavelength seemed to be settling at a high pump power. This is explained by the thermally induced red-shift at the high pump power that compensates the blue shift.

One notable difference between the 1.2-μm and 4-μm diameter metal-clad ring resonator cavities is that initial red shift caused by thermal effect was observed for the 4-μm diameter resonator. The reasons for the difference could be two-fold. Because the active region volume was smaller and the threshold pump power was lower for the 1.2-μm ring resonator, there was less thermal heating by the pump power. At the same time, since a lower temperature was used for the 1.2-μm resonator measurement, thermal dissipation was more efficient.

## 6.3 Controllability of Peak Wavelength via Control of Ring Width

As the demand for interconnect speed and architectural complexity increases, optical interconnect is a potential candidate for future intra- and inter-chip communications, offering a higher bandwidth at lower energy consumption. [74, 75] A dense optical interconnect network requires nanoscale components to be compatible with electronic components. In addition to nanoscale optical modulators, waveguides, and photodetectors, nanoscale ring resonators can provide most of the remaining functions that are needed including both passive signal processing such as add-drop filtering [76], dispersion compensation [77], and signal buffering [78] as well as active light generation and manipulation such as lasers [79, 80] and switches. Furthermore, a ring resonator can be lithographically defined and evanescently coupled to an optical waveguide. Therefore high density integration of ring resonators of different functions is possible.

One problem with typical nanolasers is that, due to nanolasers' innate nature of short cavity length, their free spectral range is usually very large. Therefore, it is difficult to fine-tune lasing wavelengths while scaling the laser dimensions. The nanoring laser has two parameters that control the resonance wavelength, ring diameter and width, which make it easier to control lasing wavelength and dimensions independently. For example, semiconductor nanoring laser's outer diameter can stay constant while controlling the lasing wavelength using ring width. The two parameters can be used together to optimize the cavity Q factor. This results in constant overall laser dimensions with multiple possible lasing wavelengths within a small range, making the semiconductor nanoring lasers attractive for on-chip use for a couple of reasons. Firstly,

constant physical dimensions make the placement of nanoring lasers exhibiting different output wavelengths in an ultradense layout easier. Secondly, the possibility of multiple wavelengths within a small range makes on-chip wavelength-division multiplexing (WDM) possible, enabling a more efficient on-chip optical interconnect network. A schematic describing how wavelength division multiplexing and demultiplexing works is given in Fig. 6.3.1. While it is true that gratings have been a preferred choice for resonance wavelength control for larger laser cavities, it is quite difficult to integrate other wavelength-controlling feedback structures such as gratings into a nanoscale laser cavity because of the size. Therefore, as dimensions become smaller, multiple design parameters give an added advantage of wavelength control.



Fig. 6.3.1. Schematic describing on-chip communication utilizing a wavelength division multiplexer and demultiplexer

Fig. 6.3.2. Lasing wavelength variation with varying ring widths
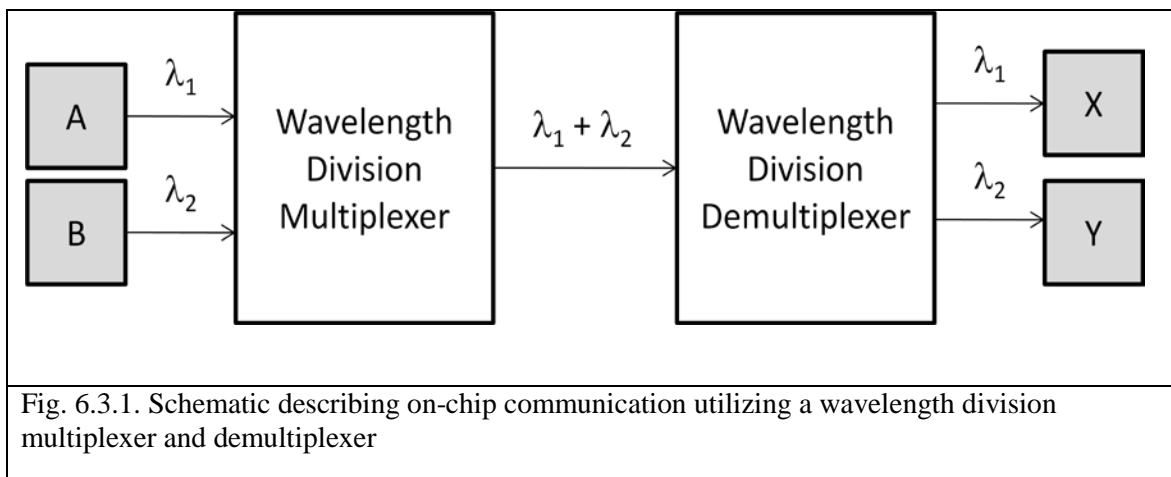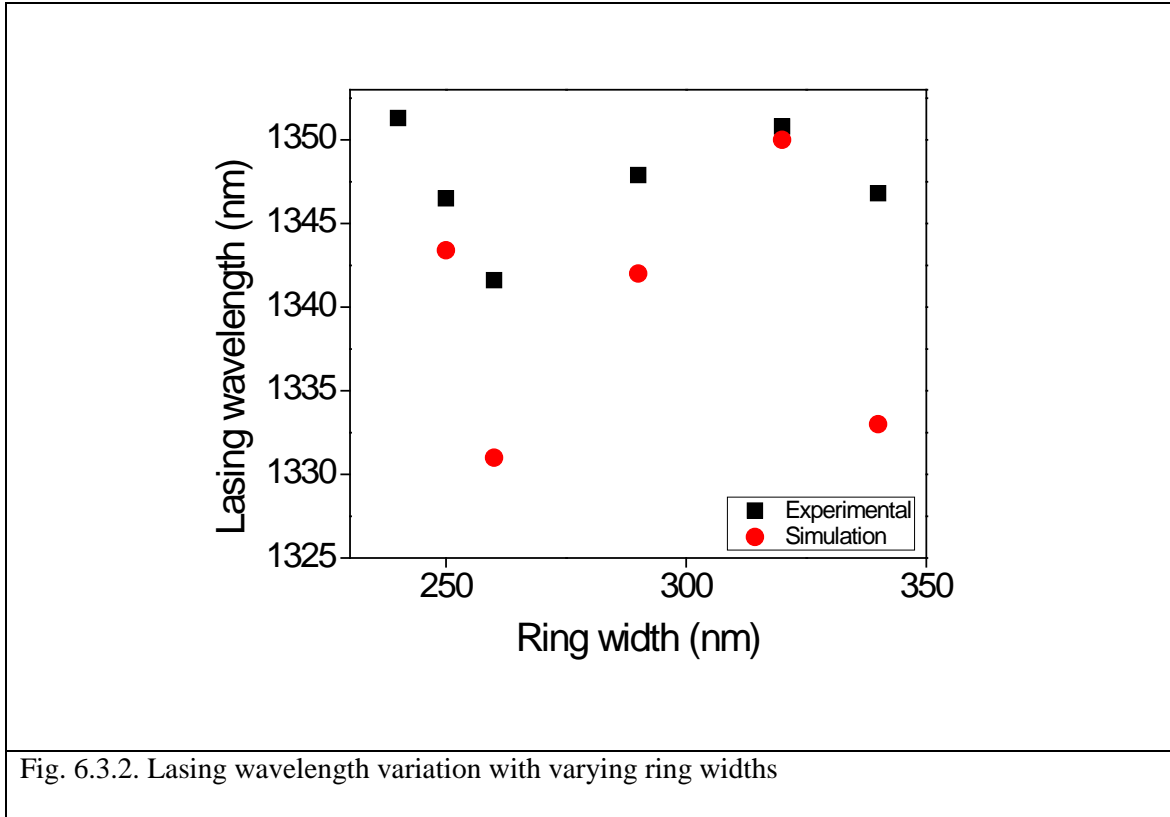
To demonstrate wavelength tuning, metal-clad nanoring lasers of 1.2−μm diameter with various ring widths were fabricated and measured using the identical optical measurement scheme described above. The results are shown in Fig. 6.3.2. It can be clearly seen that, by altering the ring width between 240 nm and 340 nm, the lasing wavelength can be fine-tuned to within a 10 nm range. The oscillatory behavior of the lasing wavelength is due to the shift of nearby resonance peaks in and out of the spontaneous emission range of the epi-structure. According to the 3-dimensional finite-difference-time-domain (3D-FDTD) simulations, the resonance peaks undergo a red-shift behavior with increasing ring width in general. Resonance peaks within the spontaneous emission range of the epi-structure from 3D-FDTD simulations are plotted along with the

experimental data.  The trend agrees well with the experiment. The discrepancy of the lasing wavelengths may be due to the passive active region assumed in the calculations.

## 6.4 Summary

In this chapter, we demonstrated lasing in a sub-wavelength-scale metal-clad nanoring laser.  Compared to fabrication of a 4-µm-diameter ring laser, several changes were made necessary to fabricate a 1.2–µm-diameter ring laser, including a hard mask, negative resist, and addition of an insulator layer.  The 1.2-µm nanoring laser showed a much lowered threshold pump power.  It corresponded to actual absorbed power of 50 µW as opposed to 1.2 mW for the 4-µmring from the previous chapter.  When fitted to laser rate equations, the sub-wavelength nanoring laser had a spontaneous emission coupling factor, $\beta$, of 0.01 while the bigger microring laser had $\beta$ of $5\mathrm{x}10^{-4}$.  The higher $\beta$ factor also contributes to decreased threshold pump power.

Additionally, fine tuning capability of the metal-clad nanoring laser has been investigated.  Because of a large spectral range of a nanolaser, fine-tuning is expected to be difficult without having to sacrifice the overall laser dimensions significantly.  On the other hand, the metal-clad nanoring laser has two design parameters which allow control of resonance wavelength without having to significantly modify the overall laser diameter.   The emission wavelength can be tuned within a 10-nm range by changing the ring width from 240 nm and 340 nm.

# CHAPTER 7

# Electrically-Pumped Metal-clad Nanoring Laser

With optically pumped lasing demonstrated in previous chapter, it is important that a laser be able to be electrically pumped in order to facilitate integration with electronic components. Therefore, a possible scenario of electrical pumping has been investigated, and some possible improvements were addressed.

## 7.1 Fabrication

In order to make the n- and p- contacts, the following has been added to fabrication. 200 nm of $Si_3N_4$ was deposited using e-beam evaporation. Rings were formed using a stepper GCA AS200. For easy lift off, bi-layer of LOR 3A and S1805 was used. First, LOR 3A was spin-coated at 4000 rpm for 45 seconds and baked at 190 degrees for 6 minutes. Then, S1805 was spin-coated at 4000 rpm for 45 seconds and baked at 115 degrees for 2 minutes. The resist was exposed in the stepper for 0.08 seconds and developed in MF 319 for 75 seconds. 50 nm of Ti was deposited and lifted off in Remover PG. Etching of $Si_3N_4$ and InP was done in the same manner as described

in Ch. 6. 20 nm of $Al_2O_3$ and 20 nm of $Si_3N_4$ were deposited using ALD and PECVD, respectively, to prevent shorting of the two contacts. It also prevents the n-contact from biasing the substrate in entirety. P-contact pads were optically defined using S1813 photoresist. $Al_2O_3$ / $Si_3N_4$ were first removed in BHF (2 min). Then, InP was etched in HCl:$H_3PO_4$ (1:1) for 10 seconds. The p+ InGaAsP layer served as an etch stop against the InP etchant. Afterwards, 20 nm each of Ti (titanium) / Pt (platinum) / Au (gold) / Pt were deposited using e-beam evaporation and lifted off in acetone. This formed the p-contact. Then, S1813 photoresist was spin-coated again. It was ashed in $O_2$ (pressure = 200 mTorr, Power = 100 W) for 14 seconds (etch rate: 27 nm/sec) in order to expose only the top of rings. Exposure of the top of rings was verified periodically using an optical microscope. This step is critical because too much etch-back would result in shorting of n- and p-contacts and not enough etch-back would result in a highly resistive n-contact. The $Al_2O_3$ / $Si_3N_4$ insulator layer on the top of the rings was removed in BHF for 2 minutes. The photoresist was stripped away. A fresh layer of S1813 was spin-coated, and an n-contact pad was optically defined. 20 nm each of Ti / Pt / Au were deposited using e-beam evaporation and lifted off in acetone. This formed the n-contact. Next, for conformal deposition of Au, 20 nm of Au was sputtered as a seed layer, and 500 nm of more Au was subsequently electroplated. Another step of optical lithography and etching of Au in between the two contact pads separated the n- and p- contacts using the previously used n- and p- masks. For this, image reversal resist, AZ 5214E, was used. It was spin-coated at 2500 rpm for 30 seconds and baked at 90 degrees for 1 minute. It was then exposed in MA-6 for 2.5 seconds and again hard baked at 115 degrees for 1 minute. Afterwards, a flood exposure was done for 40 seconds and the resist was developed in

MF 319 for 40 seconds. The gold outside of the contact areas were removed in TFA Gold Etchant. The contacts were annealed at 400 C for 1 minute. Fig. 7.1.1 shows a schematic of an electrically pumped metal-clad nanoring laser.



Fig. 7.1.1. Schematic of metal-clad nanoring laser for electrical pumping
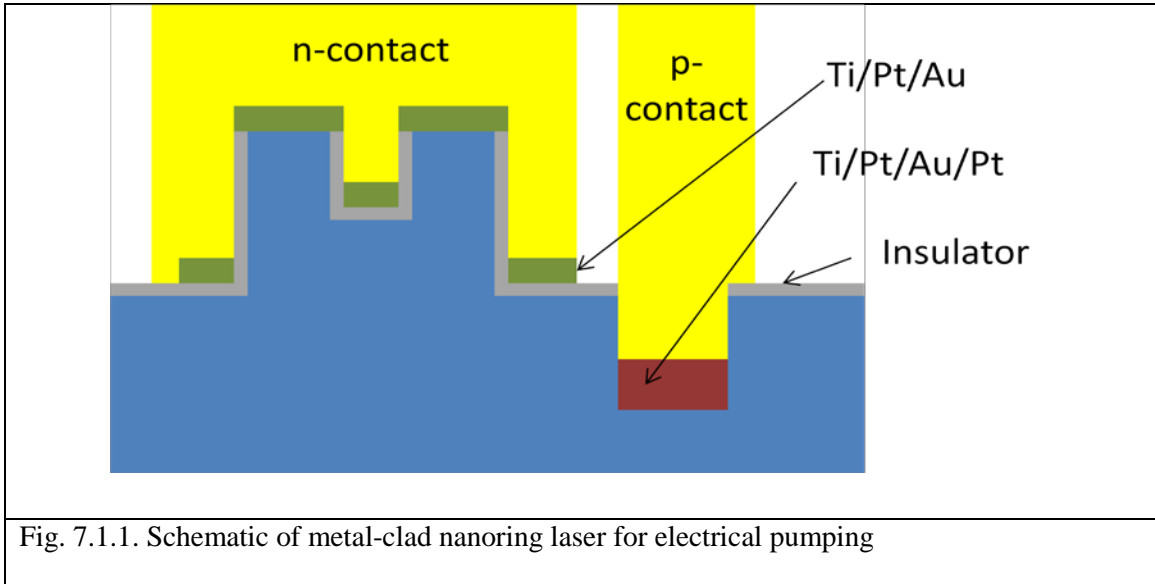
## 7.2 Current-Voltage (I-V) Measurement

I-V curve of the electrical device was measured and is shown in Fig. 7.2.1. The graph compares the two materials as the insulator. One was 20 nm of $Al_2O_3$ alone and the other was 20 nm of $Al_2O_3$ + 20 nm of $Si_3N_4$. As can be seen from the figure, the n-p diode using $Al_2O_3$ alone is very leaky. It is attributed to two possible causes. Firstly, due to the insulator being only 20 nm, it is possible that the contact metals could have shorted through the insulator during the annealing step, causing a very leaky diode. Secondly, it has been found that $Al_2O_3$ cannot serve as an ideal insulator material for p-InP due to its band structure, which is shown in Fig. 7.2.2. $Al_2O_3$ provides only about $0.1 - 0.2$ eV of barrier on the conduction band side, making it a very leaky insulator. On the other hand,

Si$_3$N$_4$ provides a good barrier on both the conduction and valence bands, as also shown in Fig. 7.2.2. Therefore, it is a much better insulator to be used for p-InP. The I-V curve using both Al$_2$O$_3$ and Si$_3$N$_4$ shows a good rectification behavior. However, the resistance is still rather large ($\sim$2 k$\Omega$) and needs to be improved.



Fig. 7.2.1. I-V curve of n-p junction of metal-clad nanoring laser. Compares two insulator materials (Al$_2$O$_3$ vs. Al$_2$O$_3$ + Si$_3$N$_4$)

Fig. 7.2.2.  Comparison of Al$_2$O$_3$ and Si$_3$N$_4$ as an insulator for p-type InP.  Al$_2$O$_3$ does not provide a good barrier for conduction band.
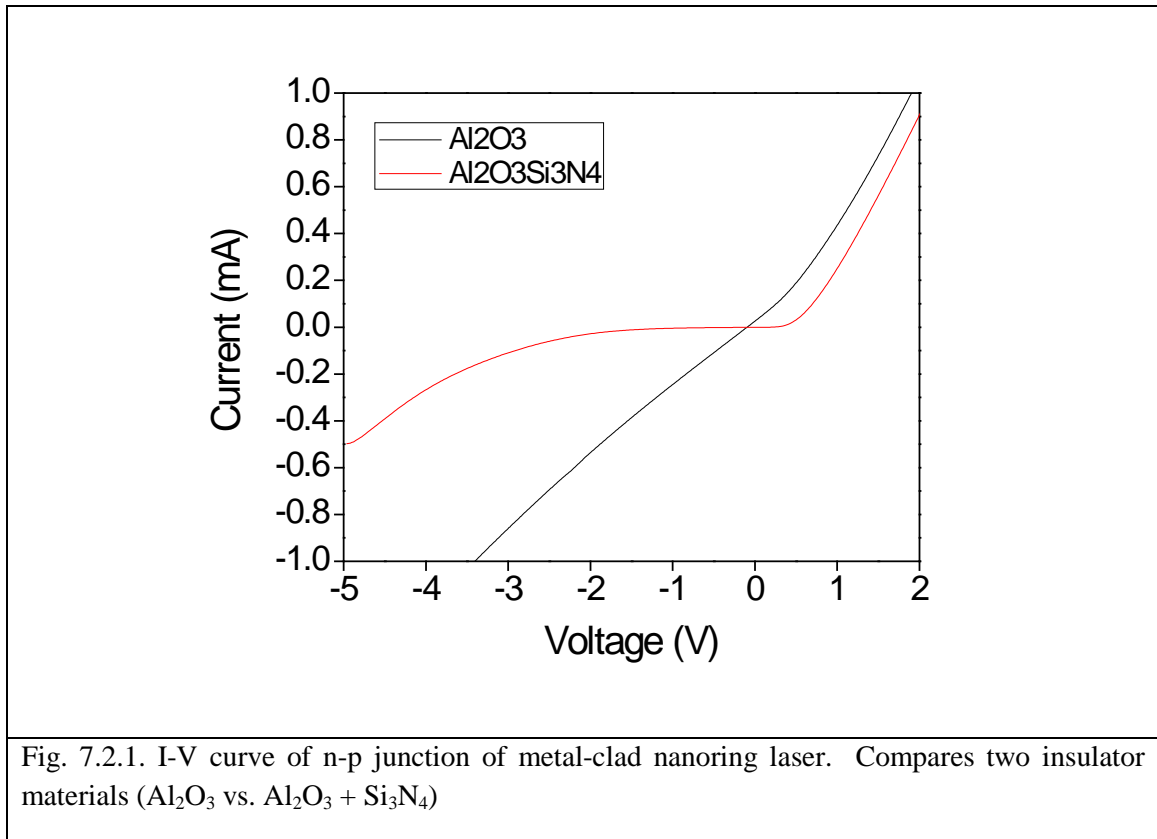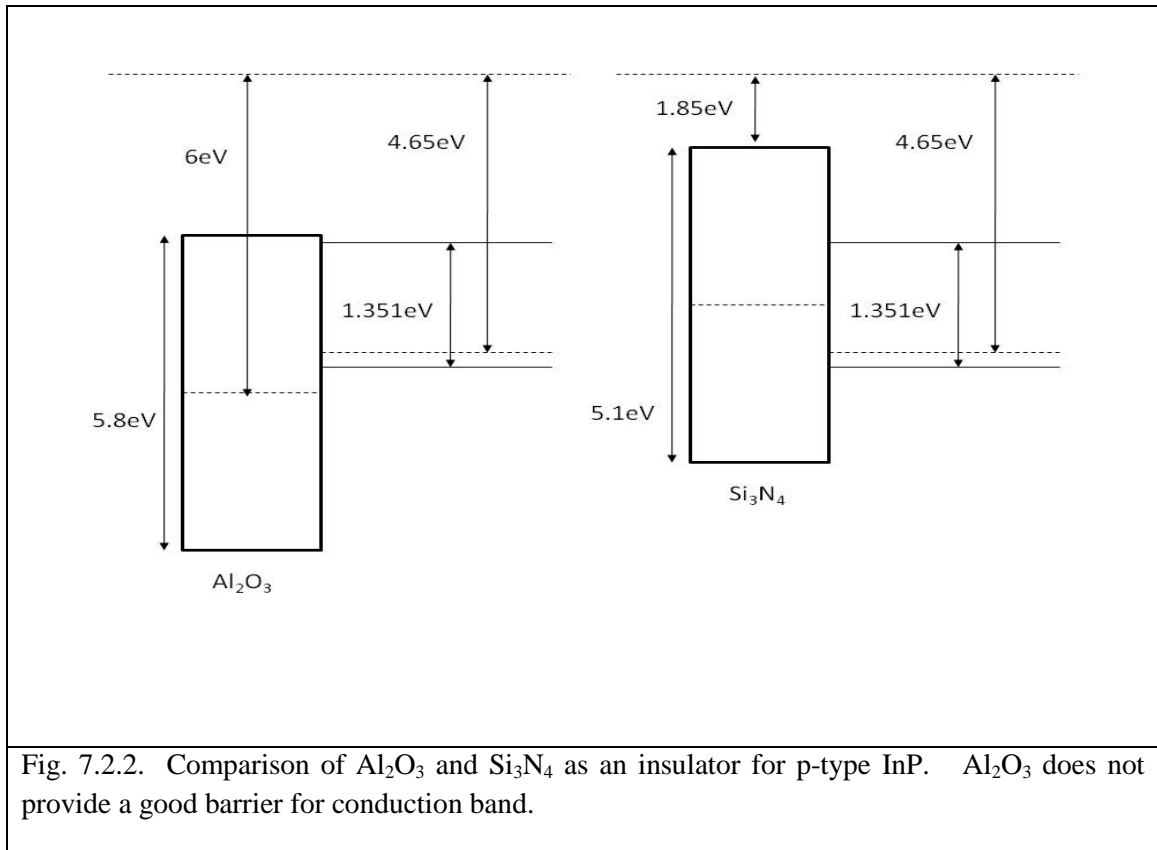
## 7.3 Summary

In this chapter, a possible scenario of electrical injection has been investigated in which n-contact is made from the top of the ring and p-contact is made from the p+ layer in the substrate.  Al$_2$O$_3$ alone was found to be not a good choice of material to serve as an insulator layer to stop the n- and p-layers from shorting, causing a leaky p-n diode. Addition of 20 nm of Si3N4 reduced the leakage and showed much improved rectification.   Currently, the resistance is around 2 k$\Omega$.  Further investigation needs to take place to reduce the resistance.

88

# CHAPTER 8

# Conclusions and Future Work

## 8.1 Conclusion

In this Thesis, methods to further decrease physical dimensions of a semiconductor laser were studied with site controllability, easy wavelength tuning, and good output coupling. Shrinking semiconductor lasers to sub-wavelength dimensions enables better on-chip integration of optoelectronic and electronic components. However, conventional air-cladding or index-contrast confinement is not efficient in confining optical modes in nanoscale dimensions. In this regard, the use of metal is beneficial, owing to the fact that electric field rapidly goes to zero inside a metal. Thus, we have investigated two different uses of metal to improve the optical confinement: surface plasmon and hybrid plasmonic/dielectric mode.

Firstly, surface plasmon was investigated for shrinking physical dimensions of a semiconductor laser. Surface plasmon is a traveling wave, formed at the interface of metal and dielectric. The electric field decays exponentially both into the metal and into the dielectric. Because of its exponential field profile, it can provide the smallest

physical laser dimensions. However, because of its peak location at the said interface, metal loss is extremely large. One proposed solution was to provide a gain medium at close proximity to the interface such that the electric field can experience optical gain, which can possibly overcome the loss. Using multi-quantum wells (MQWs) as a semiconductor gain medium and silver (Ag) as a metal layer, a waveguide experiment was conducted. It was found that the gain-assisted transmission of surface plasmon through a waveguide followed semiconductor gain function, proving that a gain medium indeed enhances surface plasmon. Additionally, we discovered that an optical gain of range from 575 cm$^{-1}$ to 1660 cm$^{-1}$ can be obtained by placing MQWs 7 nm away from the metal-semiconductor interface. Although it was not enough to compensate the loss completely, which was calculated to be 2100 cm$^{-1}$ in the GaAs-Ag system, loss compensation by a gain medium is found to be a valid method to overcome the problem of high metal loss.

Following the previous conclusion of loss compensation by a gain medium, a surface plasmon laser, named surface plasmon-enabled semiconductor injection laser (SPESIL), was explored both theoretically and experimentally. The field is confined inside SPESIL via surface plasmon in the transverse direction and via whispering gallery mode in the lateral direction. Compared to a conventional air-cladding microdisk laser, SPESIL showed superior properties for scaling, as expected. For example, the effective index of SPESIL was 3.97 as compared to 2.65 for the air-cladding microdisk laser. The higher effective index can allow us to scale down the lateral dimension without sacrificing the cavity Q. Also, despite the large metal loss, the SPESIL structure can have a larger modal gain as it has a much larger Γ —around 40% versus a typical Γ of ~

10% for a conventional microdisk laser. Due to the above reasons, SPESIL can be scaled down to sub-wavelength dimensions in all three directions. Using a rate-equation based laser model, we showed that a sub-wavelength dimension SPESIL exhibits a threshold current of 25 µA at room temperature with five quantum wells in the active region.

We, then, fabricated a SPESIL device and characterized it using a micro-photoluminescence (µ-PL) measurement scheme. From this, we were able to demonstrate gain-assisted cavity-Q enhancement. A cavity-Q factor of 66 was observed in a $0.9\lambda$-diameter cavity, which was larger than the passive cavity-Q factor calculated using 3D-FDTD calculations for the same cavity under no optical excitation. However, upon further increasing the pump power, the resonant cavities were overheated and damaged. Therefore, even though MQW gain medium was able to provide some metal loss compensation, the loss was too great to overcome even with whispering gallery mode round trip gains.

With surface plasmon metal loss in the SPESIL structure being much too high to overcome even with a gain medium placed in close proximity to the metal-semiconductor interface, we next explored the possibility of using metal resulting in a hybrid dielectric-plasmonic mode. In such modes, the peak of electric field is moved away from the interface and, therefore, metal loss is much reduced. Metal-clad semiconductor nanoring lasers were studied in detail both theoretically and experimentally. Like SPESIL, it operates in a whispering gallery mode. It had been a challenge to further shrink the ring diameters due to an increased diffraction loss with decreasing ring diameter. Theoretically, we saw that the addition of metal cladding forms a hybrid dielectric-plasmonic mode which helps confine electric field inside the semiconductor more tightly.

This brings about better scaling capabilities. The cavity Q factor in a SPESIL structure shows a saturation behavior even with an increasing device size for $D/\lambda_0 > 0.5$ where $D$ is the device diameter due to large metal loss. This saturation behavior is eliminated in the metal-clad semiconductor nanoring laser. Also we showed that, by controlling the design and by optimizing the overlap between the field and the gain medium, one can increase the Q factor. For example, the metal-clad ring lasers have better scaling properties than metal-clad pillar lasers.

Furthermore, we saw that the metal-clad nanoring lasers have two design parameters which enable independent control of cavity quality factor and resonance wavelength. There is an optimal ring width associated with each ring diameter. In general, the optimal ring width increases with ring diameter. As ring diameters become larger, the cavity Q factor is less tolerant to non-optimal design of width/diameter ratio. Conversely, the existence of two design parameter also allows fine-tuning of resonance wavelength. With the ring diameter fixed constant, ring width can alter the lasing wavelength of a metal-clad nanoring laser. This is a highly desirable feature for a nanolaser because the spectral range increases with decreasing laser dimensions. Lastly, out-coupling capabilities of metal-clad nanoring lasers were investigated in comparison to metal-clad nanopillar lasers and have been found to be superior.

Then, we demonstrated the advantage of metal-cladding in an experiment that directly compared metal-clad and no-metal 4-µm-diameter ring resonators. The metal-clad ring resonator showed a transition from spontaneous to stimulated emission at a threshold pump power that corresponded to 1.2 mW absorbed by the active region. The linewidth collapsed from 8 nm to 1.77 nm at threshold. In comparison, there was no such

transition for a ring resonator without metal coverage even at much higher pump powers. This proved the effectiveness of the metal cladding in field confinement despite increased metal loss. When fitted to laser rate equations, the $\beta$ factor of the 4-$\mu$m-diameter ring resonator was found to be $5\times10^{-4}$. Such low $\beta$ factor is due to the metal absorption loss. Addition of an insulator layer between the metal and semiconductor can reduced the metal loss.

Afterwards, we demonstrated lasing in a sub-wavelength-scale metal-clad nanoring laser. Compared to fabrication of a 4-$\mu$m-diameter ring laser, several changes were made necessary to fabricate a 1.2–$\mu$m-diameter ring laser, including a hard mask, negative resist, and addition of an insulator layer. The 1.2-$\mu$m nanoring laser showed a much lowered threshold pump power. It corresponded to actual absorbed power of 50 $\mu$W as opposed to 1.2 mW for the 4-$\mu$m. When fitted to laser rate equations, the sub-wavelength nanoring laser had a spontaneous emission coupling factor, $\beta$, of 0.01. The higher $\beta$ factor contributes to the decreased threshold pump power mentioned earlier. Additionally, fine tuning capability of the metal-clad nanoring laser has been investigated. It was shown that the lasing wavelength of a 1.2 $\mu$m diameter can be tuned within a 10-nm range by changing the ring width from 240 nm and 340 nm, and was shown to follow the trend shown by 3D-FDTD simulations.

Electrical injection scheme was also investigated. Top of the ring was to be the n-contact whereas the p+ layer in the substrate was to serve as the p- contact. Using 20 nm of $Al_2O_3$ and 20 nm of $Si_3N_4$ as an insulator to separate the n- and p- contacts, the n-p junction showed a good rectification behavior with resistance of 2k$\Omega$.

## 8.2 Future work

In order to facilitate integration of optoelectronic and electronic components, two conditions are necessary: electrical injection and room temperature operation. Firstly, it is critical that an on-chip laser be capable of electrical injection with a low threshold current for power conservation. In this Thesis, lasing has been demonstrated in a metal-clad semiconductor nanoring laser under optical pumping. Further study needs to take place demonstrating the operability of a metal-clad semiconductor nanoring laser under electrical injection. To this end, several aspects need to be investigated. For one, ohmic contacts need to be studied more in detail to minimize the series resistance. Additionally, surface roughness as well as the sidewall slope needs to be improved. Rough sidewall contributes to scattering losses, and electric field becomes leaky with a non-vertical sidewall slope.

It is also important that the laser be operated at room temperature as it is impracticable to have a cooling unit on a chip. During the experiments described in this Thesis, the pump laser power heated up the sample, especially since most of the focused laser spot was outside of the resonator. An additional advantage of an electrically injected metal-clad semiconductor nanoring laser is the mitigation of the said sample heating problem. Also, previously mentioned improvement of surface roughness and sidewall slope can result in an improved cavity Q factor, which facilitates room temperature operation.

Lastly, another important aspect of an on-chip laser to be used for the integration of optoelectronic and electronic components is the light out-coupling. Therefore, coupling of emitted light and a waveguide must be studied.

# BIBLIOGRAPHY

1 S. L. Chuang, <u>Physics of Photonic Devices</u>, John Wiley and Sons, Hoboken, NJ, 2009.

2. K.A.S. Imminkm "The digital versatile disc (DVD): System requirements and channel coding," *SMPTE*, 105 8 (1996) 483 -489

3. R. Allan, "Low-power laser drivers feature multiple channels for DVD, CD and other applications ," Electronic Design, 48 19 (2000)

4. R. Katayama and Y. Komatsu, "Blue/DVD/CD compatible optical head," Applied Optics, 47 22 (2008) 4045-4054

5. L. Longo, "Non surgical laser and light in the treatment of chronic diseases: a review based on personal experiences," *Laser Physics Letters*, 7 11 (2010) 771-786

6. R.H. Kim, et al., "Waterproof AlInGaP optoelectronics on stretchable substrates with applications in biomedicine and robotics," *Nature Materials*, 9 11 (2010) 929-937

7. M. Misiuk-Hojlo, P. Krzyzanowska-Berkowska, and A. Hill-Bator, "Therapeutic applications of lasers in ophthalmology," *Advances in Clinical and Experimental Medicine,* 16 6 (2006) 801-805

8. J. Zelingher, "Exploring the internet," *MD Computing*, 12 2 (1995)

9. P. Boffi, M.C. Ubaldi, D. Piccinin, M. Martinelli, "1550 nm volume holographic devices for optical communication networks," *Infrared Holography for Optical Communications*, 86 (2002) 157-178

10. A.V. Krishnamoorthy, D.A.B Miller, "Scaling optoelectronic-VLSI circuits into the 21st century: A technology roadmap," *IEEE Journal of Selected Topics in Quantum Electronics,* 2 1 (1996) 55-76

11. I. Hayashi, "Optoelectronic devices and material technologies for photo-electronic integrated systems, *Japanese Journal Of Applied Physics Part 1-Regular Papers Short Notes & Review Papers*, 32 1B (1993) 266-271

12. P. Lukowicz, J. Jahns, R. Barbieri, P. Benabes, T. Bierhoff, A. Gauthier, M. Jarczynski, G.A. Russell , J. Schrage, W. Sullau, J.F. Snowdon, M. Wirz, G. Troster, "Optoelectronic interconnection technology in the HOLMS system," *IEEE Journal of Selected Topics in Quantum Electronics*, 9 2 (2003) 624-635

13. G. Roelkens, L. Liu, D. Liang, R. Jones, A. Fang, B. Koch, J. Bowers, "III-V/Silicon photonics for on-chip and inter-chip optical interconnect," *Laser and Photonics Review*, 4 6 (2010) 751-779

14. D.A.B. Miller, "Physical reasons for optical interconnection," *International Journal of Optoelectronics*, 11 3 (1997) 155-168

15. M.R. Reshotko, D.L. Kencke, B. Block, "High-speed CMOS compatible photodetectors for optical interconnects," *Infrared Detector Materials and Devices*, 5564 (2004) 146-155

16. Intel, "Moore's law", http://www.intel.com/technology/mooreslaw/

17. T. Baba, "Photonic crystal and microdisk cavities based on GaInAsP-InP systems," *IEEE Journal of Selected Topics in Quantum Electronics*, 3 3 (1997) 808-830

18. W.J. Wadsworth, R.M. Percival , G. Bouwmans, J.C. Knight, P.S.J. Russel, "High power air-clad photonic crystal fibre laser," *Optics Express* 11 1 (2003) 48-53

19. D. Liang, J.S. Wang, D.C. Hall, G.M. Peake, and Q. Hartmann, "High-index-constrat ridge waveguide lasers fabricated via oxygen-enhanced wet thermal oxidation," *Novel In-Plane Semiconductor Lasers V, Proceedings Of The Society Of Photo-Optical Instrumentation Engineers (SPIE)*, 6133 (2006) 13312

20. Y. Tanaka, T. Asano, R. Hatsuta, S. Noda, "Investigation of poin-defect cavity formed in two-dimensional photonic crystal slab with one-dimensional dielectric cladding," *Applied Physics Letters*, 88 1 (2006)

21. S. L. McCall, A.F.J Levi, R.E. Slusher, S.J. Pearton, and R.A. Logan, "Whispering-gallery mode microdisk laser," *Applied Phyics Letters*, 60 (1992) 289-292

22. J. Van Campenhout, P. Rojo Romeo, P. Regreny, C. Seassal, D. VAN Thourhout, S. Verstuyft, L. Di Cioccio, J.-M. Fedeli, C. Lagahe and R. Baets, "Electrically pumped InP-based microdisk lasers integrated with a nanophotonic silicon-on-insulator waveguide circuit," *Optics Express*, 15 11 (2007) 6744-6749

23. Z. Zhang, L. Yang, V. Liu, T. Hong, K. Vahala, and A. Scherer, "Visible submicron microdisk lasers," *Applied Physics Letters*, 90 111119 (2007)

24. T. Baba, "Photonic crystals and microdisk cavities based on GaInAsP-InP system," *IEEE Journal of Selected Topics in Quantum Electronics*, 3 (1997) 808-830

25. J. Topolancik, S. Chakravarty, P. Bhattacharya, and S. Chakrabarti, "Electrically injected quantum-dot photonic crystal microcavity light sources," *Optics Letters*, 31 2 (2006) 232-234

26. M. H. Huang, S. Mao, H. Feick, H. Yan, Y. Wu, H. Kind, E. Weber, R. Russo, P. Yang, "Room-temperature ultraviolet nanowire nanolasers," *Science,* 292 (2001), 1879-1899

27. J. C. Johnson, H.J. Choi, K.P Knutsen, R.D. Schaller, P.D. Yang, R.. Saykally, "Single gallium nitride nanowire lasers," *Nature Materials* 1 2 (2002) 106-110

28. P.J. Pauzauskie, D.J. Sirbuly, and P. Yang, "Semiconductor nanowire ring resonator laser," *Physical Review Letters*, 96 143903 (2006)

29. P. Yeh, *Optical waves in layered media*. New York: Wiley, 1988

30. D. K. Armani, T. J. Kippenberg, S. M. Spillane, and K. J. Vahala, "Ultra-high-Q toroid microcavity on a chip," *Nature,* vol. 421, pp. 925-928, 2003.

31. N. Yu, E. Cubukcu, L. Diehl, D. Bour, S. Corzine, J. Zhu, G. Hofler, K. Crozier, and F. Capasso, "Bowtie plasmonic quantum cascade laser antenna," *Optics Express*, 15 13272 (2007)

32. S.-W. Chang and S.-L. Chuang, "Plasmonic nanolaser based on metallic bowtie cavity," *Conference on Lasers and Electro-Optics (CLEO)*, QTuJ5, 2008

33. M. T. Hill, Y.-S. Oei, B. Smalbrugge, Y. Zhu, T. De Vries, P. J. Van Veldhoven, F. W. M. Van Otten, T. J. Eijkemans, J. P. Turkiewicz, H. De Waardt, E. Jan Geluk, S.-H. Kwon, Y.-H. Lee, R. Notzel, and M. K. Smit, "Lasing in metallic-coated nanocavities," *Nature Photonics*, **1**, 589-594 (2007)

34. M. T. Hill, M. Marell, E. S. P. Leong, B. Smalbrugge, Y. Zhu, M. Sun, P. J. Van Veldhoven, E. Jan Geluk, F. Karouta, Y.-S. Oei, R. Notzel, C.-Z. Ning, and M. K. Smit, "Lasing in metal-insulator-metal sub-wavelength plasmonics waveguides," Optics Express, **17** 13, 11107-11112 (2009)

35. R. F. Oulton, V. J. Sorger, T. Zentgraf, R.-M. Ma, C. Gladden, L. Dai, G. Bartal and X. Zhang, "Plasmon lasers at deep subwavelength scale," *Nature*, **461**, 629-632 (2009)

36. K. Yu, A. Lakhani, M. C. Wu*, "*Subwavelength metal-optic semiconductor nanopatch lasers," *Optics Express* **18** 9 (2010) 8790-8799

37. M. A. Noginov, G. Zhu, A. M. Belgrave, R. Bakker, V. M. Shalaev, E. E. Narimanov, S. Stout, E. Herz, T. Suteewong and U. Wiesner, "Demonstration of a spaser-based nanolaser," *Nature*, **460**, 1110-1113 (2009)

38. H. Raether, *Surface Plasmons on Smooth and Rough Surfaces and on Gratings*. Berlin: Springer-Verlag, 1988

39. S. I. Bozhevolnyi, V. S. Volkov, and K. Leosson, "Localization andWaveguiding of Surface Plasmon Polaritons in Random Nanostructures," *Phys. Rev. Lett* **89,** 186801 (2002)

40. A. Boltasseva, S. I. Bozhevolnyi, , T. Søndergaard, T. Nikolajsen, and L. Kristjan, "Compact Z-add-drop wavelength filters for long-range surface plasmon polaritons," *Optics Express* **13**, 4237-4243 (2005)

41. S. A., Maier, P. G. Kik, H. A. Atwater, S. Meltzer, E. Harel, B. E. Koel, and A. A. G. Requicha, "Local detection of electromagnetic energy transport below the diffraction limit in metal nanoparticle plasmon waveguides," *Nature Materials* **2**, 229-232 (2003)

42. A. Karalis, E. Lidorikis, M. Ibanescu, J. D. Joannopoulos, and S. Marin, "Surface-Plasmon-Assisted Guiding of Broadband Slow and Subwavelength Light in Air," *Phys. Rev. Lett.* **95**, 063901 (2005)

43. M. Stockman, "Nanofocusing of Optical Energy in Tapered Plasmonic Waveguides," *Phys. Rev. Lett*. **93**, 137404 (2004)

44. V. M. Shalaev, "Optical negative-index metamaterials," *Nat. Photon.* **1**, 41–48 (2007)

45. S. Lal, S. Link, N. J. Halas, "Nano-optics from sensing to waveguiding," *Nat. Photonics* **1**, 641–648 (2007)

46. J. N. Anker, W. P. Hall, O. Lyandres, N. C. Shah, J. Zhao, R. P. Van Duyne, "Biosensing with plasmonic nanosensors," *Nat. Mater.* **7**, 442–453 (2008)

47. A. N. Sudarkin and P. A. Demkovich, "Excitation of surface electromagnetic waves on the boundary of a metal with an amplifying medium," *Sov. Phys. Tech. Phys.* **34,** 764-766 (1989)

48. M. A. Noginov, V. A. Podolskiy, G. Zhu, M. Mayy, M. Bahoura, J. A. Adegoke, B. A. Ritzo, and K. Reynolds, "Compensation of loss in propagating surface plasmon polariton by gain in adjacent dielectric medium," *Optics Express*, 16 2 1385-1392 (2008)

49. J. Singh, *Electronic and Optoelectronic Properties of Semiconductor Structures*, Cambridge University Press, 2003

50. M. Ambati, S. H. Nam, E. Ulin-Avila, D. A. Genov, G. Bartal and X. Zhang, "Observation of stimulated emission of surface plasmon polaritons," *Nanoletters* 8 11, 3998-4001 (2008)

51. G. I. Stegeman, R. F. Wallis, and A. A. Maradudin, "Excitation of surface-polaritons by end-fire coupling," *Opt. Lett.,* vol. 8, pp. 386-388, 1983.

52. S. L. Chuang, *Physics of optoelectronic devices*. New York: Wiley, 1995

53. P. B. Johnson and R. W. Christy, "Optical Constants of Noble Metals," *Phys. Rev. B,* vol. 6, pp. 4370-4379, 1972.

54. M. P. Nezhad, K. Tetz, and Y. Fainman, "Gain assisted propagation of surface plasmon polaritons on planar metallic waveguides," *Optics Express*, 12 17 (2004) 4072-4079

55. J. Seidel, S. Grafstrom, and L. Eng, "Stimulated emission of surface plasmons at the interface between a silver film and an optically pumped dye solution," *Physical Review Letters*, 94 177401 (2005)

56. G. Zhu, M. Mayy, M. Bahoura, J.A. Adegoke, V.A. Podolskiy and M.A. Noginov, "Compensation of loss in propagating surface plasmon by optical gain," *Quantum Electronics and Laser Science (QELS) Conference*, JMA5, 2007

57. L.A. Coldren, *Diode Lasers and Photonic Integrated Circuits*, Wiley-Interscience, 1995

58. S.L. Chuang, *Physics of Optoelectronic Devices*, Ch. 9, Wiley-Pure and Applied Optics, 1995

59. D. R. Scifres, R. D. Burnham, and W. Streifer, "Grating-coupled GaAs single heterostructure ring laser," *Appl. Phys. Lett.,* **28** (1976) 681.

60. N. Matsumoto and K. Kumabe, "AlGaAs-GaAs Semiconductor Ring Laser," *Jpn. J. Appl. Phys.,* **16** (1977) 1395

61. Sorel, G. Giuliani, A. Scire, R. Miglieria, S. Donati and P.J.R Laybourn, "Operating regimes of GaAs-AlGaAs semiconductor ring lasers: Experiment and model," *IEEE J. Quantum Electron.* **39**, 1187 (2003)

62. L. Gelens, S. Beri, G. Van der Sande, G. Mezosi, M. Sorel, J. Danckaert, and G. Verschaffelt, "Exploring Multistability in Semiconductor Ring Lasers: Theory and Experiment," *Physical Review Letters* **102**, 193904 (2009)

63. W. Coomans, S. Beri, G. Van der Sande, L. Gelens, and J. Danckaert, "Optical injection in semiconductor ring lasers, " *Phys. Rev. A* **81**, 033802 (2010)

64. A. F. Oskooi, D. Roundy, M. Ibanescu, P. Bermel, J. D. Joannopoulos, and S. G. Johnson, "MEEP: A flexible free-software package for electromagnetic simulations by the FDTD method," *Computer Physics Communications* **181**, 687–702 (2010)

65. V. A. Mandelshtam and H. S. Taylor, "Harmonic inversion of time signals," *J. Chem. Phys.* **107** (17), 6756-6769 (1997). Erratum, *ibid.* **109** (10), 4128 (1998)

66. M. M. Raj, J. Wiedmann, S. Toyoshima, Y. Saka, K. Ebihara, and S. Arai, "High reflectivity semiconductor/benzocyclobutene bragg reflector mirrors for GaInAsP/InP lasers," *Jpn. J. Appl. Phys.,* vol. 40, 2269-2277 (2001)

67. P.B. Johnson and R.W. Christy, *Physical Review B*, **6** 12, 4370-4379 (1972)

68. A. S.-H. Liao and S. Wang, "Semiconductor injection lasers with a circular resonator," *Appl. Phys. Lett.* **36** 10, 801-803 (1980)

69. A. W. Poon, X. S. Luo, F. Xu, and H. Chen, "Cascaded Microresonator-Based Matrix Switch for Silicon On-Chip Optical Interconnection," *Proc. IEEE* **97** 7, 1216–1238 (2009).

70. F. Xia, L. Sekaric, and Y. Vlasov, "Ultracompact optical buffers on a silicon chip," *Nature Photonics* **1**, 65–71(2007).

71. J. Van Campenhout, P. Rojo-Romeo, P. Regreny, C. Seassal, D. Van Thourhout, S. Verstuyft, L. Di Cioccio, J.-M. Fedeli, C. Lagahe and R. Baets, "Electrically pumped InP-based microdisk lasers integrated with a nanophotonic silicon-on-insulator waveguide circuit," *Optics Express* **15** 11, 6744-6749 (2007)

72. A. Yariv, *Optical Electronics*. Saunders College Publishing, 1991 p. 180

73. P.B. Johnson and R.W. Christy, *Physical Review B*, **6** 12, 4370-4379 (1972)

74. R. G. Beausoleil, P. J. Kuekes, G. S. Snider, S. Y. Wang, and R. S. Williams, *Proceedings of the IEEE,* **96** (2008) 230.

75. D. A. B. Miller, *Proceedings of the IEEE,* **88** (2000) 728.

76. B.E. Little, S.T. Chu, H.A. Haus, J.S. Foresi and J.-P. Laine, *Journal of Lightwave Technology* **15**, 998-1005 (1997).

77. G. Lenz and C. K. Madsen, *Journal of Lightwave Technology,* **17** (1999) 1248.

78. F. N. Xia, L. Sekaric, and Y. Vlasov, *Nature Photonics,* **1** (2007) 65.

79. D. R. Scifres, R. D. Burnham, and W. Streifer, *Appl. Phys. Lett.,* **28** (1976) 681.

80. N. Matsumoto and K. Kumabe, *Jpn. J. Appl. Phys.,* **16** (1977) 1395